

#### UNIVERSIDAD DE VALENCIA PROGRAMA DE DOCTORADO EN INGENIERÍA ELECTRÓNICA

Study and improvement of firmware for advanced trigger algorithms, real-time data compression, and pile-up in NEDA (Neutron Detector Array)

Presented by:

Jose Manuel Deltoro Berrio

Director:

Vicente González Millán



El Dr. D. Vicente González Millán, Catedrático de Universidad del Departamento de Ingeniería Electrónica de la Universidad de Valencia.

HACE CONSTAR: Que el Ingeniero Electrónico D. Jose Manuel Deltoro ha realizado bajo su dirección el trabajo titulado "Study and improvement of firmware for advanced trigger algorithms, real-time data compression, and pile-up in NEDA (Neutron Detector Array).", que se presenta en esta memoria para optar al grado de Doctor en Ingeniería Electrónica.

Y para que así conste, firmo el presente documento en Valencia a FECHA.

Fdo. D. Vicente González Millán.

UNIVERSIDAD DE VALENCIA ESCUELA TÉCNICA SUPERIOR DE INGENIERÍA Departamento de Ingeniería Electrónica Avd. de la Universitat s/n, 46100 Buriassot (Valencia)



Acta de calificación de tesis doctoral

# Acknowledgments

## Abstract

Nuclear physics is a branch of physics that studies atomic nuclei, exploring their structure, properties, interactions, and the forces that bind them together. This discipline is fundamental to understanding the universe at the microscopic and macroscopic levels.

The importance of nuclear physics is enormous and extends to various areas of science and technology. For instance, in medicine, imaging techniques such as Positron Emission Tomography (PET) and radiation therapy for cancer treatment are based on nuclear physics principles. In astrophysics, nuclear physics helps explain processes occurring in stars, including how elements are formed in nuclear reactions. Nuclear energy is also essential for energy production. Nuclear power plants, which provide a significant energy source worldwide, operate using controlled nuclear reactions.

In nuclear physics research, the nuclear structure is studied using highresolution gamma-ray spectroscopy. This method accurately recovers the energy and angular distributions of gamma photons emitted in the transition between nuclear states.

The electronics associated with the radiation detectors used in experiments are crucial for high-resolution gamma-ray spectroscopy. These instruments must be capable of detecting and measuring subatomic particles and radiation with high precision, which requires advanced electronics.

The current trend is towards the use of digital electronics, which offer greater flexibility and the ability to implement more complex data analysis algorithms. However, for certain high-resolution measurements, analogue electronics outperform digital electronics. Therefore, one of the challenges in this field is achieving the same performance level with digital systems.

One of the latest-generation instruments that uses the gamma-ray spectroscopy technique is the AGATA (Advanced GAmma Tracking Array) detector array. This instrument can have ancillary detectors to assist in gamma-ray spectroscopy. One of the ancillary detectors developed is the Neutron Detector Array (NEDA), a neutron detection system designed to be versatile, with high detection efficiency, excellent neutron discrimination, and high-rate capabilities.

This thesis focuses on improving the data acquisition and analysis capabilities of NEDA through the following enhancements.

First, developing a lossless data compression method that allows the signals acquired by NEDA to be compressed individually. Applying this technique allows for increasing the counting rate in the experiments and reducing the storage size required for each event and, therefore, the total data acquired.

Secondly, a double trigger condition system is developed to improve neutron-gamma discrimination. This involves an in-depth study of the electronics and firmware already implemented in the digitiser of NEDA called NUMEXO2. The system enhances the acquisition capabilities by combining two independent trigger signals based on Charge Comparison (CC) and Time-Of-Flight (TOF) measurements. Implementing this system in the Virtex-6 FPGA includes signal processing, baseline correction, and various trigger logic blocks. Evaluations using data from the E703 experiment at GANIL show that the AND trigger mode is effective for experiments requiring a low level of trigger requests. In contrast, the OR mode is beneficial for minimising neutron loss when the system can handle higher trigger requests.

Thirdly, the thesis addresses the issue of pulse pile-up in nuclear spectroscopy and reaction studies, where overlapping pulses degrade energy and timing information. The proposed solution uses a one-dimensional convolutional autoencoder (1D-CAE) to reconstruct pile-up events. The method reconstructs pile-up signals and evaluates them by comparing the reconstructed signals to the original ones, achieving very high levels of similarity. This solution allows for the correct analysis of reconstructed signals using Pulse Shape Analysis techniques and provides correct neutron/gamma discrimination.

## Resumen

## Introducción

La física nuclear es una rama de la física que estudia los núcleos atómicos, explorando su estructura, propiedades, interacciones y las fuerzas que los unen. Esta disciplina es fundamental para comprender el universo a nivel microscópico y macroscópico.

La importancia de la física nuclear es enorme y se extiende a diversas áreas de la ciencia y la tecnología. Por ejemplo, en medicina, las técnicas de imagen como la Tomografía por Emisión de Positrones (PET) y la radioterapia para el tratamiento del cáncer se basan en principios de la física nuclear. En astrofísica, la física nuclear ayuda a explicar los procesos que ocurren en las estrellas, incluido el modo en que se forman los elementos en las reacciones nucleares. La energía nuclear también es esencial para la producción de energía. Las centrales nucleares, que proporcionan una importante fuente de energía en todo el mundo, funcionan mediante reacciones nucleares controladas.

En la investigación de la física nuclear, la estructura nuclear se estudia mediante espectroscopia de rayos gamma de alta resolución. Este método recupera con precisión la energía y las distribuciones angulares de los fotones gamma emitidos en la transición entre estados nucleares. La electrónica asociada a los detectores de radiación utilizados en los experimentos es crucial para la espectroscopia de rayos gamma de alta resolución. Estos instrumentos deben ser capaces de detectar y medir partículas subatómicas y radiación con alta precisión, lo que requiere una electrónica avanzada.

La tendencia actual es hacia el uso de la electrónica digital, que ofrece una mayor flexibilidad y la capacidad de implementar algoritmos de análisis de datos más complejos. Sin embargo, para ciertas medidas de alta resolución, la electrónica analógica supera a la electrónica digital. Por tanto, uno de los retos en este campo es conseguir el mismo nivel de rendimiento con los sistemas digitales.

Uno de los instrumentos de última generación que utiliza la técnica de espectroscopia de rayos gamma es el array de detectores AGATA (Advanced GAmma Tracking Array). Este instrumento puede disponer de detectores auxiliares para ayudar en la espectroscopia de rayos gamma. Uno de los detectores

auxiliares desarrollados es el Neutron Detector Array (NEDA), un sistema de detección de neutrones diseñado para ser versátil, con una alta eficiencia de detección, una excelente discriminación de neutrones y capacidades de alta velocidad.

NEDA es un conjunto avanzado de detectores de neutrones desarrollado a través de una colaboración internacional que involucra a varios institutos de nueve países europeos. Este innovador sistema fue concebido como el sucesor del detector Neutron Wall. NEDA consiste en un conjunto de detectores de neutrones de nueva generación basados en un centellador líquido. NEDA ha sido diseñado para acoplarse a un conjunto de detectores de rayos gamma basados en germanio como AGATA, EXOGAM2 o GALILEO.

La primera implementación de NEDA se llevó a cabo junto con el Neutron Wall y AGATA en GANIL. No obstante, la movilidad de NEDA permite integrarse fácilmente con otros conjuntos de detectores de rayos gamma. Los detectores de neutrones y de partículas cargadas juegan un papel crucial en la elección efectiva de procesos de decaimiento, especialmente al investigar núcleos deficientes en neutrones resultantes de reacciones de fusión-evaporación. Además, NEDA sirve como un instrumento indispensable para la exploración de núcleos exóticos generados a través de reacciones de transferencia donde la partícula emitida es un neutrón. En los próximos años, la disponibilidad de una amplia gama de nuevos haces radiactivos para reacciones de transferencia inducidas por proyectiles ricos en protones y neutrones se expandirá significativamente. Esta expansión será facilitada por instalaciones de haces radiactivos de vanguardia como HIE-ISOLDE (CERN, Ginebra, Suiza), SPES (Legnaro, Italia), SPIRAL2 (Caen, Francia) y FAIR (Darmstadt, Alemania).

Respecto a la electrónica de NEDA, su principal componente es NUMEXO2, el cual también era utilizado previamente para el detector EXOGAM. NU-MEXO2 es responsable de digitalizar y preprocesar datos para ambos detectores. A pesar de los diferentes objetivos de estos detectores y metodologías en términos de detección de radiación, las funcionalidades de NUMEXO2 útiles para ambos detectores. Estas incluyen la conversión Analógica a Digital (A/D), el preprocesamiento de datos, la interfaz con el sistema GTS y la gestión de enlaces de comunicación para 16 canales. El digitalizador NU-MEXO2 consta de una placa base y un conjunto de cuatro FADC Mezzanines. La placa base fue desarrollada por el Group d'Acquisition pour la Physique (GAP) en el Grand Accélérateur National d'Ions Lourds (GANIL) en Caen. Los FADC Mezzanines desarrollados en la Universidad de Valencia realizan la conversión A/D para cuatro canales.

Una de las características clave de NUMEXO2 es su flexibilidad, que se atribuye a su uso de electrónica digital con dispositivos lógicos programables. Esta característica permite una base de hardware común, pero con dispositivos programables de alto rendimiento que pueden implementar varios algo-

ritmos de procesamiento de señales digitales. Específicamente, NUMEXO2 incluye dos, en ese momento, FPGA (Field-Programmable Gate Arrays) de alto rendimiento, una Virtex-6 y una Virtex-5 de Xilinx.

Esta tesis se centra en proporcionar mejoras significativas en los sistemas de adquisición y análisis de datos para NEDA mediante nuevas funcionalidades, contribuyendo así a la eficiencia y precisión de los experimentos en física nuclear. En este resumen se van a explicar los objetivos de la tesis, la metodología empleada, el desarrollo e implementación de las nuevas funcionalidades y las conclusiones obtenidas.

## **Objetivos**

A continuación se resumen los principales objetivos de la tesis, considerando el entorno en el que se desarrolla.

- Estudio del entorno: Realizar un estudio esencial del marco científico en el que está involucrado NEDA, así como de la estructura, electrónica y diseños implementados previamente.
- Compresión de datos sin pérdida en línea: Se realizará un estudio de los diferentes métodos de compresión existentes y se desarrollará de un método de compresión sin pérdida que reduzca el tamaño de almacenamiento y ofrezca la posibilidad de aumentar la tasa de conteo en experimentos NEDA.
- Sistema de condición de doble disparo: Desarrollar un sistema de condición de disparo que mejore las capacidades de adquisición de discriminación neutrón-gamma previamente implementadas y estudiar su efecto en el análisis de datos. Para llevar a cabo esta mejora, se estudiará en detalle la electrónica involucrada en NEDA, principalmente el firmware ya implementado en NUMEXO2.
- Reconstrucción de pulsos apilados: El apilamiento de pulsos es un problema en espectroscopia nuclear y estudios de reacciones nucleares que ocurre cuando dos pulsos se superponen y se distorsionan entre sí, degradando la calidad de la información de energía y tiempo. Por lo tanto, el último objetivo de esta tesis es estudiar los diferentes métodos de separación y reconstrucción de pulsos, y ofrecer un nuevo método de reconstrucción de pulsos basado en técnicas de aprendizaje automático.

## Metodología

La metodología utilizada en esta tesis está diferenciada para cada uno de los objetivos a alcanzar. El procedimiento aplicado a cada objetivo se detalla a continuación.

- Estudio de antecedentes: La tarea inicial, que sirve no solo para familiarizarse con las especificaciones de diseño en NEDA, sino también para adquirir conocimientos básicos fundamentales relevantes para los objetivos del experimento, implica explorar el entorno experimental y su física fundamental. En consecuencia, esto incluye una descripción general de la espectroscopia nuclear de rayos gamma y las interacciones neutrónicas de la radiación con la materia. Además, parte del trasfondo es el estudio detallado de la estructura del detector NEDA y su electrónica frontal.
- Compresión de datos sin pérdida online: La compresión de datos es un campo de investigación que se ha estudiado desde la década de 1940. Hasta la fecha se han desarrollado numerosos métodos de compresión, por lo que el primer paso es estudiar los más relevantes e investigar qué método desarrollar para su implementación en la electrónica NEDA. Entre los diferentes métodos desarrollados hasta ahora, el estudio se centrará en los métodos de compresión sin pérdida, ya que no es deseable perder información de eventos. Una vez seleccionado el método de compresión, se desarrolla en Python utilizando datos de experimentos reales para probar su validez. Posteriormente, el método se implementará en el digitalizador NUMEXO2. Finalmente, se realizan pruebas para verificar la efectividad del método de compresión de datos sin pérdida online.
- Sistema de condición de doble disparo: Para desarrollar el sistema de condición de doble disparo, el primer paso es estudiar el firmware implementado en NUMEXO2. A continuación, se elige cuál de las dos FPGA (Virtex-5 y Virtex-6) de NUMEXO2 debe albergar el nuevo sistema de disparo. Tras esto, se debe implementar el sistema y probarlo en el laboratorio para verificar su correcto funcionamiento. Finalmente, se debe utilizar este sistema en experimentos con haz, y se debe realizar un estudio del impacto del nuevo sistema de disparo en los datos analizados.
- Reconstrucción de pulsos apilados: Las señales con pulsos apilados normalmente se descartan, ya que la información de los pulsos está distorsionada. En este caso, la reconstrucción de pulsos se realizará mediante técnicas de aprendizaje automático utilizando señales del detector NEDA. En primer lugar, se estudian diferentes formas y métodos para separar y reconstruir los pulsos apilados. Posteriormente, se ha de estudiar el estado del arte de la Inteligencia Artificial, el Aprendizaje Automático y las Redes Neuronales para resolver problemas similares al apilamiento de pulsos. Después, se ha de implementar un método de separación y reconstrucción de pulsos basado en técnicas de aprendizaje automático. Finalmente, se ha de evaluar el rendimiento y precisión del nuevo método.

## Desarrollo e implementación

Aunque las nuevas funcionalidades desarrolladas en esta tesis se enmarcan en el detector de NEDA, éstas no están directamente conectadas por lo que el desarrollo e implementación de cada una de ellas se ha llevado a cabo de forma independiente.

### Compresión de datos sin pérdida online

En esta tesis se ha desarrollado un método de compresión sin pérdida para reducir el tamaño de almacenamiento necesario y aumentar la tasa de conteo en los experimentos. Se ha decidido utilizar un método de compresión sin pérdida para evitar la pérdida de información del evento. La implementación se ha realizado en Python utilizando datos de experimentos de NEDA y posteriormente se ha implementado en el digitalizador NUMEXO2.

En los últimos años, la capacidad de almacenamiento de datos y la velocidad de procesamiento en la electrónica y las redes de comunicación han aumentado. No obstante, lograr velocidades más altas es complicado, especialmente cuando el hardware no se puede modificar, como es el caso de la electrónica de NEDA. En este entorno, una técnica crucial para mejorar el rendimiento es la compresión de datos, ya que el proceso de compresión-transmisión es más rápido que la transmisión sin compresión. La compresión de datos también es beneficiosa para el almacenamiento masivo, reduciendo los costos tanto en almacenamiento como en transmisión de datos.

Existen varios métodos y algoritmos para reducir o eliminar datos redundantes y lograr la compresión de datos, que se clasifican en dos grupos: con pérdida y sin pérdida. En la transmisión de datos, se prefieren los métodos de compresión sin pérdida para garantizar que los datos transmitidos sean idénticos a los originales, lo cual es crucial para aplicaciones donde la precisión es vital, como en imágenes médicas, datos científicos y transacciones financieras. En los experimentos de NEDA, es esencial mantener la información del evento para analizar adecuadamente la forma de onda.

Se han estudiado diferentes métodos de compresión sin pérdida para elegir el más adecuado e implementarlo en el firmware existente de NUMEXO2. Se han considerado varios aspectos de diseño, como las capacidades de lectura de NUMEXO2 en experimentos de NEDA, donde la tasa de conteo se ha establecido en 50 kHz y NUMEXO2 trabaja con 16 canales. Cada evento tiene un tamaño de 256 muestras, y cada muestra es de 2 bytes, resultando en un tamaño total de 512 bytes por evento. Si se reduce el número de bits necesarios para formar la traza de cada evento, se podría aumentar la tasa de conteo sin exceder la tasa máxima de 409.6 MB/s.

El método de compresión se ha implementado en la FPGA Virtex-6, ya que está primero en la cadena de adquisición, lo que permita también una transmisión más rápida de eventos entre Virtex-6 y Virtex-5. Para el diseño del método de compresión se ha tenido en cuenta que se han de utilizar el mínimo de recursos posibles, permitiendo la implementación del diseño actual y posibles modificaciones futuras. La compresión se ha centrado en reducir el tamaño en bytes de la traza de cada evento, manteniendo el tamaño del encabezado del evento. También se ha considerado la relación de compresión y el ahorro de espacio al elegir el método de compresión adecuado.

Se han estudiado diversos métodos de compresión sin pérdida, analizando y aplicando ad-hoc algunos de los métodos más simples y comúnmente utilizados en ingeniería, ciencias de la computación y física, para evaluar su idoneidad en la compresión de las trazas de eventos de NEDA, buscando el mejor compromiso entre capacidad de compresión y bajo consumo de recursos.

El método de compresión elegido ha sido el de Codificación diferencial con número de bits fijo. Se trata de un método ad-hoc para NEDA que se basa en calcular la diferencia entre muestras y almacenar la diferencia en un número fijo de bits. Se ha realizado un estudio de las señales para evaluar si es posible asignar un número fijo de bits para almacenar las muestras en diferencias. De esta forma se ha establecido que en la línea de base se puede almacenar cada muestra utilizando la mitad de bits. Por otro lado, este método deja sin comprimir la parte de la señal correspondiente al pulso.

Se ha verificado el funcionamiento del método de compresión en Python con señales de NEDA, y posteriormente se ha implementado en NUMEXO2. El diseño de este bloque de firmware está disponible en el siguiente repositorio: https://github.com/jmdeltoro/trace\_compression\_NEDA

## Sistema de condición de doble disparo

Las celdas de NEDA muestran sensibilidad a los neutrones, rayos X y rayos gamma. Si bien el blindaje reduce la interferencia de rayos X, resulta poco práctico para rayos gamma de mayor energía sin comprometer la eficiencia de detección de neutrones. Los rayos gamma detectados por NEDA se pueden clasificar en dos tipos, rayos gamma inmediatos y rayos gamma no correlacionados. Las descripciones de estos tipos se explican a continuación:

- Los rayos gamma inmediatos son rayos gamma emitidos inmediatamente después de una reacción nuclear. Por lo general, son emitidos por núcleos atómicos en un estado excitado que se desintegra a un estado de menor energía, liberando el exceso de energía.
- Los rayos gamma no correlacionados son rayos gamma que no tienen una relación causal directa con la reacción nuclear del experimento. Pueden provenir de varias fuentes, como la radiación cósmica, la desexcitación de núcleos radiactivos o la interacción de partículas cargadas (como protones, partículas alfa o electrones) con la materia. En los experimentos de física nuclear, los rayos gamma no correlacionados pueden

representar un fondo o ruido que debe tenerse en cuenta al analizar los datos.

Dada esta característica de las celdas de NEDA, resulta esencial desarrollar técnicas para discriminar entre rayos gamma (rápidos y no correlacionados) y eventos de neutrones para determinar el tipo de radiación. En NEDA, el análisis de forma de pulso (PSA) basado en información de CC (Charge Comparison) y TOF (Time of Flight) se utiliza para la discriminación neutrongamma.

El sistema propuesto combina la relación CC con información adicional del evento para aceptar neutrones de baja energía mientras se reducen las solicitudes de disparo. Esta información adicional es el TOF de cada partícula. Con la información de TOF, también es posible identificar los rayos gamma instantáneos, ya que su TOF es cercano a cero. En contraste, los neutrones tienen un TOF mayor. Para NEDA, el TOF se mide como la diferencia de tiempo entre una señal lógica externa, como la señal de radiofrecuencia del haz (STOP), y la señal generada dentro de la celda de NEDA (START).

La introducción de este método de disparo permite el uso de dos señales de disparo independientes que se pueden combinar para generar un disparo final. En primer lugar, los neutrones de baja energía, indetectables por un sistema basado únicamente en CC, pueden ser capturados usando una lógica OR para combinar ambas señales de disparo. En segundo lugar, estas dos señales se pueden integrar con una lógica AND para disminuir la alta tasa de conteo causada por eventos de rayos gamma instantáneos.

En consecuencia, se implementan cuatro modos de disparo para los experimentos de NEDA, permitiendo la personalización del método de disparo para los objetivos específicos de cada experimento. Los modos implementados son:

- Modo CC: Solo se utiliza el disparo generado por CC.
- Modo TOF: Solo se considera el disparo basado en TOF.
- Modo AND: Se genera una señal de disparo cuando ambos métodos generan un disparo.
- Modo OR: Se genera una señal de disparo cuando cualquiera de los dos métodos genera un disparo.

Como se ha mencionado anteriormente, el componente central de la electrónica de NEDA es el digitalizador NUMEXO2, que cuenta con una FPGA Virtex-6 y una FPGA Virtex-5. El diseño del nuevo sistema de condición de doble disparo se ha implementado en la Virtex-6, utilizando las salidas de señales de disparo obtenidas de manera independiente como entradas. El digitalizador NUMEXO2 tiene 16 canales de adquisición, por lo que esta nueva funcionalidad se ha implementado de manera independiente en cada canal. Se ha

prestado especial atención a la optimización del código y a la minimización del uso de recursos de la FPGA, ya que la FPGA ya operaba al 70% de su capacidad.

El diseño de estos nuevos métodos se ha sometido a un test de funcionalidad. El objetivo de la prueba funcional ha sido evaluar el rendimiento de la implementación del doble disparador examinando el rendimiento del firmware de los modos de disparo. En concreto, la prueba ha verificado si, durante la adquisición en línea, los modos de disparo CC, TOF, AND y OR descartaban correctamente los eventos que se encontraban fuera de los umbrales establecidos y retenían los eventos que se encontraban dentro de ellos.

Después de comprobar el correcto funcionamiento, los cuatro modos de disparo también fueron utilizados en un experimento con haz. En éste se ha evaluado la influencia de cada modo de disparo después de realizar un análisis offline y la discriminación neutrón-gamma. El análisis se ha centrado en cómo los modos de disparo AND y OR, integrado las señales del disparo CC y TOF, afectaron la cantidad de neutrones aceptados después del análisis PSA (Pulse Shape Analysis) offline, en comparación con el escenario en el que solo se ha utilizado el modo de disparo CC online.

#### Reconstrucción de pulsos apilados

La superposición o apilamiento de pulsos es un problema frecuente en los experimentos de reacciones nucleares y espectroscopía con altas tasas de conteo. Este efecto ocurre cuando los pulsos llegan tan cerca en el tiempo que se superponen total o parcialmente. Como resultado, los pulsos se distorsionan. Esta distorsión compromete la calidad de la información de energía y tiempo, haciendo difícil identificar los tipos de partículas mediante las técnicas usuales de discriminación de formas de pulso. En consecuencia, los pulsos apilados se descartan típicamente.

Se ha propuesto un método de reconstrucción online de pulsos apilados capaz de recuperar pulsos con una diferencia de tiempo de 15 ns o más (3 muestras a 200 MHz). Para garantizar la viabilidad, el método debe tener baja complejidad analítica y computacional y un tiempo de reconstrucción corto por evento para integrarse sin problemas en el sistema de análisis general.

Los pulsos apilados se rechazan durante el análisis offline por lo que el CC offline de estos eventos no se lleva a cabo. Este trabajo tiene como objetivo implementar un método de reconstrucción de pulsos que cumpla con todos los requisitos mencionados anteriormente para ser incluido en la cadena de adquisición antes del análisis fuera de línea y verificar su viabilidad y eficiencia. El objetivo futuro es implementar el método de reconstrucción en el digitalizador. En esta tesis se propone un método ad-hoc utilizando un 1D-CAE (One-Dimensional Convolutional Autoencoder) para separar los dos pulsos que componen cada evento apilado adquirido con los detectores NEDA.

La arquitectura 1D-CAE propuesta sigue la estructura habitual de un 1D-CAE, pero con la particularidad de que tiene una única entrada, que es la señal que contiene los dos pulsos de apilamiento, pero dos salidas, cada una correspondiente a uno de los pulsos en la señal de entrada. Para este propósito, la estructura del codificador se comparte y el decodificador se bifurca, resultando en un decodificador separado para cada pulso reconstruido. Esta estructura permite al modelo capturar y reconstruir patrones complejos de la señal de entrada mientras proporciona dos señales de salida distintas. El diseño completo está disponible en el siguiente repositorio: https://github.com/jmdeltoro/pile-up\_reconstruction\_NEDA

Para el entrenamiento del modelo propuesto, se ha creado una base de datos de eventos con pulsos apilados de forma artificial, de modo que se conocen los dos pulsos que forman el evento apilado. Las dos combinaciones de pulsos que se han generado han sido neutron-gamma y gamma-neutron porque no todas las combinaciones son igualmente probables o detectables como señales de apilamiento. La combinación neutrón-neutrón, donde dos neutrones llegan al mismo detector, tiene una baja probabilidad de ocurrir, con una diferencia de tiempo típicamente menor a 5 ns, lo que hace que el análisis lo identifique como un solo neutrón, por lo tanto, no detectando el apilamiento. La combinación gamma-gamma es más probable; sin embargo, si dos rayos gamma llegan al mismo detector simultáneamente después de la reacción, se identificarán como un solo rayo gamma. La combinación neutrón-gamma es probable cuando un neutrón se detecta primero, seguido de un rayo gamma espurio de la radiación de fondo natural. Este rayo gamma puede aparecer en cualquier momento durante la señal adquirida. Finalmente, los eventos de apilamiento gamma-neutrón ocurren cuando los rayos gamma de la reacción se detectan primero, seguidos de un neutrón. Se observará un TOF más largo o más corto dependiendo de la distancia del detector a la reacción. Con la configuración estándar de NEDA, la distancia típica es de 100 cm, resultando en un tiempo de vuelo promedio de neutrón de 40 ns. Dadas estas características, la reconstrucción de pulsos apilados se ha centrado en eventos gamma-neutrón o neutrón-gamma.

Una vez entrenado el modelo 1D-CAE se ha evaluado el nivel de similitud entre los pulsos originales y reconstruidos, y también se ha comprobado el éxito al determinar el tipo de partícula utilizando el método de CC con las señales reconstruidas y las originales.

## Conclusiones

En esta tesis se han implementado con éxito diversos avances en el sistema de detectores de neutrones NEDA para mejorar sus capacidades de adquisición y análisis de datos en el contexto de la espectroscopia de rayos gamma. A continuación se resumen los principales logros y conclusiones de cada una de

las nuevas funcionalidades implementadas.

- Compresión de datos en línea sin pérdida: Se implementó el método de codificación diferencial con número fijo de bits, logrando una relación de compresión de 1,6 y ahorrando un 37,5% de espacio de almacenamiento. Esto permite un aumento significativo en la tasa de conteo sin superar la velocidad máxima de transmisión de 409,6 MB/s. A pesar de no estar totalmente optimizado debido a las limitaciones del DMA, se demostró con éxito la compresión y descompresión de trazas de eventos.
- Sistema de doble condición de disparo: Se desarrolló un sistema de doble condición de disparo, combinando medidas de comparación de carga (CC) y tiempo de vuelo (TOF) para discriminar eficazmente entre rayos gamma y neutrones. Se evaluaron cuatro modos de disparo (CC, TOF, AND y OR) utilizando datos del experimento E703 en GANIL. El modo AND es útil para reducir las solicitudes de disparo, mientras que el modo OR minimiza la pérdida de neutrones cuando se pueden manejar tasas de solicitud de disparo más altas. Estos modos de disparo ofrecen una mayor versatilidad para adaptar el sistema de detección a los objetivos experimentales específicos.
- Reconstrucción de apilamiento de pulsos: Se implementó un método novedoso que utiliza un autocodificador convolucional unidimensional (1D-CAE) para reconstruir eventos de apilamiento, mostrando una tasa de éxito del 83,95% en la reconstrucción precisa de estos eventos. Este método conserva información crucial previamente perdida en eventos de apilamiento y mantiene una alta correlación promedio de 0,988 con las señales originales. Ofrece una solución práctica para el procesamiento de señales en tiempo real en futuras actualizaciones de NEDA.

En general, los resultados de esta tesis mejoran las capacidades de adquisición y análisis de datos de NEDA, lo que permite estudios de reacción y espectroscopía nuclear más precisos y eficientes. Los avances en la compresión de datos, el sistema de condición de doble disparo y la reconstrucción de acumulación de pulsos optimizan colectivamente el rendimiento de NEDA, posicionándolo como una herramienta poderosa para la futura investigación en física nuclear.



UNIVERSITAT DE VALÈNCIA DEPARTAMENT D'ENGINYERIA ELECTRÒNICA

## Contents

A	ckno	wledgments				VII
$\mathbf{A}$	bstra	act				IX
R	esum	nen			X	III
1	Inti	roduction				1
	1.1	Introduction				1
	1.2	Objectives				2
	1.3	Methodology				3
2	Nuc	clear Gamma-ray spectroscopy				5
	2.1	Introduction				5
	2.2	Exotic nuclei				6
	2.3	High-resolution Gamma-ray spectroscopy				7
		2.3.1 High-resolution Gamma-ray spectroscopy detector	$\mathbf{S}$			8
		2.3.2 Ancillary detectors				9
	2.4	Gamma spectroscopy physical processes				10
		2.4.1 Gamma radiation interaction with matter				10
		2.4.2 Neutron Interaction with matter				12
3	NE	DA detector				13
	3.1	NEDA				13
		3.1.1 NEDA detection mechanism				15
		3.1.2 NEDA construction				21
		3.1.3 NEDA electronics			•	23
4	The	e NUMEXO2 digitiser				<b>25</b>
	4.1	Description of the NUMEXO2				25
	4.2	The FADC Mezzanine				27
	4.3	Virtex-6 design				27
		4.3.1 ISERDES				29
		4.3.2 Digital Signal Processing				30
		4.3.3 Data management				32

		4.3.4 Setup Registers	33
	4.4	Virtex-5 design	34
5	Loss	sless data compression for data acquisition	37
	5.1	Introduction	37
	J	5.1.1 Implementation considerations for data compression in	•
		NUMEXO2	38
	5.2	Lossless compression methods	40
	5.3	Python implementation	45
	5.4	Firmware implementation	48
	5.5	Test and results	54
	5.6	Conclusions	58
c	Dox	ble Trigger condition gratery	61
6	6.1	ble Trigger condition system	61
	0.1	Introduction	63
	c o	* v	64
	6.2 6.3	Firmware implementation	66
	6.4	In-beam results	69
	6.5	Conclusions	73
	0.5	Conclusions	10
7		-up reconstruction using a 1D-CAE	<b>75</b>
	7.1	Introduction	75
	7.2	Pile-up in NEDA detector	77
	7.3	1D-CAE architecture for NEDA pile-up event reconstruction .	78
		7.3.1 1D-CNN	79
		7.3.2 Autoencoder	80
		7.3.3 1D-CAE architecture and training	80
	7.4	Dataset preparation	82
		7.4.1 Data acquisition	83
		7.4.2 Analysis and dataset generation	83
	7.5	Analysis of reconstructed signals	84
	7.6	Conclusions and future work	88
8	Con	clusions	89
Lis	$\mathbf{st}$ of	Figures	91
ΔΙ			
71	obre	viations	94

## Chapter 1

## Introduction

This initial chapter aims to introduce the research performed for this Ph.D. thesis. It is dedicated to presenting the motivation for the study, the set objectives, and the methodology employed to complete the research.

## 1.1 Introduction

The atomic nucleus, the enigmatic heart of matter that composes our universe, has captivated human curiosity and research for centuries. As our understanding of nuclear physics deepens, it raises increasingly complex questions, demanding the development of more sophisticated tools and technologies. In order to unravel the mysteries of the atomic nucleus, physicists from the 1960s to the present day have been working using gamma-ray spectroscopy, which uses the detection of gamma-rays to obtain properties of the atomic nucleus.

Technological advances have led to improvements in gamma-ray detection methods, including high-resolution gamma spectroscopy techniques that improve energy measurements and help develop more reliable nuclear models. To perform this high-resolution gamma spectroscopy, physicists and engineers have developed detection instruments such as the following: EUROBALL [1], GAMMASPHERE [2], MINIBALL [3], EXOGAM [4], AGATA [5] and GRETA [6]. These instruments are often coupled with ancillary neutron detectors such as Neutron Wall [7], NEDA [8], and charged-particle detectors such as GRIT [9] and DIAMANT [10], among others, in order to obtain information regarding the reaction channel.

The development of these instruments, which obtain high-resolution spectra, involves a great deal of design complexity, where the geometry and material of the detector and the electronics involved are key. Originally, analogue electronic systems were used to process the pulse signals from the detectors. These systems provided good time resolution and energy measurements. However, analogue electronics have less flexibility when implementing new functionalities and algorithms and are generally more susceptible electromag-

netically than digital electronics. This has led to the increasing use of digital electronics, where more complex PSA (Pulse-Shape Analysis) algorithms, data throughput, high-speed communications, and firmware reconfiguration can be implemented more feasibly. Furthermore, given the flexibility of digital electronics, different instruments can be developed where part of the electronics is common. As an example, a synergy was achieved in the front-end electronics of EXOGAM and NEDA, which led to the design of a common digitiser and preprocessing electronics, the so-called NUMEXO2.

In this thesis, new methods are investigated and developed to improve the efficiency of the NEDA detector and increase the acquisition capabilities. On the one hand, to enhance NEDA efficiency, a double trigger condition system is implemented to improve neutron/gamma discrimination (NGD). On the other hand, to increase acquisition capabilities, a lossless online compression method is developed to increase the data acquisition rate without needing to modify the hardware. Increasing the data acquisition rate increases the probability of acquiring pile-up events. In this context, reconstructing and analysing pile-up events becomes crucial. A NEDA pile-up event reconstruction method based on a machine learning technique is evaluated to avoid losing pile-up events.

## 1.2 Objectives

This section summarises the main objectives of the thesis, considering the environment in which it is developed.

- Background study: An essential study of the scientific framework in which NEDA is involved will be carried out, as well as the structure, electronics, and designs previously implemented.
- Lossless data compression online: Study of the different existing compression methods and develop of a lossless compression method to reduce storage size and offer the possibility of increase the counting rate in NEDA experiments.
- Double Trigger condition system: Develop a trigger condition system that enhances the previously implemented neutron-gamma discrimination acquisition capabilities and study its effect in the data analysis. In order to carry out this improvement, the electronics involved in NEDA will be studied in detail, mainly the firmware already implemented in NUMEXO2.
- Reconstruction of piled-up pulses: Pulse pile-up is a problem in nuclear spectroscopy and nuclear reaction studies that occurs when two pulses overlap and distort each other, degrading the quality of energy and timing information. Therefore, the last objective of this thesis is to

study the different methods of pulse separation and reconstruction, and to offer a new method of pulse reconstruction based on machine learning techniques.

## 1.3 Methodology

The methodology used in this thesis is differentiated for each of the objectives to achieve. The procedure applied to each objective is detailed below.

- Background study: The initial task, which serves not only to familiarise oneself with the design specifications in NEDA but also to acquire fundamental background knowledge relevant to the experiment's objectives, involves exploring the experimental environment and its fundamental physics. Consequently, this includes a descriptive overview of nuclear gamma-ray spectroscopy and the neutron interactions of radiation with matter. Also, part of the background is the detailed study of the structure of the NEDA detector and its front-end electronics.
- Lossless data compression online: Data compression is a field of research that has been studied since the 1940s. Numerous compression methods have been developed to date, so the first step is to study the most relevant ones and investigate which method to develop for implementation in NEDA electronics. Among the different methods developed so far, the study will focus on the lossless compression methods as it is not desirable to lose event information. Once the compression method is selected, it is developed in Python using real experiment data to test its validity. The method will later be implemented in the NUMEXO2 digitiser. Finally, tests are carried out to verify the effectiveness of the online lossless data compression method.
- Double Trigger condition system: In order to develop the double trigger condition system, the first step is to study the firmware implemented in NUMEXO2. Then, choosing which of the two FPGAs (Virtex-5 and Virtex-6) of NUMEXO2 has to house the new trigger system. After this, system must be implemented and tested in the laboratory to verify its correct operation. Finally, this system has to be used in in-beam experiments, and a study of the impact of the new trigger system on the data analysed has to be carried out.
- Reconstruction of piled-up pulses: Signals with piled-up pulses are usually discarded as the pulse information is distorted. In this case, the reconstruction of pulses will be carried out using machine learning techniques using signals from NEDA detector. First, different ways and methods to separate and reconstruct the pile-up pulses are studied.

Subsequently, the state of the art regarding machine learning techniques have been studied, and the most appropriate technique to separate and reconstruct the signals has been chosen. Subsequently, a database of NEDA signals is created to train and test the chosen machine learning model. Finally, the reconstruction method is evaluated by analysing its effectiveness in reconstructing the pile-up pulses as faithfully as possible.

## Chapter 2

# Nuclear Gamma-ray spectroscopy

This chapter introduces the concept of gamma spectroscopy and highlights its significance in nuclear structure research. It provides a concise overview of the fundamental principles of physics to set the necessary concepts for the thesis. The focus is on High-resolution Gamma-ray spectroscopy and its detectors and ancillary detectors to improve spectroscopy performance.

### 2.1 Introduction

The first identification of high-energy photons occurred in November 1895 when Roentgen discovered X-rays during his experiments with cathode ray tubes [11]. Additionally, in the subsequent year, Becquerel demonstrated the existence of radiation by observing a photographic plate darkening solely through exposure to uranium salt without any sunlight. This discovery marked the inception of radiation detection, and Marie Curie further improved the detection method by utilising the piezoelectric effect of quartz, ultimately recognising radiation as a general phenomenon in radioactive substances [12]. These scientific advances paved the way for the concept of the nucleus as the radiation source in 1911, starting a new era of scientific exploration. This idea was developed thanks to Rutherford's contributions to nuclear structure and the experiments carried out by Geiger and Marsden. However, experiments in the 1940s and 1950s later revealed that nuclei were no longer considered the fundamental units of the universe, as once believed [13]. Nuclear gamma-ray spectroscopy involves quantitatively analysing photon spectra emitted by a nucleus. These gamma-ray photons originate during transitions of nucleons (protons and/or neutrons) between quantised states within the nucleus, occupying the high-energy portion of the electromagnetic spectrum. Gamma-ray spectroscopy techniques offer the possibility to measure the fundamental nuclear properties of excited nuclear states, including excitation energy, angular momentum (spin) and parity, by applying conservation laws and electromagnetic selection rules. Moreover, by determining decay probabilities of nuclear states through lifetime measurements, one can gain direct insights into the relationships between the initial and final states within the nucleus. Understanding of the nucleus is advancing, and its complexity is becoming more evident. The need for more accurate and complete information from detectors is growing as they serve as a window into the intricate realm of matter.

## 2.2 Exotic nuclei

In the contemporary scientific understanding of matter, it is acknowledged that matter is composed of numerous fundamental particles, including those that were previously posited as constituents of the atomic nucleus. In the natural world, independently of its physical state, a central nucleus characterises every chemical element, a positive electric charge, and an ensemble of electrons distributed within quantised atomic layers, each with a negative charge. The configuration of these electron shells significantly governs the element's electrochemical and atomic attributes.

The nucleus, essential in early radiation detection, comprises several particles, specifically protons and neutrons. The cumulative particle count within the nucleus is the mass number (A). The mass number provides an approximate measure of the total mass of a nucleus due to the comparable masses of protons and neutrons. While protons have a positive charge, neutrons exhibit neutrality, and their presence is essential for stabilising the nucleus.

The atomic number (Z), corresponding to the number of protons, carries fundamental significance in determining the true identity of an element due to its fundamental role in chemical properties. In parallel, the number of neutrons (N) gives rise to a series of isotopes, representing elements with identical chemical characteristics and nomenclature but varying neutron counts. Consequently, these isotopes display divergent nuclear attributes, half-life, and energy levels. This extension of the periodic table, based on chemical or atomic criteria, is shown in the Table of Nuclides (Segré Chart), as exemplified in Fig. 2.1.

This graphical representation was first introduced by Giorgio Fea in 1935 and later expanded upon by Emilio Segré in 1945. Since then, it has become an essential tool for nuclear physicists. Approximately 300 stable nuclei and around 3,000 different unstable nuclei have been identified so far, with the possibility of up to 6,000 isotopes.

The Segré Chart is illustrated with stable nuclei shown in black as they cross the  $\beta$ -stability line. To the left, a set of isotopes marked in blue represents proton-rich nuclei, which are unstable and have fewer neutrons than stable ones. To the right, their homologous in pink represent neutron-rich nuclei,

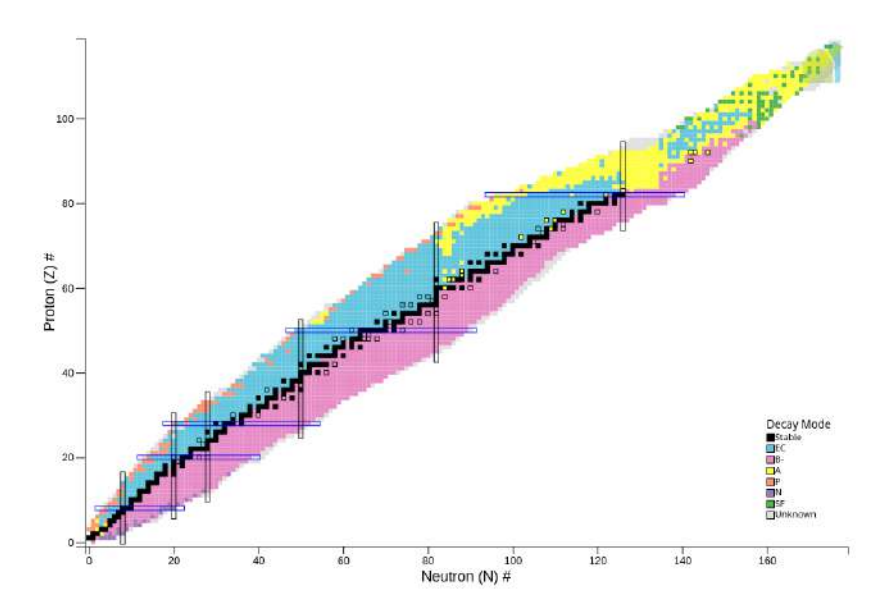


**Figure 2.1:** Table of nuclides with the stable elements in black and for the other nuclides the colour indicates the type of decay (or radiation) happening in the unstable nuclei, i.e. red:  $\beta+$ , blue: $\beta-$ , orange: proton-decay, yellow:  $\alpha$ -decay, purple: neutron-emitters

characterised by an excess of neutrons. Exotic nuclei, those with a neutron-to-proton (N/Z) ratio significantly different from the typical natural nuclei, are limited by the neutron and proton drip-lines, beyond which no isotopes can exist.

Research on the proton drip-line has well-established values for a significant portion of the elements [14]. However, the most neutron-rich and heaviest nuclei, corresponding to the drip-line nuclei, are <sup>31</sup>F and <sup>34</sup>Ne for fluorine and neon, respectively. So, the location of the neutron drip-line is in Z=10 [15].

## 2.3 High-resolution Gamma-ray spectroscopy

According to quantum mechanics, an excited nucleus is a nucleus with a higher energy than its ground state, where the ground state is the one whose energy is the lowest for a certain nucleus [14, 16]. Any excited nucleus can emit radiation in different ways before reaching its ground state.

Different decay modes could be observed in nuclei, including, among others, gamma-ray emission, internal conversion, alpha emission, neutron emission,  $\beta$ + emission,  $\beta$ -emission, electron capture, fission, etc. The ones related to the de-excitation of the nucleus itself correspond to decay between different excitation energies in the same nucleus. The decay modes involving weak interaction and/or particle emission also modify the nucleus that emits the

radiation. The most common technique to obtain the energy level scheme of a nucleus is the so-called gamma-ray spectroscopy. Gamma-ray spectroscopy is a method used in nuclear physics to investigate nuclei through the energy spectra of the gamma-rays emitted during de-excitation.

The capability to distinguish these levels in the decay scheme is directly connected to the spectrometer's capability to distinguish between two gamma rays of slightly different energy. This property is known as energy resolution and is a must for a specific branch of gamma spectroscopy known as high-resolution gamma spectroscopy.

### 2.3.1 High-resolution Gamma-ray spectroscopy detectors

The journey of gamma-ray spectroscopy started with the revelation of radioactivity by Henri Becquerel in 1896. Hans Geiger, in 1908, introduced the first practical technique to quantify radioactivity and invented the Geiger counter. This instrument, which leveraged the ionisation of gas by radiation under a high electric field, could detect alpha and beta particles and gamma-rays. However, it could not distinguish between different types of particles or their energies.

The evolution of experiments and detectors has been significant, beginning with early models in the 1960s that used NaI(Tl) scintillators. This evolution continued with Si(Li) and Ge(Li) detectors, which could not distinguish very well between different types of particles or their energies. Ultimately, the High-purity Germanium (HPGe) detectors were developed, achieving a high distinguish ability and thus being able to perform high-resolution gamma-ray spectroscopy. For a comprehensive history of gamma spectroscopy, please refer to [17].

HPGe based detectors play a crucial role in high-resolution gamma-spectroscopy due to their exceptional energy resolution. They have been effectively utilised in high-resolution spectroscopy projects like EXOGAM [4] or EUROBALL [1], leading to discoveries such as new decay modes of superdeformed nuclei, high-spin spectroscopy, search of symmetries in N $\approx$ Z nuclei, etc. Other materials commonly used in gamma-spectroscopy include LaBr3(Ce), NaI(Tl), and CsI(Tl) [18] inorganic scintillators. However, their energy resolution is not comparable to that of HP-Ge, making the semiconductor's resolution ( $\approx 0.2-0.8\%$ ) an order of magnitude higher than scintillators (> 3 – 5%). Figure 2.2 compares the energy resolution of a  $^{60}$ Co gamma spectrum using HP-Ge and NaI(Tl), demonstrating the performance difference between the two materials.

While HP-Ge detectors have many beneficial features, they also have some disadvantages. The material is expensive, and its small energy gap (around 0.7 eV) renders it unusable at room temperature. This necessitates using a constant supply of costly liquid nitrogen to keep them cool. In addition,

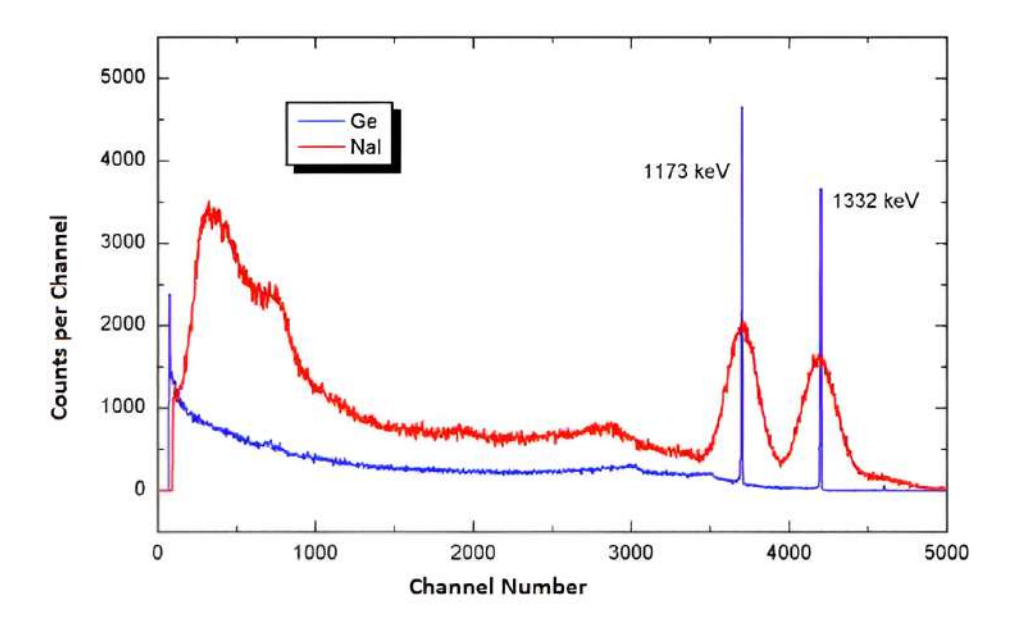


**Figure 2.2:** Comparison of the <sup>60</sup>Co gamma spectrum between HP-Ge (blue) and NaI (red) [19].

large-volume HP-Ge detectors typically have limited time resolutions, around 8-10 ns, due to the dependence on the position of the gamma-ray's impact in the detector [20]. When experiments require faster responses, around  $\approx 1$  ns, scintillators are more appropriate and have higher efficiency than HP-Ge detectors.

In recent years, technological advancements such as the segmentation of Ge detectors, pulse shape analysis techniques, and gamma-ray tracking have led to the emergence of the newest generation of spectrometers: AGATA [5] in Europe and GRETA [6] in the USA. These advanced spectrometers not only measure energy, position, and time; they also trace the path of scattered gamma-rays, improving overall efficiency.

## 2.3.2 Ancillary detectors

As mentioned before, studying gamma energy spectra is crucial in identifying various characteristics of a specific nucleus. However, there are instances where the data derived from gamma energy spectra may need to be improved due to constraints in the instrument's sensitivity. This calls for the employment of additional detectors.

An ancillary detector is a device that combined with a gamma spectrometer can offer more comprehensive into the reaction channel or the mode of deexcitation. This combination allows to identify the isotope being studied or to gather additional data. Neutron and charged particle detectors are among the most common ancillary detectors. In nuclear physics, NEDA, which is the focus of this thesis, and Neutron Wall are notable examples of neutron detection arrays. At the same time, GRIT and DIAMANT are examples of charge-particle detection arrays.

Several experiments employing coupled detectors take place at GANIL laboratory (Grand Accélérateur National d'Ions Lourds) in Caen and LNL (Laboratori Nazionali di Legnaro) in Legnaro. These experiments use EXOGAM, along with the Neutron Wall and DIAMANT detectors. Also, at GANIL and SPES at LNL, NEDA detector is coupled with AGATA, EXOGAM, and TRACE detectors.

## 2.4 Gamma spectroscopy physical processes

The following paragraphs provide a descriptive explanation of the primary physical processes involved in gamma radiation detectors and neutron detectors such as NEDA. This section explains the mechanisms of photon matter and neutron matter, specifically focusing on the predominant phenomena found in high-resolution gamma spectroscopy.

#### 2.4.1 Gamma radiation interaction with matter

Understanding the interactions between gamma rays and matter is necessary to optimise information extraction from gamma rays in an experiment. This knowledge is crucial for assessing the desired radiation and identifying and mitigating unwanted sources of radiation that might compromise the accuracy of our measurements. When high-energy photons encounter matter, they can suffer one of three distinct interactions

- Photoelectric Absorption The photoelectric effect takes centre stage in the low-energy range of the gamma spectrum. In this phenomenon, the energy of the gamma-ray is intricately linked to both the incoming photon's energy and the electron's binding energy within the atom. Consequently, the electron is expelled from its bound state with the residual kinetic energy. Subsequently, this secondary electron discharges its energy through electromagnetic interactions with the surrounding medium.
- Compton Scattering: This significant phenomenon prevails within the mid-energy range of the gamma spectrum, typically ranging from 1 to a few MeV. During this process, a gamma ray transfers a portion of its energy to an electron, manifesting as kinetic energy. This interaction generates a new photon, with its energy level determined by the difference in energies involved in the scattering event.
- Pair Production: The pair production effect dominates at high energy levels within the gamma spectrum, typically occurring at energies

exceeding 10 MeV. When photons possess energies exceeding the combined mass of two electrons and are influenced by the electric field of a nucleus, they can transform into a pair of electrons and positrons. The excess energy exceeding 1.022 MeV, the threshold for pair production, is directly converted into the kinetic energy of these newly created particles.

Figure 2.3 illustrates the regions of interaction and provides information about their impact on spectra. The low-energy area has decreasing Photoelectric Absorption. In the central area, Compton scattering predominates, while at higher energies, pair production dominates. The likelihood (cross-section) of these interactions depends on the gamma-ray's energy and the material's atomic number. The total cross-section of the interaction of gamma rays with an atom is equal to the sum of all three mentioned partial cross-sections:

$$\sigma = \sigma_f + \sigma_C + \sigma_p \tag{2.1}$$

 $\sigma_f$  is the cross-section of the photoelectric effect,  $\sigma_C$  that of Compton scattering and  $\sigma_p$  that of pair production.

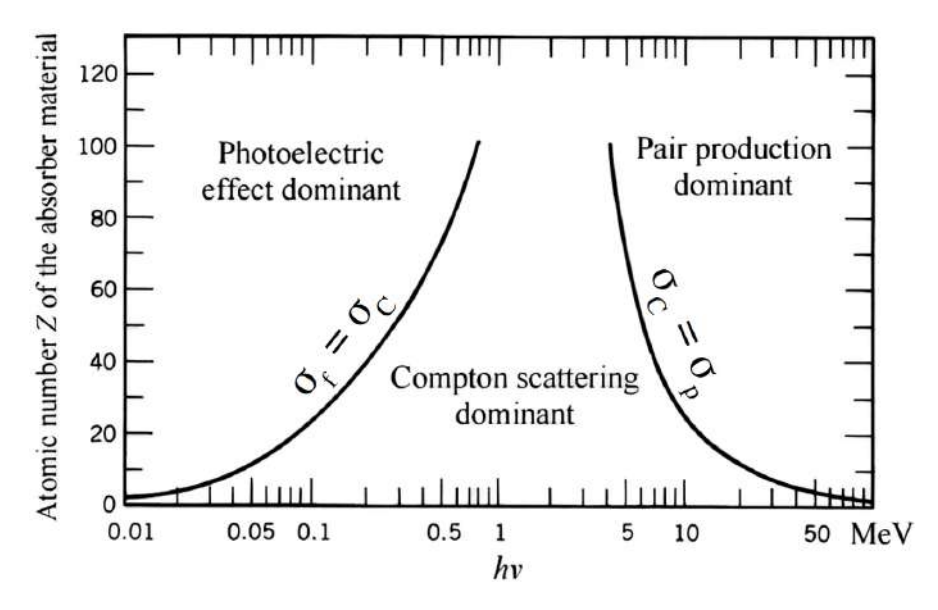


Figure 2.3: Attenuation coefficients for gamma ray in relation with atomic number Z of absorbed material [21].

In summary, a comprehensive understanding of these mechanisms is crucial for optimising data extraction from gamma rays and discerning and mitigating any undesirable radiation sources that may affect our measurements' precision.

#### 2.4.2 Neutron Interaction with matter

Detecting neutrons poses unique challenges due to their lack of electric charge, which renders them unaffected by Coulomb processes. Unlike gammarays, neutrons do not directly interact with electrons. Instead, their interactions predominantly occur with atomic nuclei, resulting in the release of charged particles and triggering various nuclear reactions [22]. Depending on neutrons' energy, several scenarios can be considered. There are two primary types of interactions: scattering and absorption processes. Let's delve into these interactions more systematically.

- Scattering Mechanisms: Scattering mechanisms are prevalent, particularly in the MeV energy range [23], where a neutron carries enough energy to transfer a significant amount of kinetic energy during a single collision with a nucleus. Subsequently, the neutron undergoes moderation, slowing down and losing energy with each collision. Within scattering processes, two distinctions are notable:
  - Elastic Scattering A(n,n)A: The nucleus does not transition to an excited state following the collision with the neutron.
  - Inelastic Scattering  $A(n, n')A^*$ : In inelastic scattering, the involved nucleus may transition to an excited state after the collision with the neutron, mainly when the neutron energy is exceptionally high (>1 MeV). This results in the nucleus undergoing an internal rearrangement and emitting radiation. For neutron detectors, scattering mechanisms involving light nuclei like hydrogen or helium are preferred.
- Neutron Absorption: A second type of neutron interaction occurs when a neutron is captured or absorbed by a nucleus, leading to a diverse array of possibilities. Typical effects include the emission of a proton, deuteron, alpha particle, or fission products after neutron capture/absorption, as well as the radiative capture reaction of neutrons. Neutrons can be indirectly detected through secondary processes involving the emission of gammas or charged particles after neutron capture/absorption. The cross-section for absorption processes is more relevant for thermal and slow neutrons (~0.025 eV), while scattering processes gain prominence for fast neutrons (>1 MeV) [14,23]

Depending on the energy range of the neutrons, various methods can be used to detect them. Some examples include detecting slow neutrons through ionised <sup>3</sup>He or BF<sub>3</sub> chambers. For fast neutron detection, standard methods involve <sup>4</sup>He and CH<sub>4</sub> [22], scintillation produced in lithium glass fibres [14], and, as seen in NEDA and Neutron Wall, neutron interaction with aromatic organic scintillators [8,24].

# Chapter 3

# NEDA detector

NEDA (NEutron Detector Array) is the neutron detector upon which data acquisition improvements have been developed in this thesis. This chapter briefly introduces the NEDA detector and focuses on the detection mechanism, detector structure, and front-end electronics.

#### 3.1 NEDA

NEDA is an advanced neutron detector array developed through an international collaboration involving several institutes from nine European countries. This innovative system was conceived as the successor to the Neutron Wall detector. NEDA consists of a set of new generation neutron detectors like the one shown in Fig. 3.1 based on a liquid scintillator that can achieve high-detection efficiency, excellent neutron-gamma discrimination, high two neutrons discrimination capabilities and high counting rate capabilities that have been designed to be coupled to a set of germanium-based gamma detectors like AGATA, EXOGAM2 or GALILEO [25].

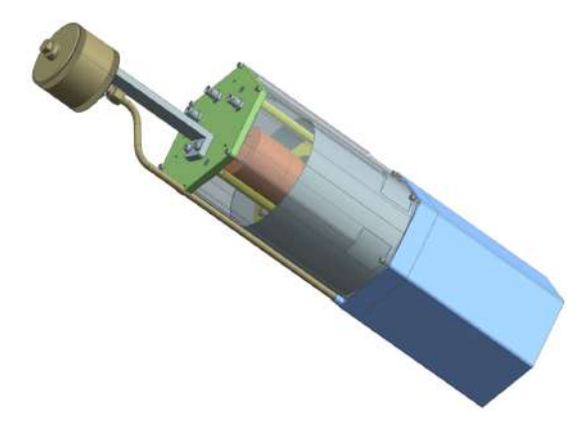


Figure 3.1: The design of a single NEDA neutron detector cell [8].

The first implementation of NEDA was carried out in conjunction with the Neutron Wall, shown in Fig. 3.2, and AGATA at GANIL. Nevertheless, the mobility of NEDA allows it to easily integrate with other gamma-ray array detectors. Neutron and charged-particle detectors play a crucial role in effectively choosing decay processes, especially when investigating neutron-deficient nuclei resulting from fusion-evaporation reactions. Furthermore, NEDA serves as an indispensable instrument for the exploration of exotic nuclei generated through transfer reactions where the emitted particle is a neutron. In the upcoming years, the availability of a diverse range of new radioactive beams for transfer reactions induced by proton- and neutron-rich projectiles will expand significantly. This expansion will be facilitated by cutting-edge radioactive beam facilities such as HIE-ISOLDE [26] (CERN, Geneva, Switzerland), SPES [27] (Legnaro, Italy), SPIRAL2 [28](Caen, France), and FAIR [29] (Darmstadt, Germany).



Figure 3.2: The NEutron Detector Array coupled to the Neutron Wall at 90° [30].

In contrast to other neutron array detectors, such as the Neutron Wall or Neutron Shell [31], NEDA enhances the efficiency of neutron detection while reducing the incidence of cross-talk or double hits from a single neutron, which can distort the actual number of neutrons emitted due to scattering.

Throughout this section we will detail the detection mechanism on which NEDA detectors is based, how the detector has been constructed, and finally the associated electronics.

#### 3.1.1 NEDA detection mechanism

The NEDA detector collects data of the reactions generated by the nucleus under examination. This process involves the detection of fast neutrons using organic scintillators. However, these scintillators are also responsive to gamma rays, necessitating the implementation of a technique to differentiate between gamma rays and neutrons.

Each NEDA cell contains an organic scintillating liquid that produces light with the interaction of neutrons and gamma rays. Through photomultipliers, this light is transformed into an electrical signal, which is subsequently analysed to determine the origin of the reaction, neutron or gamma ray. The mechanism of light production and conditioning using photomultiplier tubes is explained below.

#### Organic scintillator physics

The physics of organic scintillators in radiation detection is regarded as one of the most traditional and effective methods employed to date. This approach is used not only for gamma spectroscopy but also for detecting fast neutrons. Scintillator materials operate on the principle of converting the kinetic energy of incoming particles into light through the inherent luminescent properties of the material. Typically, scintillators must be linked to photomultipliers to yield an amplified current pulse generated from the light emitted within the detector. Figure 3.3a diagram of the scintillator next to the photomultiplier.

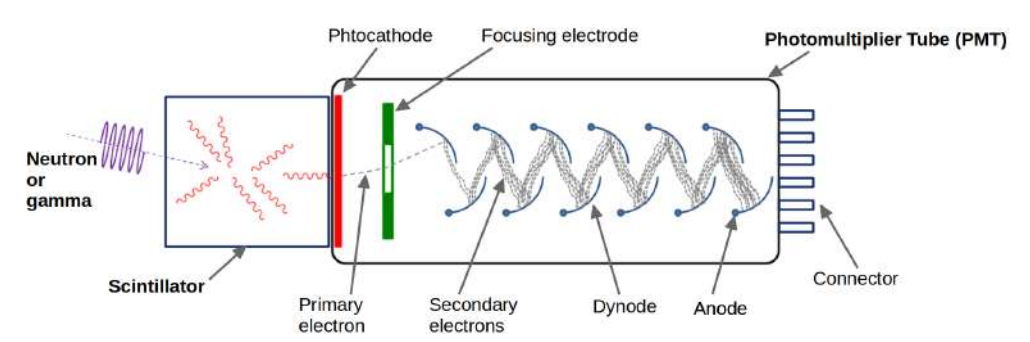
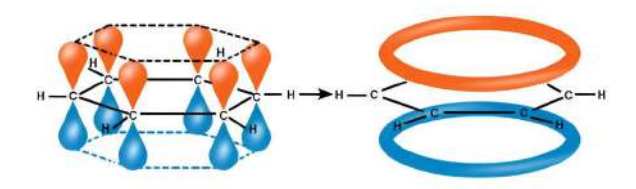


Figure 3.3: Scintillator coupled to a photomultiplier.

The scintillator materials can be classified into organic and inorganic crystals, organic liquids, plastics and gases [16]. Organic liquid scintillators are the best option for detecting fast neutrons due to their higher hydrogen content and rapid response. The organic liquid scintillator ELJEN EJ301 (equivalent to BC501A) has been selected for NEDA. This organic liquid and others, such as BC537, have the advantage of having slight differences in the responses to the different types of particles with which they interact [24], which facilitates discrimination between them.

Aromatic carbohydrates serve as the basis for organic liquid scintillators. The luminescent process creates covalent chemical bonds when two or more p orbitals from carbon atoms overlap. This overlapping leads to a delocalised system characterised by two symmetric lobes separated by a nodal plane, illustrated in Fig. 3.4 for the example of benzene.



**Figure 3.4:** Graphic representation of the delocalisation of electrons in benzene. [32].

Referring to the energy levels of the  $\pi$ -electron, specifically the  $\pi$ -electrons constituting the delocalised system, an examination of luminescence arising from their energy transitions can be conducted. The ground state will be denoted as  $S_0$ , the ionisation energy as  $I_{\pi}$ , and the excited states as  $S_1$ ,  $S_2$ ,  $S_3$ , ..., designated as singlet states. Additionally, the molecules may possess lower-state energy levels, identified as triplets, labelled as  $T_1$ ,  $T_2$ ,  $T_3$ , along with other vibrational states designated as  $S_{01}$ ,  $S_{02}$  ...,  $S_{11}$ ,  $S_{11}$ , and  $T_{01}$ ,  $T_{02}$  ...,  $T_{11}$ , associated with each singlet or triplet state. Three distinct forms of light emission can be derived within this intricate framework. Fluorescence, characterised as the swiftest decay mode, stems from transitions with decay times ranging from 1 to 10 ns.

Phosphorescence involves light emission following an energetic transition to a metastable triplet state, typically  $T_1$ , resulting in 100 microseconds and beyond decay. The last emission mode, delayed fluorescence, occurs when an energetic transition returns to a singlet state after traversing a metastable state. Typically induced by thermal effects, this transition exhibits a decay time close to 1 microsecond. Figure 3.5 schematically illustrates the energy levels of a  $\pi$ -electron.

The amalgamation of light decay modes in certain organic scintillators yields a pulse characterised by summating exponential functions with distinct time constants instead of a straightforward exponential light output response. Consequently, the temporal output signal comprises two distinct components, each ascribed to a distinct type of luminescent emission. The rapid component is dictated by the prompt fluorescence decay time, approximately within the range of a few nanoseconds. In contrast, the slow decay component predominantly arises from delayed fluorescence, characterised by a decay time in the hundreds of nanoseconds. This output signal produced by the organic scintillator is conducted to a photomultiplier and converted into an electric signal for processing in subsequent stages.

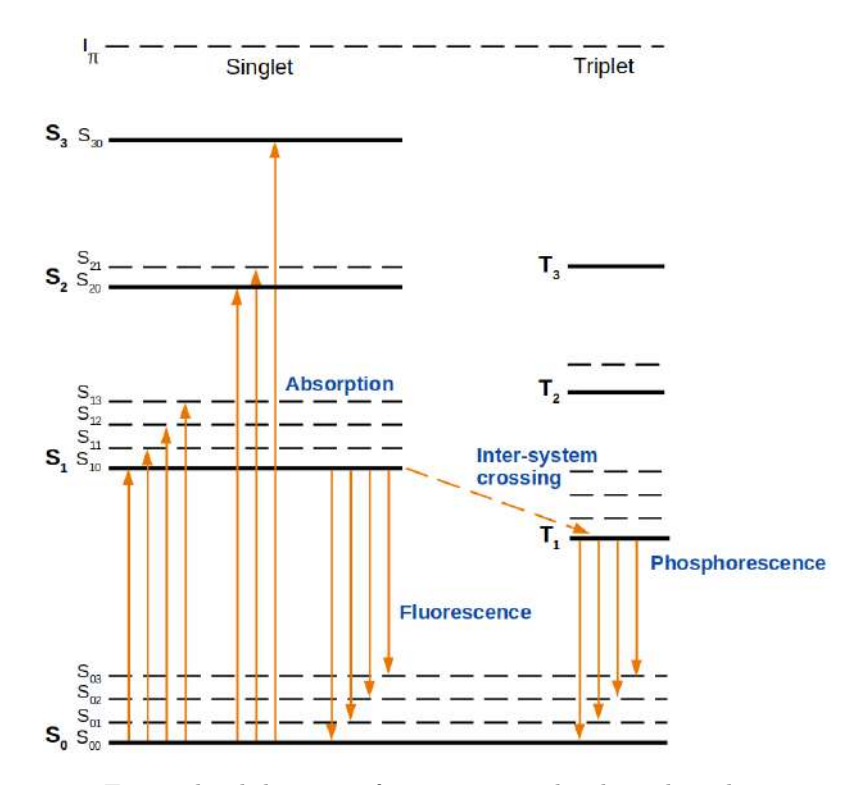


**Figure 3.5:** Energy level diagram of an organic molecule with  $\pi$ -electron structure, adapted from [33]. The singlet states with spin 0 are labelled  $S_{ab}$  and the triplet states of spin 1 are labelled  $T_{ab}$  where a indicates the excitation level and b indicates the vibrational state of that level.

## Photomultipliers

Photomultipliers (PM) or photomultiplier tubes (PMT) play a crucial role in converting light into measurable electric signals, particularly in radiation detectors coupled to scintillators. [34]. This coupling is favored due to the PM's capability to transform a weak light signal, typically around hundreds of photons, into a discernible current with minimal added noise. While newer applications explore advancements like silicon photomultipliers (SiPM), particularly in medical physics for Positron-Emission Tomography (PET) [35], photomultipliers continue to be the predominant choice for applications requiring large surface areas.

The fundamental components of a PMT include a photocathode, multiple dynodes, and an anode assembled within a vacuum tube. The photocathode emits electrons when subjected to the photoelectric effect upon light impact. These electrons traverse the set of dynodes towards the anode. The photocathode connects to the most negative potential inside the tube, while the anode links to the most positive potential. Each dynode connects to increasingly positive voltages (V1, V2, ...V8), facilitating the acceleration of electrons

from the photocathode to the anode.

Upon an electron release from the photocathode, electrons are attracted to the more positive electric field of the first dynode, resulting in impact and the release of additional electrons. This process repeats through subsequent dynodes, with electrons gaining acceleration at each stage. Finally, a substantial quantity is collected when electrons reach the last dynode and the anode. The ratio of electrons collected at the anode to those released from the photocathode determines the photomultiplier gain, typically ranging from  $10^5$  to  $10^6$  in photomultiplier tubes. Figure 3.6 illustrates the mechanism of electron collection in a photomultiplier and the specific potentials to which the dynodes and anode are connected.

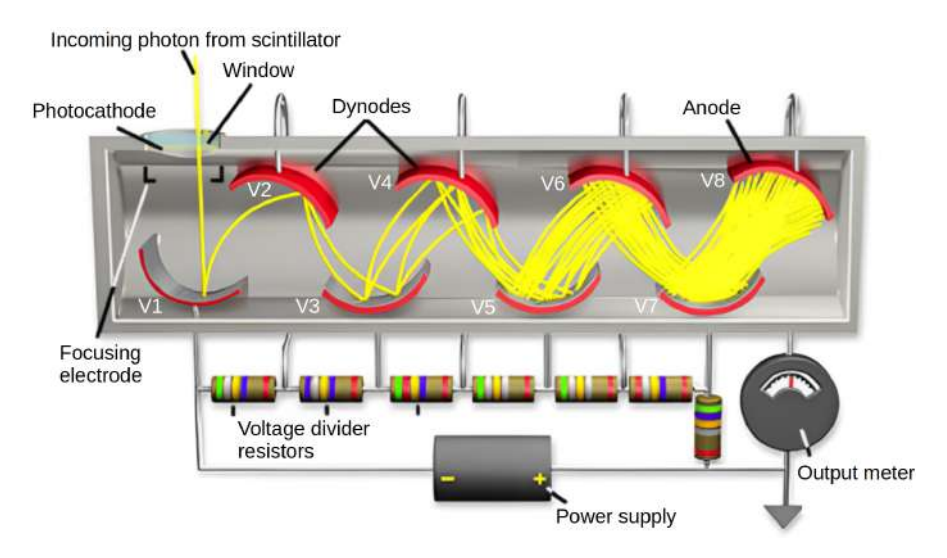


Figure 3.6: Photomultiplier schema and their electron drifting mechanism.

Regarding NEDA, a study was conducted to evaluate the optimal PMT available in the market, focusing on its ability to effectively discriminate between neutron and gamma events and achieve precise timing. This research was detailed in citation [36, 37], and the Hamamatsu R11833-100 PMT with a super bialkali photocathode was selected.

## Neutron-gamma discrimination

As previously mentioned, although the main light generation comes from the fast decay component, the slow component is crucial for analysing the pulse shape. The physical basis that allows us to understand how discrimination is carried out is based on how the energy of the receding particles is deposited in the material. In order to determine the type of particle, the parameter dE/dx is entered. In the case of gamma rays, a low dE/dx is obtained since they interact mainly with the surrounding electrons, and the interaction causes the

electrons to recoil. The mechanism of elastic interaction between neutrons and nucleons within the nucleus produces the emission of protons with higher dE/dX than electrons. As a result, the electrical signal acquired by the types of particles can be distinguished by their tail, as can be seen in Fig. 3.7.

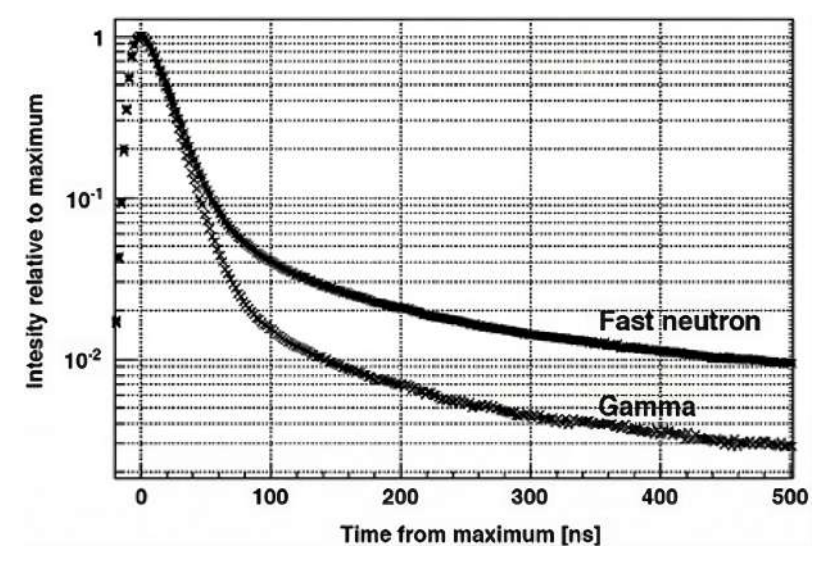


**Figure 3.7:** Average waveform from <sup>252</sup>Cf for neutrons and gammas in a hydrocarbon-based plastic, normalised to the same electron-equivalent energy range.

In NEDA, the electrical signal in the photomultiplier is digitised and processed by electronic systems (more in detail in section 3.1.3), and finally an offline analysis is performed. The main objective of the analysis is to achieve the best possible Neutron Gamma Discrimination (NGD). To do this, the NGD is based on analysing the pulse shape and the Time-Of-Flight information.

On the one hand, the PSA (Pulse Shape Analysis) based on the CC (Charge Comparison) method takes advantage of the difference in the shape of the pulses to discriminate between neutrons and gammas. It mainly consists of comparing two pulse regions and determining whether it is a neutron or a gamma. This method establishes that the ratio between the integral on the tail (named "slow component") and the integral covering the rising edge and part of the damp after the peak (called "fast integral") defines a parameter to discriminate between neutrons and gammas. When this parameter exceeds a certain threshold, the particle is considered a neutron, and if the parameter is less than the threshold, the particle is a gamma. As depicted in Fig. 3.8, after performing the CC, we can see a distribution of events. Using a threshold in the valley of the distribution makes it possible to distinguish between neutrons and gamma rays.

On the other hand, the Time-of-Flight (TOF) technique is a valuable method for determining the kinetic energy of travelling particles. The TOF

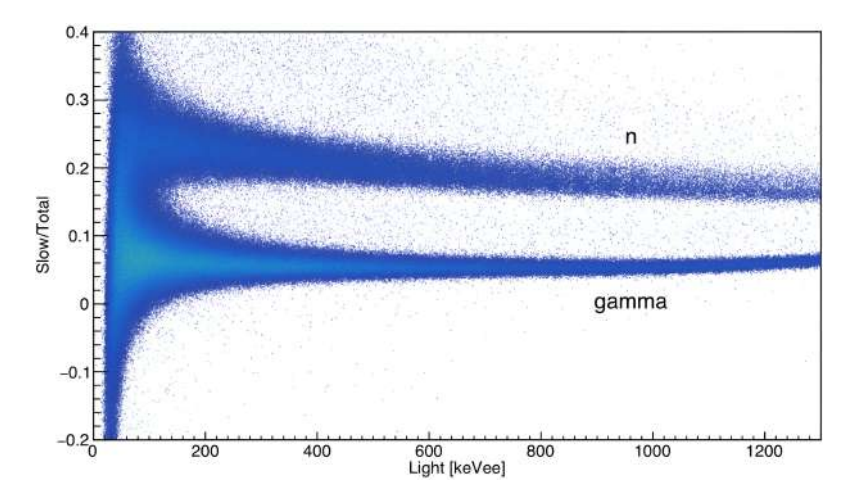


**Figure 3.8:** Pulse-shape discrimination based on the charge comparison method [38] measured with a NEDA detector using a <sup>252</sup>Cf source. The ratio of the light in the slow component of the digitised signal divided by the total light is shown on the y axis as a function of the total light in keVee on the x axis [8].

technique involves measuring the time it takes for a particle to travel between two fixed points with a known distance. In NEDA, the TOF is measured as the time difference between an external logical signal, e.g. the beam radio frequency signal (STOP), and the signal generated within the NEDA cell (START). As Fig. 3.9 shows, gamma-rays travel at a speed close to the speed of light, so their TOF is close to 0 ns. However, neutrons have a TOF between approximately 30 and 40 ns.

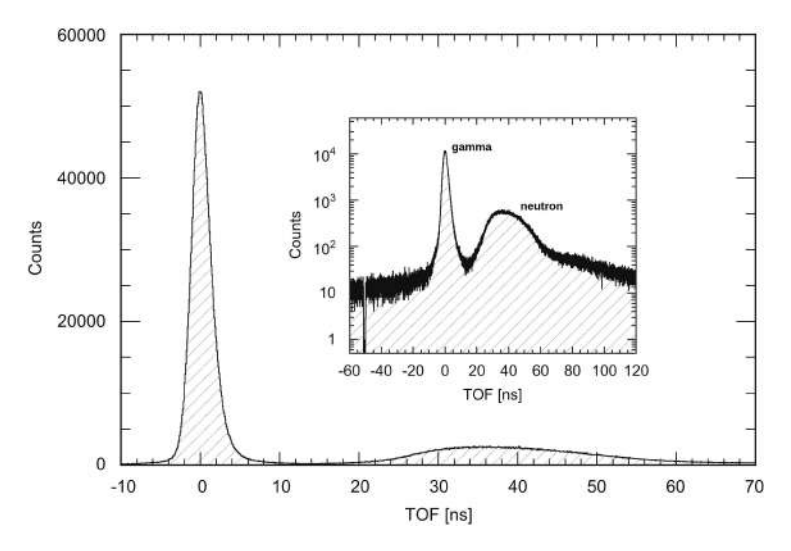


**Figure 3.9:** Measured Time-of-Flight distribution of pulses. The inset shows the TOF distribution in logarithmic scale [38].

#### 3.1.2 NEDA construction

The NEDA project has been split into three distinct stages, each serving a specific purpose. Initially, NEDA stage 0 aimed to modernise Neutron Wall electronics by transitioning from analogue NIM modules to state-of-the-art digital electronics utilising NUMEXO2.

The current NEDA Phase 1 is dedicated to integrating 90 detectors, forming a synergy with the existing Neutron Wall infrastructure. This combination consists of 45 detectors from the Neutron Wall and an additional 45 from NEDA, marking a significant expansion in detection capabilities. For NEDA phase 2, the deployment of the complete  $2\pi$  array, which comprises 355 detectors. This phase represents the culmination of efforts to maximise coverage and enhance detection efficiency.

In the future, a subsequent Phase 3 is envisioned to explore novel materials, advanced light readout systems, and the potential utilisation of highly segmented neutron arrays. Figure 3.10 presents a schematic outlining these phases, visually representing the project.

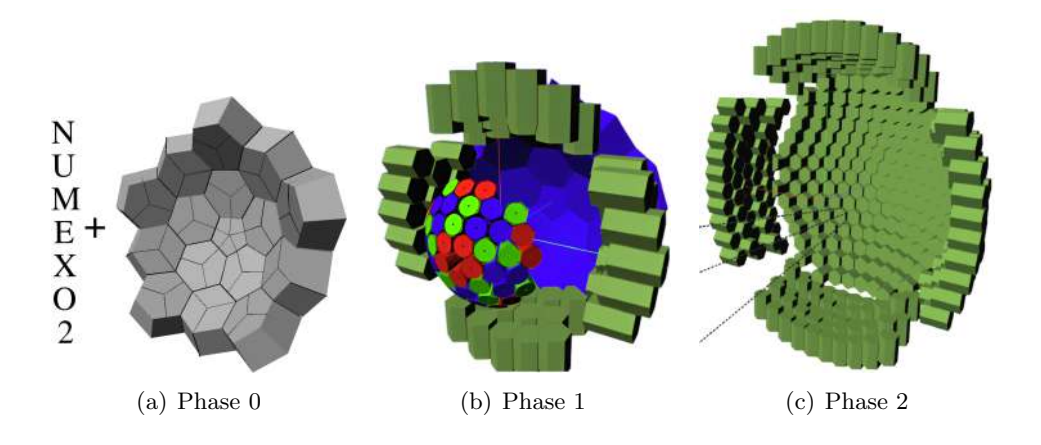


Figure 3.10: (a) NUMEXO2 digitiser + Neutron Wall. (b) Neutron Wall (blue) + NEDA (green) + AGATA (multi-color). (c) 355 NEDA detectors.

Currently, NEDA is in phase 1, working together with 45 NEDA cells, 45 Neutron Wall cells, AGATA and DIAMANT, as shown in Fig. 3.11.

#### Design of NEDA cells

Regarding the construction of each of the cells, the first studies focused on the geometry and materials of each cell, improving the performance of Neutron Wall. As it was previously described, several scintillators and PMTs were investigated and characterised with the main objective of improving neutron efficiency, timing and neutron-gamma discrimination (NGD). The final geom-

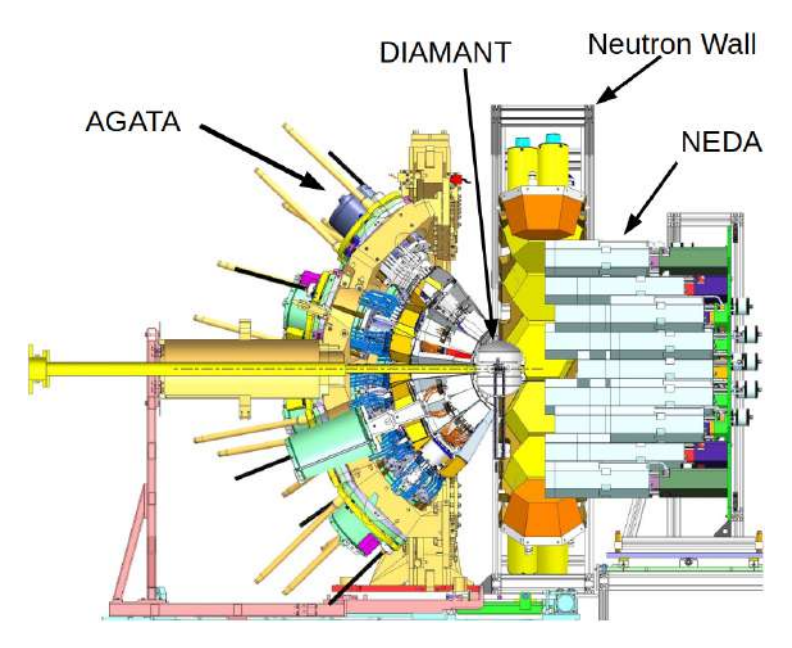


Figure 3.11: NEDA + AGATA + Neutron Wall + DIAMANT structure.

etry chosen is shown in Fig. 3.12. The optimal depth studied is 20 cm [39]. The side length of the hexagon is 84 mm, which is suitable for the largest photomultiplier tubes commonly available, with a diameter of 5 inches. The resulting volume of each detector cell is 3.23 litres. The external structure is made with an aluminium canning with a thickness of 3 mm, which is used to provide sufficient mechanical stability.

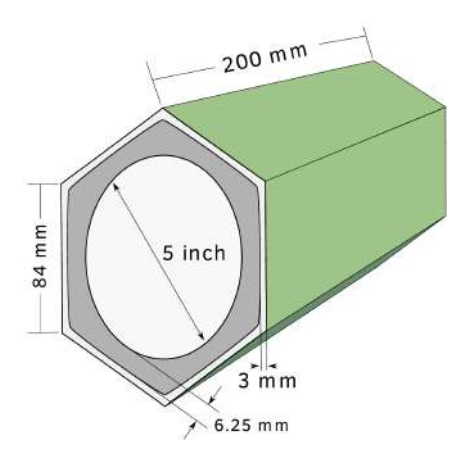


Figure 3.12: Schematic picture and measures of the NEDA detector cell.

Due to its high reactivity to air, a precautionary measure was taken during the assembly process. Before inserting the scintillator into each cell, the cell is filled with argon gas, mirroring the procedure used for empty units. Moreover, each cell is equipped with an expansion chamber designed to accommodate temperature-induced liquid expansion, thereby mitigating the risk of cell rupture. In order to optimise light transmission towards the PMT, the inner surface of the chamber containing BC501-A is covered with reflective paint. A cross-sectional view of a NEDA cell, with liquid scintillator BC501-A coupled to a PMT, is illustrated in Fig. 3.13.

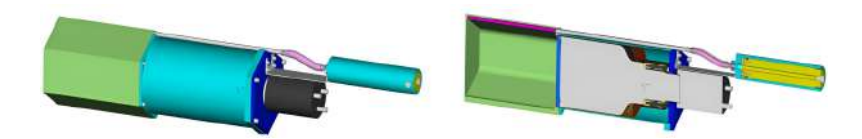


Figure 3.13: Scintillator coupled to a photomultiplier tube (PMT).

#### 3.1.3 NEDA electronics

The electronics for data acquisition have focused on equipping the Neutron Wall detector with new digital electronics, accommodating 45 detectors and also integrating the 45 NEDA detector modules. In addition, this electronics allows it to work together with AGATA and other detectors.

The electronic chain comprises several components [40]: single-ended to differential modules [41], the NUMEXO2 (Numériseur pour EXOGAM) motherboard, FADC Mezzanines [42], LINCO2 PCIe readout interface [43], GTS (Global Trigger and Synchronization) system [44], and workstations for data acquisition and processing. Figure 4.2 shows the scheme of NEDA electronics with single detector.

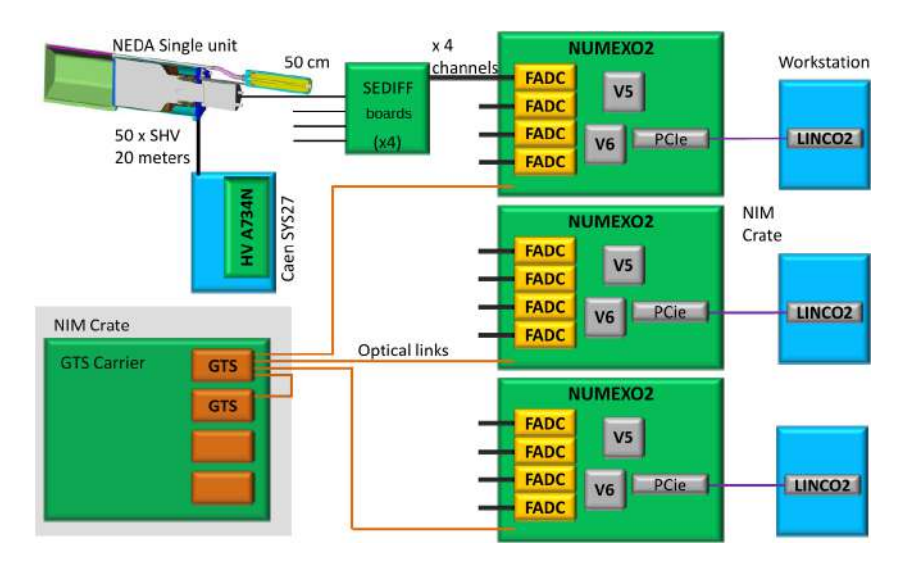


Figure 3.14: General scheme of NEDA electronics with single detector.

Each detector module, powered from the CAEN module SY527, is read by a single front-end electronics channel, extracting a current signal from the corresponding PMT. These signals pass through SEDIFF converter modules and are sent via a 10 m cable to the NUMEXO2 digitiser. Each SEDIFF module handles 16 channels. Upon reaching NUMEXO2, the digitiser incorporates 4 FADC Mezzanines with four channels each for A/D conversion at 200 Msps with 14-bit resolution. Digital pre-processing takes place in the NUMEXO2 motherboard, utilising Field Programmable Gate Arrays (FPGAs) (Virtex-6 and Virtex-5) to manage readout and digital pre-processing for 16 channels. A trigger algorithm, based on Charge Comparison, operates within the Virtex-6 to optimise bandwidth by reducing gamma-ray events. Trigger requests, primarily from neutrons, are then forwarded to the GTS for validation or rejection. The Virtex-5 includes a Power PC (PPC) embedded processor with embedded Linux OS for Slow Control (SPI/I2C) and communication management (TCP/IP, GTS leaf, PCIe protocol).

For readout capabilities based on event window and count rate, each NU-MEXO2 handles 400 MB/s (25MB/s), necessitating an optical link with a minimal data rate of 3.2 Gbps per digitiser with an estimated digitiser power consumption of  $\approx 100$  W.

# Chapter 4

# The NUMEXO2 digitiser

The NUMEXO2 digitiser, the heart of the NEDA front-end electronics, is a collaborative design with EXOGAM2 [4]. This collaboration aims to optimise both time and resources. This chapter details the main components of the digitiser: the FADC mezzanines, the Virtex-6 and Virtex-5 FPGAs. The design of the Virtex-6 has been deeply detailed as the firmware improvements carried out in this thesis have been implemented in this FPGA.

# 4.1 Description of the NUMEXO2

NUMEXO2, a crucial component in the EXOGAM2 and NEDA electronics, is responsible for digitising and pre-processing data for both detectors. Despite the different objectives of these detectors and methodologies in terms of radiation detection, NUMEXO2 functionalities remain useful. These include Analog-to-Digital (A/D) conversion, data pre-processing, interfacing with the GTS system, and managing communication links for 16 channels.

The NUMEXO2 digitiser, shown in Fig. 4.1, comprises a motherboard and a set of four FADC Mezzanines. The motherboard was developed by the *Group d'Acquisition pour la Physique* (GAP) at the *Grand Accélérateur National d'Ions Lourds* (GANIL) in Caen. The FADC Mezzanines developed at the University of Valencia perform the A/D conversion for four channels.

One of key features of the NUMEXO2 is its flexibility, which is attributed to its use of digital electronics with programmable logic devices. This characteristic allows for a common hardware basis, but with high-performance programmable devices that can implement various digital signal processing algorithms. Specifically, NUMEXO2 includes two, at that time, high-performance Field-Programmable Gate Arrays (FPGAs), a Virtex-6 and a Virtex-5 from Xilinx.

Designed to fit into the NIM standard crate, NUMEXO2 receives its power supply from the crate, which is then distributed to the rest of the electronics within the digitiser, including the FADC Mezzanines. The system's total



- (a) Frontal view of NUMEXO2.
- (b) NUMEXO2 hardware.

Figure 4.1: Frontal and general view of NUMEXO2.

power consumption is 100 W, which is equivalent to 6.25 W per channel (16 channels). The FADC Mezzanines consume 25 W of this total power. The block diagram of NUMEXO2, as illustrated in Fig. 4.2, includes the FPGAs, FADC Mezzanine, and communication links.

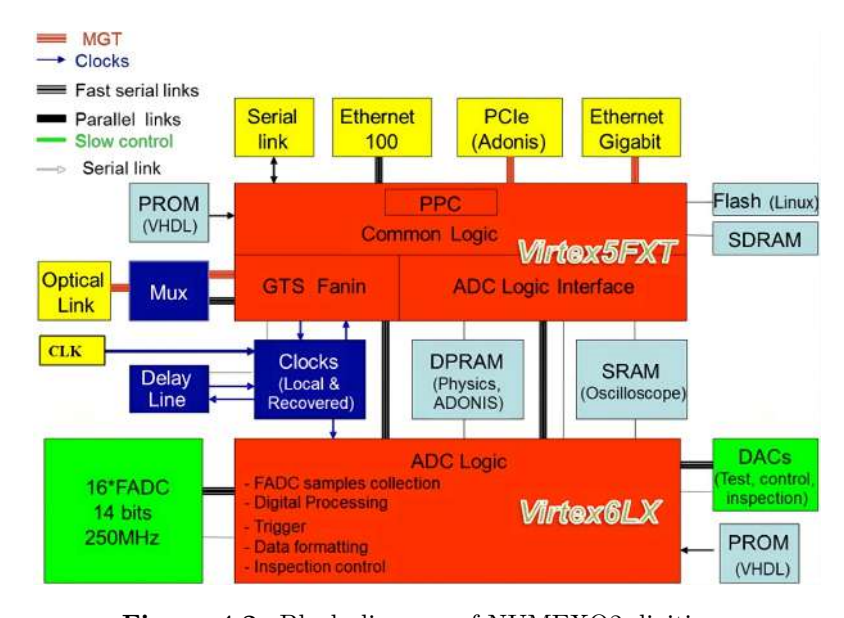
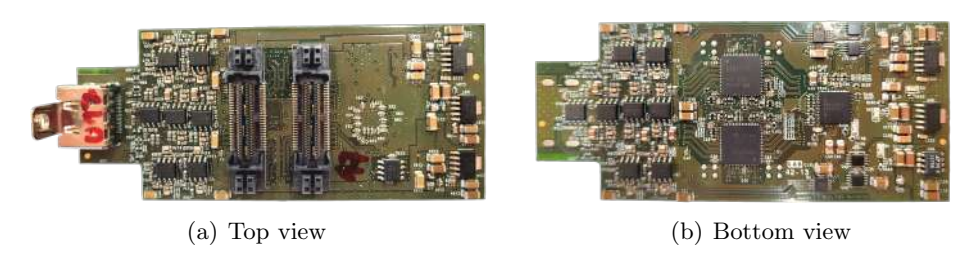


Figure 4.2: Block diagram of NUMEXO2 digitiser.

Next, the characteristics and functionalities of the three main components of the NUMEXO2: FADC Mezzanines, Virtex-6 and Virtex-5 are explained. In some of the block diagrams used in this chapter, only the most important blocks will be described.

# 4.2 The FADC Mezzanine

Four FADC Mezzanines manage the analog-to-digital conversion process [42,45]. These Mezzanines are equipped with a set of 14-bit dual ADS62P49 FADCs, which operate at a sampling frequency of 200 Msps. This frequency was chosen based on several factors, including the required bandwidth for the signal (considering its 10 ns rise-time), the ability to recover precise timing information during post-processing stages, and the need for compatibility with the GTS system, which requires the use of an integer multiple of the main clock frequency. Figure 4.3 shows the top and bottom view of a single FADC Mezzanine.



**Figure 4.3:** Top and bottom view of the hardware of the FADC Mezzanine.

The FADC Mezzanines are connected to the NUMEXO2 motherboard via board-to-board connectors. These connectors carry the input and output clocks from the FADC, differential parallel data lanes, control lines, and power supply. A 100 MHz clock input from NUMEXO2 is supplied into a PLL LMK03001C to generate low-jitter 200MHz clocks. The analogue interface to the input is facilitated using HDMI connectors and a series of analogue stages. These stages are based on the AD8139 fully-differential amplifier and provide input impedance matching, voltage matching at various gain settings (which can be configured by adjusting resistors in a T-bridge voltage divider), and first-order passive anti-aliasing filtering. The bandwidth of this filtering can be modified to suit different applications by changing a capacitor. Figure 4.4 shows the different parts of the single mezzanine.

# 4.3 Virtex-6 design

The Virtex-6 XC6LX130T device is installed in the NUMEXO2 board. Figure 4.5 shows the global scheme of the firmware implemented in this device.

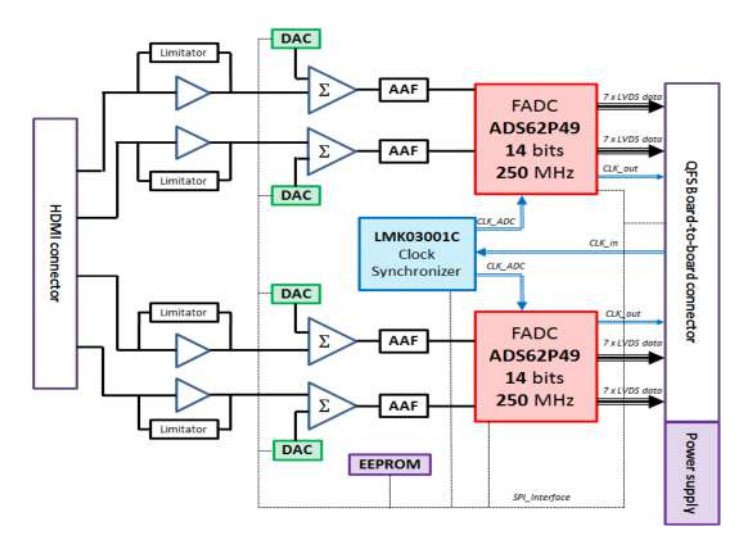


Figure 4.4: Block diagram of single mezzanine [42].

The global functionality consists of collecting the data from 16 channels of the FADCs mezzanines, providing a trigger request based on the decision whether the event acquired has neutron-like properties and organising the data from all channels to be transmitted to the Virtex-5 using a fast link. The new functionalities implemented in this thesis and described in chapters 5 and 6 have been added to this FPGA.

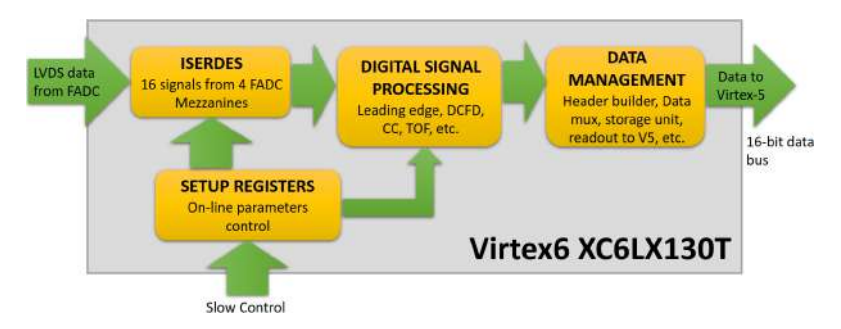


Figure 4.5: Block diagram of Virtex-6 firmware.

Therefore, based on the block diagram from above, the functionality of the main blocks is drafted in the following points:

- *ISERDES*. Input Serialisation/Deserialisation. The first block that data passes through when entering the FPGA. As explained in subsection 4.3.1, it takes the multiplexed odd-even bits pairs and delivers processable raw data samples.
- Digital Signal Processing. It performs basic signal processing with blocks such as leading edge, digital constant fraction discriminators, and trigger

request algorithms. The trigger request algorithm is intended to filter the trigger requests to the GTS coming from gamma-rays.

- Data management. Since the fast link between Virtex-6 and Virtex-5 allows only transmissions of a single event simultaneously, this IP buffers and organises the traces from 16 channels before sending data to Virtex-5.
- Setup registers. This allows the user to change the parameters of the Virtex-6 online. Thanks to a registered server in Virtex-5, this control interface can be performed.

#### 4.3.1 **ISERDES**

The Virtex-6 data acquisition chain starts with a setup involving ISERDES (serialisation/deserialisation data sub-blocks) to convert bit pairs into usable serial samples. The differential input signals to the Virtex-6 come from the FADC Mezzanines. Each FADC device contains 2 ADCs with two channels per ADC. A single IP ISERDES is implemented to manage the data from each ADC (2 channels). Figure 4.6 shows the diagram of the IP ISERDES and how the input and output data look.

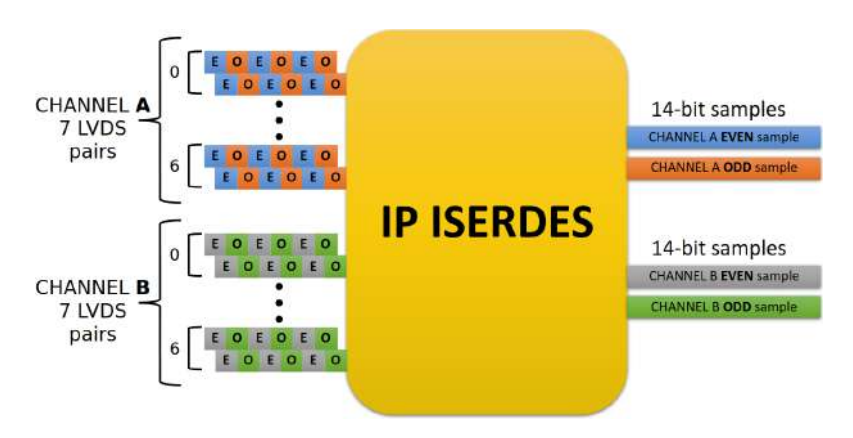
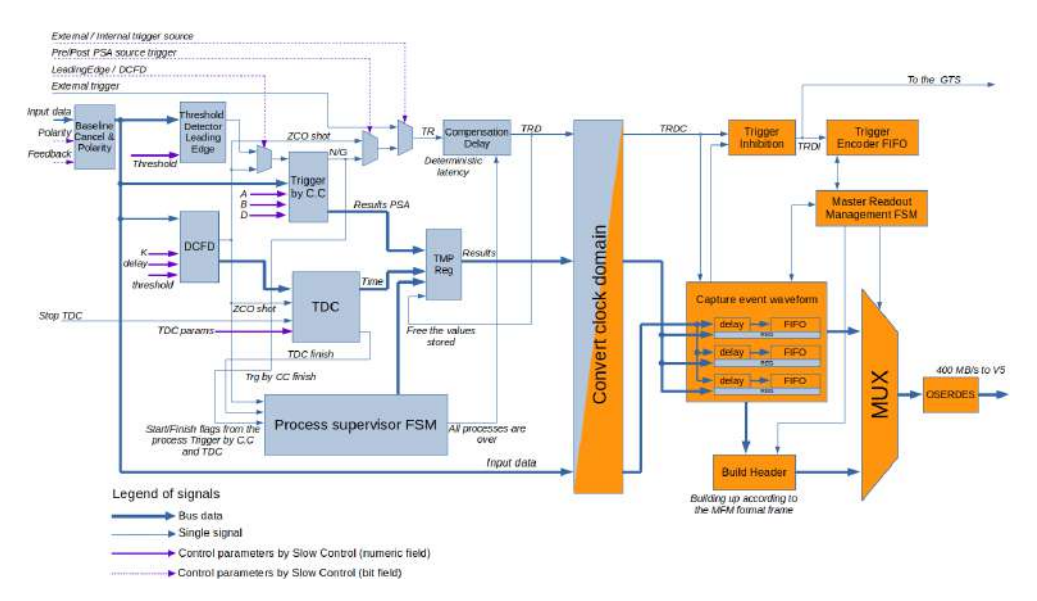


Figure 4.6: ISERDES hardware block diagram

Each FADC Mezzanine output is distributed in 7 LVDS differential pairs, in which each line contains multiplexed data from two consecutive bits, i.e. line 0 carries the bits 0 and 1, line 1 carries the bits 2 and 3, and so on, where the even bits are digitised during the rising-edge, and the odds on the falling edge. At the Xilinx IP ISERDES block output, the data is reordered in 14-bit samples. In total, 8 ISERDES IP blocks are implemented in the Virtex-6 to manage the 16 acquisition channels.

## 4.3.2 Digital Signal Processing

A dedicated architecture is designed in the Virtex-6 in order to satisfy the NEDA requirements regarding digital signal processing, packaging and readout. This architecture, depicted in Fig. 4.7, has two main domains depending on the clock. On the left side, in blue, the local processing uses the ADC clock in order to perform digital signal processing locally for two channels (even though only one has been shown), and, in orange, the readout interface that requires a global clock in order to command the merging of all channels during the packaging and readout (notice that final readout is performed inside the Virtex-5 by driving the data to the PCIe). Consequently, a clock domain conversion block is required before the data packaging, which is shown in both colours.



**Figure 4.7:** Digital signal processing for a single channel and interaction with the global readout. Blocks in blue refer to local processing, while orange refers to the readout system clocked by the global clock.

The main blocks within the digital signal processing are described below.

#### Baseline restorer

The baseline restorer block eliminates the offset that can entail difficulties in further processing stages. Given that the signals are fast, the offset component can be calculated simply by applying a low-pass filter with very low cut-off frequencies that would absorb the signal peaks. Then, the baseline restorer subtracts this offset component. The filter used is the Exponential Moving Average (EMA), which follows the following equation:

$$y(n) = y(n-1) + x(n) - \frac{1}{2^N} y(n-1)$$
(4.1)

Besides, a polarity control allows the signal to be changed sign controlled by Slow Control, making signal processing and acquisition more versatile.

#### DCFD (Digital Constant Fraction Discriminator)

Commonly, constant fraction discriminators are used together with ZCO (Zero cross-over) in high-energy and nuclear physics to provide a prompt trigger signal without introducing time-walk problems. In NEDA, the DCFD is also used to produce a starting signal to start the measure of the Time-of-Flight. The DCFD output produces a bipolar-shaped signal provided by the expression:

$$y(n) = k \cdot x(n) - x(n - \tau_{CFD}) \tag{4.2}$$

where k is the DCFD factor < 1, and the DCFD delay named as  $\tau_{CFD}$ , given in number of samples. From the hardware implementation point of view, the design contains the DCFD shaper that implements the equation mentioned above and a ZCO detector used to catch the zero crossing. The output signal produced from the ZCO detector is used as a START signal for the TDC block and as an input for the NGD block.

#### Trigger request based on Charge Comparison

As explained in Section 3.1, CC is one of the algorithms used for offline NGD, and this same algorithm has also been included in the NEDA firmware to generate an online trigger request when the CC result is higher than the threshold that determines whether the acquired event is accepted or not. Including this trigger request algorithm in the firmware reduces the counting rate since many gamma rays are discarded. This processing block has the START signal as input, selectable through Slow Control between START from Leading Edge or from the output of DCFD. In addition, it also has inputs controllable through Slow Control, the parameters A, B, and T. A is the number of samples of the fast component, B is the number of samples of the slow component, and T is the discrimination threshold parameter. As outputs, the results of the two integrals are calculated, and a logical trigger signal is obtained if the CC result is higher than the established threshold.

#### TDC

A Time-to-Digital Converter (TDC) is implemented to measure time intervals with larger resolution than the main 100 MHz clock cycle. In this case, it serves to obtain the time of flight of the particles. The TDC consists of a

clock generator, common for all channels, and a set of oversampling counters and FIFOs, implemented individually for each channel. The clock generator takes an input of 100 MHz and generates two derived clocks at 300 MHz with  $0^{\circ}$  and  $90^{\circ}$  phases, respectively. These two clocks trigger an oversampling unit that encodes the output value to be later counted. The 100 MHz clock is also used to manage a small FIFO that stores the time measurements.

#### Supervisor system

A set of controllers based on FSM supervises the whole process between the generation of the START signal (produced either by the leading edge or the CFD) to delivering the final trigger to the data management block. The motivation of such a design is due to the following factors:

- Some processes are not connected serially but in parallel. Therefore, the processing time required by each of them must be supervised, leading to a set of possibilities depending on which block is faster. The latency/processing time variability is due to the configuration of some blocks.
- A trigger request with a fixed latency is required. For the reason mentioned above, an extra delay (programmable but fixed for all channels) delivers the final trigger request after all processes end.
- Management of the parameters required to be inserted in the frame event. Since different parameters are calculated at different times but need to be delivered together, the FSM supervises the processes and is responsible for joining each calculated parameter to the corresponding event.

# 4.3.3 Data management

Since simultaneous events must be captured from different channels, an architecture to manage and coordinate the delivery to the Virtex-5 in the correct order of arrival is implemented. Figure 4.8 shows the block diagram of the designed architecture.

The system can be divided into two main parts: the first part gathers the 16 "Capture single channel" IPs and the data readout. This part would conform to the data path, and it is in charge of storing temporally and selecting the readout channel according to the arrival order of the events. A second part is responsible for sorting the trigger request signals, whose corresponding blocks are the trigger encoder and the readout FSM. The same order will be followed during the readout based on the arrival of trigger requests. For instance, if CH1, CH3, and CH6 are triggered in this order, then the readout controller FSM unit delivers the waveform in the proper order: CH1, CH3, and CH6.

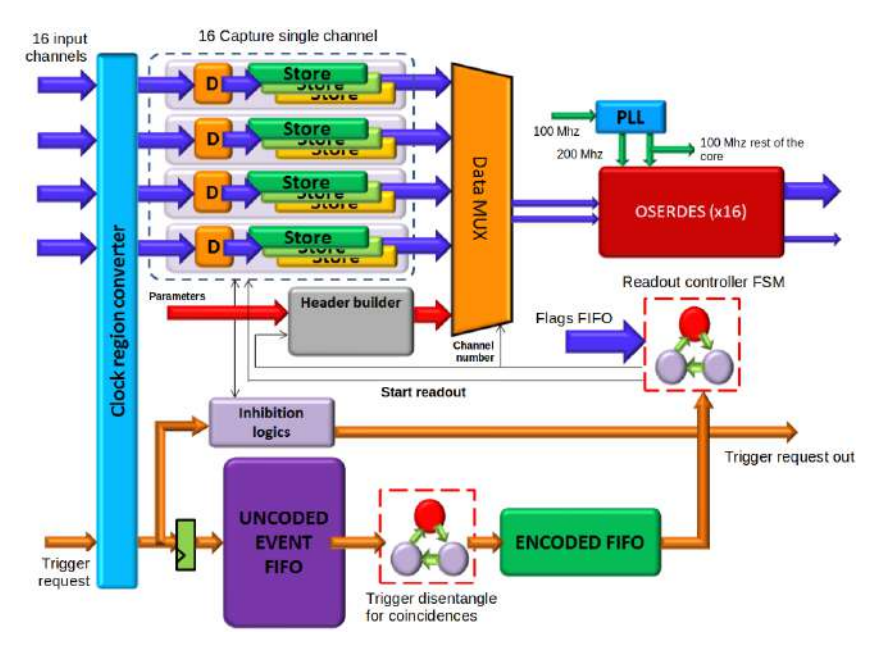


**Figure 4.8:** General block diagram of the capture event to transmit data between Virtex-6 and Virtex-5

#### Capture single channel IP

Each "Capture single channel block" carries out the waveform storage for a single channel, meaning that 16 identical blocks must be instantiated. Each unit manages the writing operations when a new event produces a trigger. Fig. 4.9 shows the block diagram of the capture single channel IP.

In addition to the fact that different acquisition channels can be active simultaneously, consecutive events close in time can be acquired by the same channel. This can result in a new event being acquired while an event is being processed, which must also be processed. In order to handle these scenarios, each capture single channel unit features three storage elements, implemented as FIFO memories. This way, the goal of implementing the storage unit is to capture new events even in case one of the FIFOs is being written when a new event comes, even if other FIFOs are full or being read. If all FIFOs are full, the system will only accept new traces once the memories are flushed out.

# 4.3.4 Setup Registers

Most of the parameters introduced during the digital signal processing part and data readout can be changed externally by the user, requiring a control interface and a set of registers to store them.

In NUMEXO2, the global Slow Control is carried from the control PC and mapped mainly in the Virtex-5 register server. This register server contains the

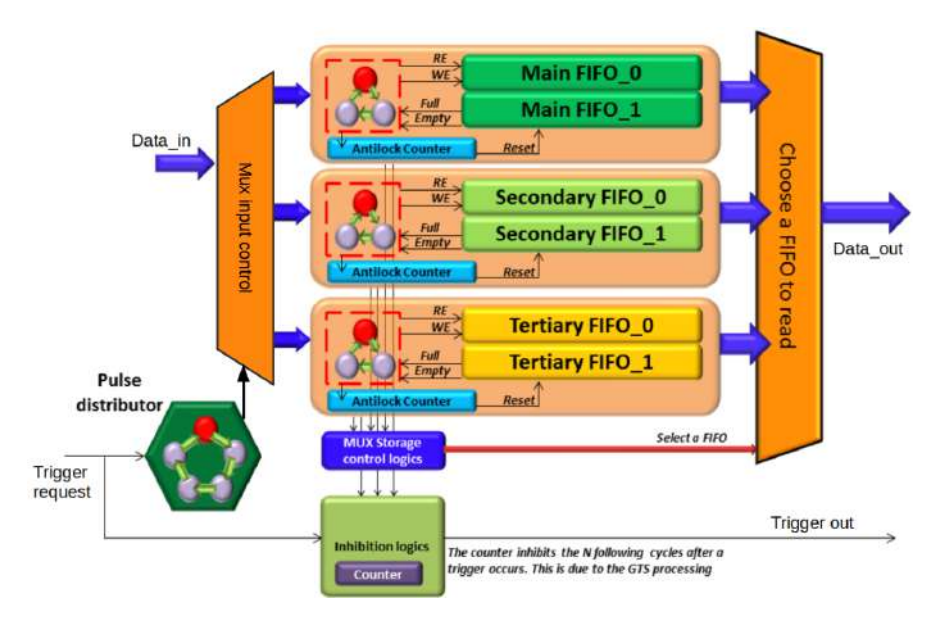


**Figure 4.9:** General block diagram of the capture event to transmit data between Virtex-6 and Virtex-5

parameters for the whole NUMEXO2, including Virtex-6, FADC Mezzanines, Virtex-5 self-parameters, and the GTS leaf (inside Virtex-5), as well as some external NUMEXO2 devices such as memories and the PLLs.

Regarding the Virtex-6, the register bank mapping is carried out using a Slow Control SPI protocol between Virtex-6 and Virtex-5, where Virtex-5 (for this case, the master device) bypasses the commands to the Virtex-6 using SPI commands. Then, at the slave device, the Virtex-6 decodes the SPI commands and sets all required parameters for global control and monitoring.

# 4.4 Virtex-5 design

The other programmable component integrated into NUMEXO2 is the Virtex-5 FX70T device, which manages data reception from the Virtex-6 processing. In contrast to the Virtex-6, the Virtex-5 design adopts a microprocessor-centered approach, where various cores or peripherals are organised within a bus structure. However, this arrangement does not mandate that all cores respond directly to microprocessor commands. Specific modules, like the PCIe controller or ADC interface, autonomously handle data transfer without requiring microprocessor intervention. Entities like the TCP/IP core, GTS leaf, and SPI controllers rely on software instructions delivered through the PLB central bus. Figure 4.10 shows the block diagram of the Virtex-5 design.

The following paragraphs describe the fundamental blocks in the Virtex-5 relevant to NEDA.

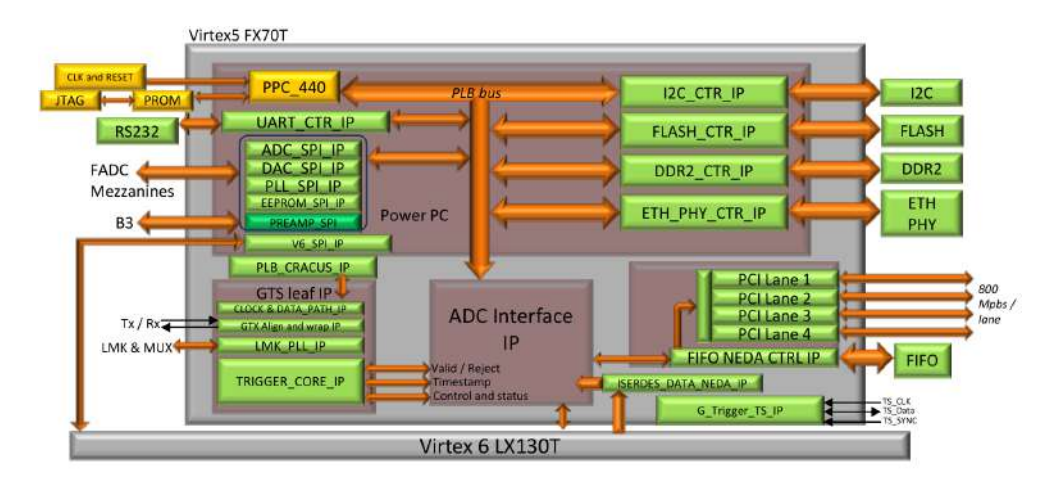


Figure 4.10: Virtex-5 block diagram. Courtesy of GANIL

#### ADC Interface IP

The ADC interface block within NUMEXO2 serves as the receiver for data from the Virtex-6. Its functions include collecting and unpacking data frames from the Virtex-6, storing them in a buffer, and awaiting validation or rejection of event data by the GTS leaf. Upon validation by the GTS, the leaf appends the received timestamp. Subsequently, the ADC interface forwards the timestamped to the output PCIe.

#### PowerPC (PPC) and its peripherals

The Virtex-5 features a built-in hardware PowerPC (PPC) processor running an embedded Linux operating system, which efficiently handles the intricacies of the TCP/IP protocol. This processor performs various tasks, including configuring other components within the Virtex-5. These tasks enclose managing Ethernet Gigabit settings, configuring PCIe setup registers, setting up the GTS leaf, coordinating with the Virtex-6 setup, handling FADC Mezzanine SPI registers, B3 registers, external Flash (256 Mb), DDR (1 Gb) memories, and a serial port for monitoring Linux OS boot status.

#### GTS leaf IP

Derived from AGATA, the GTS (General Trigger System) synchronises digital multichannel systems and validates or rejects events. The GTS system is organised in a hierarchical tree structure, with the GTS leaf situated at the lowest level. It is responsible for receiving and packaging trigger requests from the Virtex-6 to the GTS system, including the tree and trigger processor outside NUMEXO2. Each NUMEXO2 unit incorporates a single GTS leaf IP,

which is optically connected to a GTS crate, capable of overseeing up to 16 channels.

## PCI express IP

Within NUMEXO2, an optical link is integrated, housing 4 PCIe Endpoint lanes capable of achieving up to 3.2 Gbps (800 Mbps each). This configuration aligns with NEDA specifications regarding data requirements. Within the PCIe driver lies a FIFO, serving to buffer data between the ADC interface and the driver, ensuring smooth data flow and efficient processing.

# Chapter 5

# Lossless data compression for data acquisition

This chapter focuses on the study and development of a lossless compression method to reduce the necessary storage size and have the ability to increase the counting rate in experiments. The study will focus on lossless compression methods, as no loss of event information is desired. Regarding the development, once the method is chosen, it will be implemented in Python using data from experiments and testing the method's validity for NEDA data. Subsequently, it will be implemented and tested in NUMEXO2.

## 5.1 Introduction

In recent years, data storage capacity and processing speed in electronics and communication networks have increased. Moving to higher speeds is a complicated task, particularly when the hardware cannot be modified, as with NEDA's electronics. In this environment, to achieve higher speed performance, one must resort to techniques that allow to overcome the physical deficiencies of the hardware. The most important technique in this regard is data compression. Data compression is beneficial because the compressiontransmission process is faster than the transmission process without compression. Data compression is not only for data transmission but also for mass storage. The need for storage is also rising beyond the possibility of increasing the hard drives or memory expansion capacities. The motivation for applying compression to data, is to reduce costs both in storage (less space is required) and in data transmission (data are transmitted faster using the same bandwidth). The price to be paid is some computational time to compress and decompress the data [46]. Several methods and algorithms attempt to reduce or eliminate redundant data to achieve data compression. They are classified into two groups: lossy and lossless [47].

- Lossy data compression methods discard some data to achieve a smaller size. These methods can reduce the data quality, although it is still possible to recreate the original data from the compressed data. An example of lossy compression is JPEG image compression [48], which discards some image information to achieve a smaller file size.
- Lossless data compression methods preserve all the data and recreate the original data exactly from the compressed data. These methods are often used for data transmission, where it is crucial to preserve the integrity of the data. An example of lossless compression is Huffman coding [49], which uses a codebook to replace common data patterns with shorter codes.

In data transmission, lossless data compression methods are preferred to ensure that the data transmitted is the same as the original data. This fact is essential for applications where accuracy is critical, such as medical imaging, scientific data, and financial transactions. By using lossless data compression methods, data transmission can be faster and more efficient without sacrificing the integrity of the data. In the case of NEDA experiments, it is essential to maintain event information to analyse the waveform properly. Therefore, in Section 5.2, different lossless data compression methods have been studied and applied to choose the most suitable one and implement it in the existing NUMEXO2 firmware. For the choice of method, some design aspects taken into account are described below.

# 5.1.1 Implementation considerations for data compression in NUMEXO2

First, the reading capabilities of NUMEXO2 in NEDA experiments must be analysed. When performing experiments with high-intensity ion beams, the counting rate has been set to 50 kHz, and the number of channels NUMEXO2 works with is 16 [40]. On the other hand, the trace of each event has a size of 256 samples, and each sample is 2 bytes, so the total size of each trace is 512 bytes. With this information, the maximum acquisition bandwidth (BW) can be determined with the following expression:

$$BW = Bytes \ per \ Trace \times Counting \ rate \times N_{ch}$$
  
$$BW = 516 \ Bytes \times 50 \ kHz \times 16 \ Channels = 409.6MB/s$$
 (5.1)

Therefore, if the number of bits required for the trace of each event can be reduced, the counting rate could be increased without exceeding the maximum rate of 409.6MB/s.

Another aspect to consider is where the compression method is implemented, either in the Virtex-6 or in the Virtex-5. Since Virtex-6 is first in the

acquisition chain, it has been decided to implement the compression block in this device. In this way, the transmission of an event between Virtex-6 and Virtex-5 will be faster as fewer bits will be transmitted for each event. Thus, it is necessary to know the resources available in Virtex-6 to implement new functionalities. The following figure shows the resources already used for the rest of the firmware:

Device Utilization Summary (estimated values)			
Logic Utilization	Used	Available	Utilization
Number of Slice Registers	48882	160000	30%
Number of Slice WTs	53224	80000	66%
Number of fully used LUT-FF pairs	25242	76864	32%
Number of bonded IOBs	56	600	9%
Number of Block RAM/FIFO	85	264	32%
Number of BUFG/BUFGCTRLs	25	32	78%

Figure 5.1: Resources used in the FPGA without compression method included.

As can be seen, some of the resources are used more than 60% (LUT is 66% and BUFG is 78%). Therefore, the compression method should be designed to consume minimal resources. This will enable the implementation of the current design and accommodate potential future modifications.

It is also important to consider the actual data structure. In the case of NEDA acquisition, the Header cannot be modified, so the compression will focus on only reducing the size in bytes of the trace of each event. Therefore, the data compression method shall compress the event trace but keep the size of the Header of each event, as shown in the following figure:



**Figure 5.2:** Example one event compressed where X is smaller than 128.

Finally, the compression ratio and space-saving, defined in Eqs. (5.2) and (5.3), will also be considered when choosing the appropriate compression method.

$$Compression \ Ratio = \frac{Uncompressed \ Size}{Compressed \ Size} \tag{5.2}$$

$$Space \ Saving = 1 - \frac{Compressed \ Size}{Uncompressed \ Size}$$
 (5.3)

Different compression methods are then studied to find the most suitable one to compress each event trace, looking for the best compromise between compression capacity and low resource consumption.

# 5.2 Lossless compression methods

Throughout history, many lossless compression methods have already been developed for engineering, computer science and physics [50]. Given the limitations of NEDA electronics, some of the most commonly used simple methods have been analysed and applied ad-hoc for NEDA in order to assess their suitability.

#### • Run-Length Encoding (RLE)

RLE is a simple lossless data compression algorithm that replaces repeated data sequences with a single value and a count of the number of times it occurs. It was developed to transmit analogue television signals in 1967 [51], and 1983, run-length encoding was patented by Hitachi [52]. RLE is particularly effective for compressing data that contains long runs of repeated values, such as simple images or audio files with silence. As shown in Fig. 5.3, in RLE, the input is split into runs of identical values, and each run is replaced with a code that consists of the value and the length of the run. The resulting compressed data can be stored using fewer bits than the original, resulting in a smaller file size. The advantage of this method is that it is easy to implement and is often used in real-time data transmission and low-bandwidth storage applications.

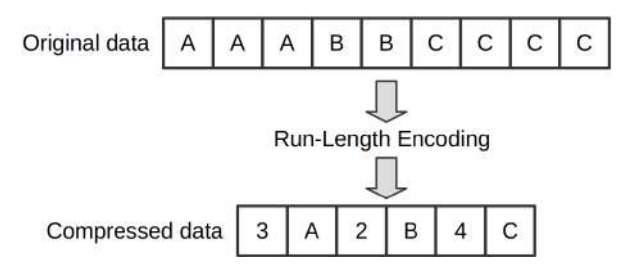


Figure 5.3: Example Run-Length Encoding.

This method has been implemented on 1,000 traces acquired with NEDA obtaining, on average, a compression ratio of 1.09, saving 8.3% space. This low compression ratio is because, in the baseline, few values are repeated contiguously.

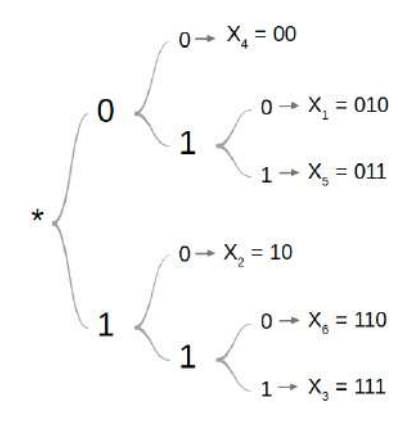
# • Huffman coding

Huffman coding is a method proposed in 1952 by David Huffman [49]. The idea behind Huffman coding is to assign the shortest possible binary codes to those symbols that occur most frequently in the data. By contrast, infrequently occurring symbols will be assigned binary codes of greater length. Huffman's coding method provides the optimised assignment rule, which is uniquely decodable. The following example illustrates this method.

#### - Example:

Consider a dataset consisting of 6 numbers  $X_i$  where  $1 \le i \le 6$ , with probability of occurrence of 0.1, 0.3, 0.2, 0.2, 0.1, 0.1, respectively.

Subsequently, applying the Huffman coding method [53], the tree in the figure 5.4, and table 5.1 with assigned codes is obtained.



Number	Probability	Code
$\overline{X_1}$	0.1	010
$\overline{X_2}$	0.3	10
$\overline{X_3}$	0.2	111
$\overline{X_4}$	0.2	00
$\overline{X_5}$	0.1	011
$\overline{X_6}$	0.1	110

Figure 5.4: Example Huffman tree.

**Table 5.1:** Example of Huffman code assignment

If a fixed size is taken for all numbers, at least 3 bits are needed for each one. In contrast, with the Huffman method, the average size of this code is  $0.1\times3 + 0.3\times2 + 0.2\times3 + 0.2\times2 + 0.1\times3 + 0.1\times3 = 2.5$  bits for each number. Once the code is obtained, it is possible to encode and decode. For example, the following string of encoded numbers 10111011 is decoded as  $X_2X_3X_5$ , obtaining, in this case, a compression ratio of 1.286 and saving 22.22% of space.

The same process was applied to a trace obtained with one of the NEDA detectors. Figure 5.5 shows the Huffman tree obtained and Table 5.2 shows the Huffman assignment.

Without compression, 3712 bits are used for each trace (232 samples \* 16 bits/sample). In the case of the coded event, the trace would need 3296 bits. This results in a compression ratio of 1.13 and a space-saving of 11.21%.

In order to apply this method to NEDA data, it would be necessary to generate a Huffman tree for each event and transmit its assignment. This information must also be sent for each event so the size of the event will increase and the compression ratio will be reduced. In addition, this new information must be included in the event header, but the size of the header cannot be increased, as mentioned above.

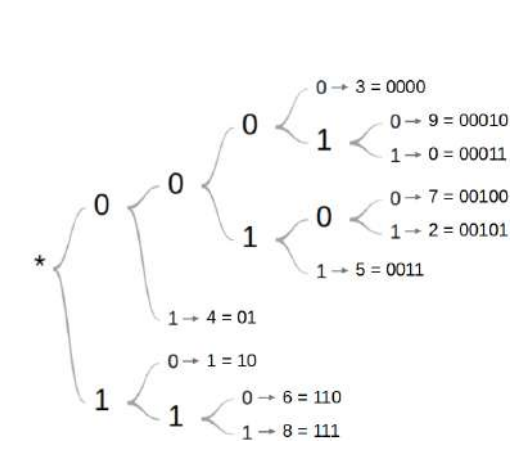


**Figure 5.5:** Example Huffman tree for NEDA event.

Number	Code
0	00011
1	10
2	00101
3	0000
4	01
5	0011
6	110
7	00100
8	111
9	00010

**Table 5.2:** Example of Huffman code assignment for NEDA event

#### • Dictionary methods

Dictionary-based methods use the principle of replacing data strings with codewords that identify that string within a dictionary. Three dictionary-based methods can be differentiated into dynamic (Sliding Window Algorithms) and static. All of them are based on the algorithm developed and published by Abraham Lempel and Jacob Ziv [54] and are widely used in different file compression formats, such as ZIP and RAR.

The main dynamic algorithm is the LZ77 [54] which introduced the concept of 'sliding window', which is based on finding if the character sequence currently being compressed has already occurred earlier in the input data. If the same sequence is found, instead of repeating it, it is replaced by a pointer.

Static dictionary methods create a dictionary from the first reading of the data. In compression, when they encounter a phrase already present in the dictionary, they output the index number of the phrase in the dictionary. The most commonly used static methods are LZ78 [55] and LZW [56].

Compression of the same NEDA event used above has been done with the LZW algorithm to check the compression ratio obtained and the saved space. The compression ratio obtained is 1.25, and the space saved is 20.15%. Although the space saved increases comparing to the Huffman method, sending extra information for each event is still necessary. This

method is, therefore, also ruled out for implementation in NEDA data acquisition.

#### • Differential encoding

Differential encoding or relative encoding [57] is a compression technique that works by encoding the difference between successive data points instead of encoding the absolute values of each data point. This technique is handy for compressing data with a high correlation between adjacent samples.

The basic idea of differential encoding is subtracting the previous sample from the current sample to obtain the difference between them. In order to decode the differentially coded data, the original sample is reconstructed by adding the encoded difference to the previous sample. This process can be repeated for each sample in the sequence, reproducing the original data. Based on this concept C.Chapin Cutler in 1952 [58], developed the DPCM (Differential Pulse-Code Modulation), which has been used for voice, image and audio transmission.

One of the advantages of differential encoding is that it can be implemented very efficiently using simple arithmetic operations. This advantage makes it particularly well-suited for real-time applications, where low latency and low computational overhead are essential considerations.

Based on this method, two different compression methods (Differential coding with variable number of bits and Differential coding with fixed number of bits), implemented ad-hoc for NEDA data, based on differential encoding were proposed.

#### - Differential coding with variable number of bits

In the protocol established in the NEDA acquisition chain, once the signal has been digitised, each sample of the acquired signal is transmitted in 16 bits. The Differential coding with variable number of bits method proposes keeping the value and size at the first sample and recording the differences between successive samples with the minimum number of bits possible. In addition, since the differences can be negative or positive, an extra bit is added. Figure 5.6 shows how this method works and Fig. 5.7 how it is applied to the same event used with the previous methods.

Applying this method, the compression ratio of 3.93 and the space-saving of 74.57% have been obtained. However, sending the number of bits necessary for each sample would also be necessary to decompress this event. If this method were implemented, the number of bits required for each sample could be sent after each. Adding this information, the compression ratio is reduced to 1.32, achieving a space-saving of 24.6%

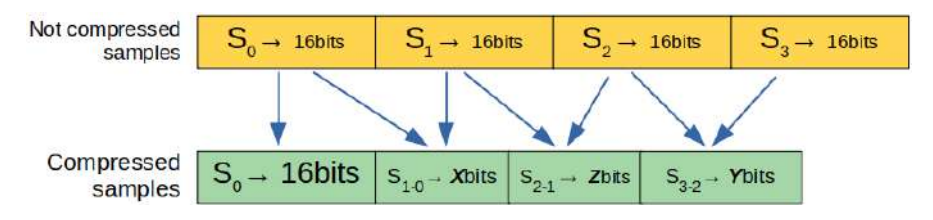


**Figure 5.6:** Schema Differential coding with variable number of bits where X, Z, and Y are less than or equal to 16.

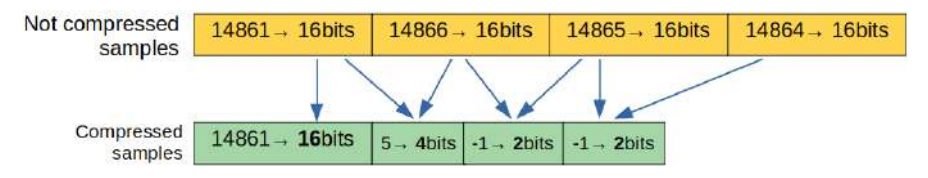


**Figure 5.7:** Example of Differential coding with variable number of bits in the first samples in a real trace.

#### Differential coding with fixed number of bits

This is an ad-hoc method for NEDA based on the above method. This new method, instead of storing each sample in as few bits as possible, a study of the signals is conducted to assess whether assigning a fixed number of bits to store the samples in differences is possible. In this way, it would not be necessary to send with the sample the number of bits needed to store it, as is the case using the Differential coding with variable number of bits.

In order to evaluate this method, the same event has been taken as in the previous methods. Figure 5.8 shows the signal's shape, where it is possible to choose to use 8 bits in the flattest areas of the trace and 16 bits in the peak and tail, except for the first sample, which is kept uncompressed for reference.

Considering the samples chosen to compress to 8 bits (1-40 and 100-232) and the samples to compress to 16 bits (41-99), we obtain a ratio of 1.6 and a space-saving of 37.5%. Of course, these results will depend on the samples selected. This method achieves a better compression ratio than the Differential coding with variable number of bits because it has the advantage that it is unnecessary to send information on the size of each sample as it is chosen beforehand. On the other hand, as mentioned above, it is necessary to make a previous study of the signals to choose the number of bits in each section of the signals.

The Differential coding with fixed number of bits does not require sending extra information and achieves higher compression ratio than the Differential



Figure 5.8: Example of Differential coding with fixed number of bits.

coding with variable number of bits and the RLE method. So, this method has been chosen to study its viability using Python and, if feasible, to implement it in the NEDA firmware.

# 5.3 Python implementation

In addition to the Differential coding with fixed number of bits method, a variant of this one has been proposed for implementation in Python. As previously mentioned, in the Differential coding with fixed number of bits method the difference between successive samples is calculated. This newly proposed method consists of taking the first sample as a reference and calculating the difference between the reference sample and the rest. This variant will require a lower computational load since it does not require updating the reference sample in each cycle.

In order to check the feasibility of both variants of the method for NEDA signals, it is necessary to study the number of bits needed to store the samples in the different sections of the signals: initial baseline, pulse (peak and tail), and final baseline. The baseline sections are where it will be possible to get the most compression, so the noise contribution in the baseline is crucial. To know the baseline noise of the signals, the noise level has been calculated with signals acquired by NEDA. Figure 5.9 shows the baseline noise acquired in 10,000 signals with NEDA at HIL (Heavy Ion Laboratory). Taking the highest and lowest value and taking into account the configuration and characteristics of the FADC (resolution of 14 bits, at 2 Vpp [59]), the maximum noise level is 6.5 mVpp.

The two variants of the method have been subjected to 10,000 signals generated with the Desktop Digital Detector Emulator DT5800D [60], with

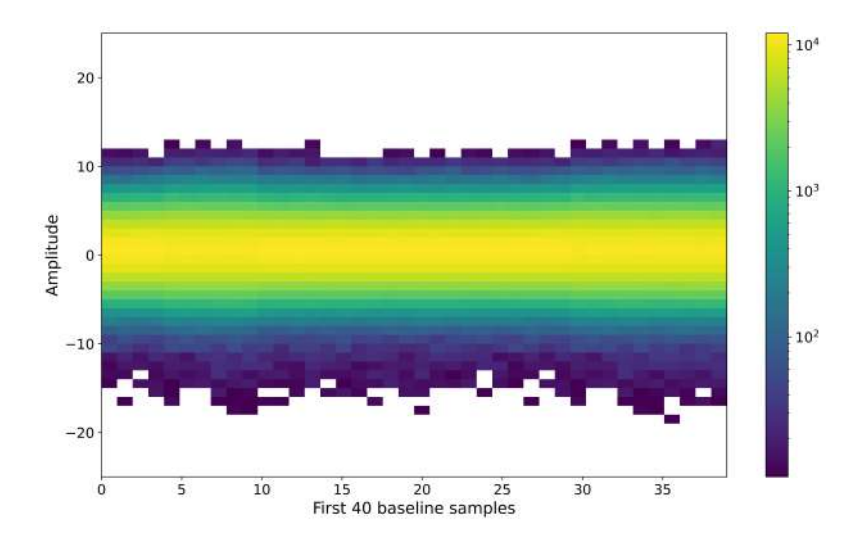
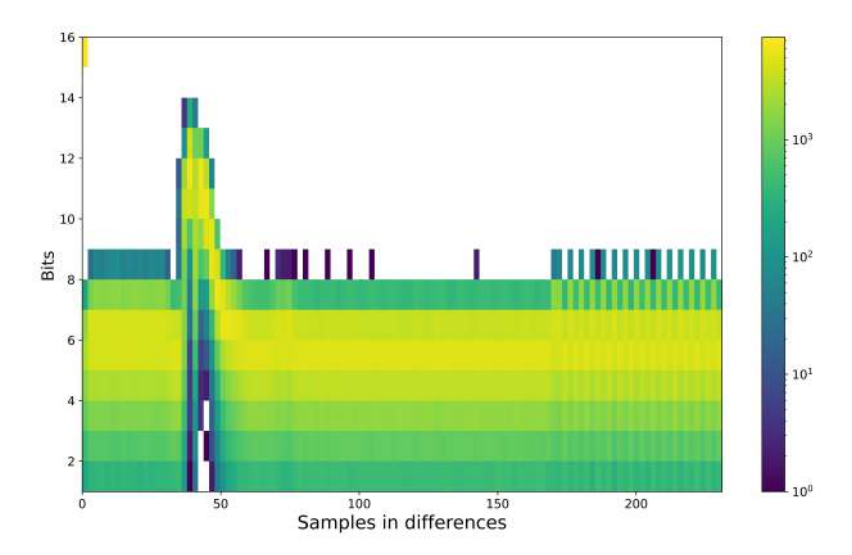


Figure 5.9: Baseline noise of 6.5 mVpp in a data acquisition at HIL.

10 mVpp of noise at the baseline. These signals were then compressed, and the minimum number of bits required for each compressed sample was determined, including the sign bit. The following figures show, for each variant, the number of bits required in each sample and the frequency with which each value is repeated.



**Figure 5.10:** Number of bits required for the difference between consecutive samples.

As it can be seen, in Fig. 5.10 and 5.11, the number of bits needed in both variants initial and final baseline is 8 bits. Although in the case we take the difference between samples, in some moments, will only need 7 bits, the size

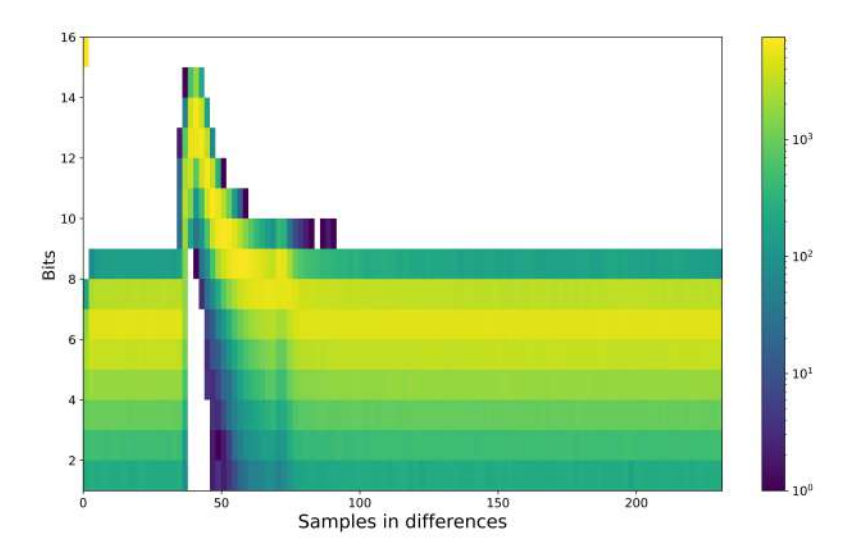


Figure 5.11: Number of bits required for the difference with the first sample.

will be 8 bits since it is the maximum necessary for that section of the signal. In the pulse section, the number of bits required is a maximum of 14 bits for the case "difference with the reference" and 13 for the case "difference between consecutive samples". Instead, since the data must be packed in 16-bit blocks, even if the maximum is less than 16 bits, it must be stored in 16 bits. Since 16 bits is the number of bits uncompressed samples have, this part of the signal will be left uncompressed to ensure signal integrity in the pulse.

Once we had analysed the number of bits needed and which variants to use in the compression method, a script was developed to perform the compression with the chosen method.

The compression software developed in Python was emulated the data processing in Virtex-6. The basic schematic of the compression software is shown in Figure 5.12. The Virtex-6 receives digitised signals, where each sample comprises 16 bits. Subsequently, the difference between all baseline samples and the reference was calculated. Then they were packed into 16-bit blocks to comply with the communication protocol.

Since in different experiments, the start of the pulse as well as the size of the pulses can change, two parameters were added: the sample up to which we use the compression method before the start of the pulse and the sample from which apply the compression after the end of the pulse to the end of the signal. These parameters can be controlled in the FPGA through Slow Control.

The compression method has been tested using the same set of signals. With the same compression parameters (30 and 120), a compression ratio 1.44 is obtained (30% saved). Higher compression ratios can be achieved by using higher values for the first parameter and smaller values for the second.

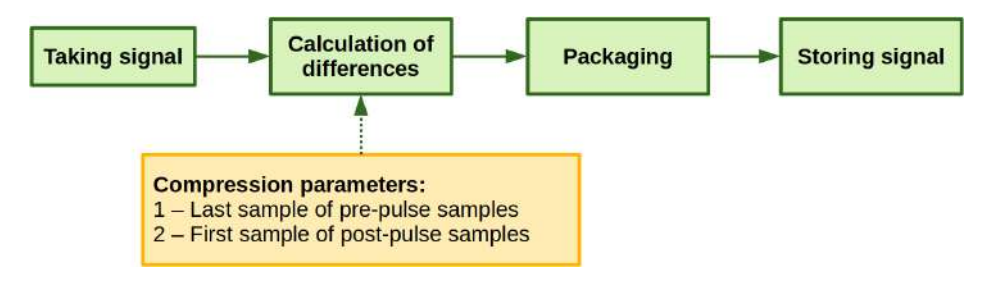


Figure 5.12: Outline of the basic concept of data compression.

For example, 32 and 100 could be used for this set of signals, obtaining a compression ratio 1.54 and saving 35%. After storing the compressed events, they have been successfully decompressed without loss.

These results confirm that the Fixed sample size differential coding method using the first sample as a reference is viable for compressing NEDA signals; thus, the next step is implementing this method in NUMEXO2.

# 5.4 Firmware implementation

Implementing the data compression in the firmware requires choosing the optimal location to develop the compression method on the NUMEXO2. As previously mentioned, the compression firmware has been developed for the Virtex-6 FPGA, as it is the first FPGA where the data arrives. Thus, the transmission of compressed signals from Virtex-6 to Virtex-5 will be faster than that of uncompressed signals. Within the Virtex-6, it has been necessary to analyse the existing firmware Fig. 4.7 to place this block so that it affects the existing firmware as little as possible. As seen in section 4.3.3, an individual "Capture Single Channel" block per channel has been dedicated within the readout architecture since simultaneous events must be caught. Taking advantage of this architecture, the compression block has been added within this block.

The Capture Single Channel block coordinates the arrival of consecutive events with the Control Multiplexer. This multiplexer manages the events so that if a new event arrives while a previous event is being processed, i.e. the FIFO\_A is not empty, it will be written to the FIFO\_B. If FIFOs A and B are busy, the new event is stored in FIFO\_C.

In the new firmware, as depicted in Fig. 5.13, a modification has been made where compression blocks are introduced following each FIFO. Under the new configuration, if a new event arrives while the previous event is still undergoing processing (including compression), the incoming event will be processed in the subsequent acquisition block. If the first two acquisition blocks are already occupied, the third one will be utilised. This revised architecture allows compressing up to three consecutive events when needed.

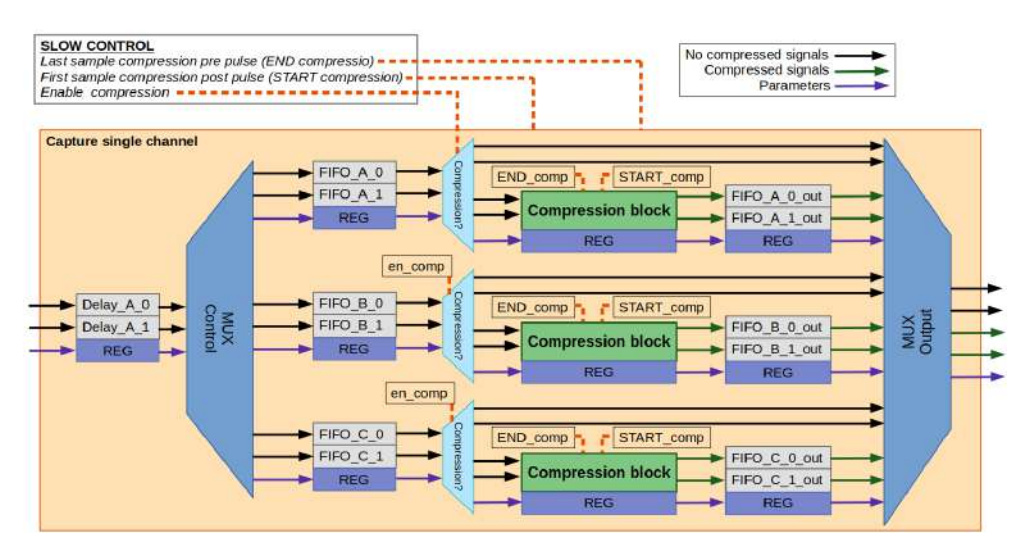


Figure 5.13: Compression blocks location and new design inside the Capture Single Channel block

The Slow Control is used to control from outside the FPGA which samples must be compressed and which must not. If compression is enabled, the data will pass through the compression block. Otherwise, they will go directly to the output multiplexer. In addition, the compression parameters END\_compression and START\_compression will be inputs (from Slow Control) to the compression blocks to control the last compressed sample before the pulse and the first sample to be compressed after the pulse.

Finally, if the event has been compressed, the trace is stored in the output FIFO, and the output multiplexer is in charge of managing the event to be output from the "Capture Single Channel" block.

Regarding the compression blocks, they consists mainly of three interconnected FSM (Finite-State Machines), creating a processing pipeline to optimise execution time. This technique allows multiple samples to be processed per clock cycle. In the following, the operation of the state machines is described in detail.

• **Differences FSM:** The first state machine, shown in Fig. 5.14, calculates the differences between each sample of the trace and the reference sample. In the implementation of this method in Python, the first sample has been used as a reference, but in the case of the firmware implementation, it has been decided not to compress the second sample either and to take this one as a reference. Thus, the first two samples (even and odd) are treated and transmitted in the same way.

In this FSM, the input samples come from the FIFOs of the Capture Waveform block. Thus, the odd and even samples are received

in parallel. The FSM has three states: INIT, FIRST\_SAMPLES, and DIFF\_SAMPLES.

- The input signals (sample\_diff0\_in\_sig, sample\_diff1\_in\_sig) are set to zero in the INIT state. If the write\_in signal (readout enabling signal) is asserted and the enable\_comp (compression enabled by Slow Control) signal is asserted, the state machine transitions to the FIRST\_SAMPLES state.
- In the FIRST\_SAMPLES state, the first samples of the (Sample0\_in\_sig and Sample1\_in\_sig) are copied to Sample\_0\_diff\_sig and Sample\_1\_diff\_sig without calculating the difference. This is because the first sample of Sample1\_in\_sig will be taken as a reference to calculate the differences. For this purpose, the Sample\_1\_diff\_sig signal is copied to the Sample\_ref signal and remains as a reference sample. The state machine then transitions to the DIFF\_SAMPLES state.
- In the DIFF\_SAMPLES state, the difference between the current (SampleO\_in\_sig and Sample1\_in\_sig) and reference samples (Sample\_ref) is calculated and the results sent to Sample\_0\_diff\_sig and Sample\_1\_diff\_sig provided that these are within the compression sections. The difference is calculated whenever the state of pack\_state is not SAMPLES\_peak. In this case, the signals are copied directly, from SampleO\_in\_sig and Sample1\_in\_sig to SampleO\_in\_sig and Sample1\_diff\_sig. Finally, when the write\_in signal is deasserted, the state machine returns to the INIT state.

Figure 5.15 shows an example of a chronogram of operation of this FSM, where  $Sample0\_in\_signal$  and  $Sample1\_in\_signal$  are the inputs and,  $Sample0\_diff\_sig$  and  $Sample1\_diff\_sig$  are the outputs with the samples in differential format. The output signals are stored in two FIFOs, one for even and one for odd samples.

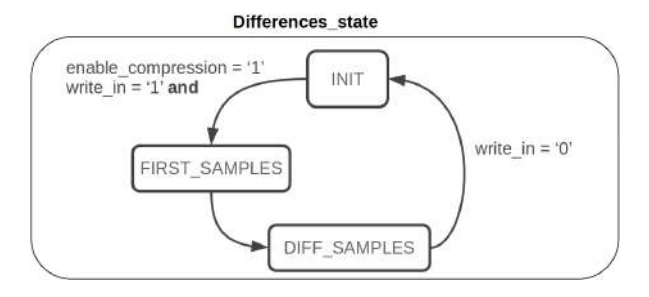


**Figure 5.14:** Differences FSM performs the calculation of the difference between current samples and the reference sample (second sample).

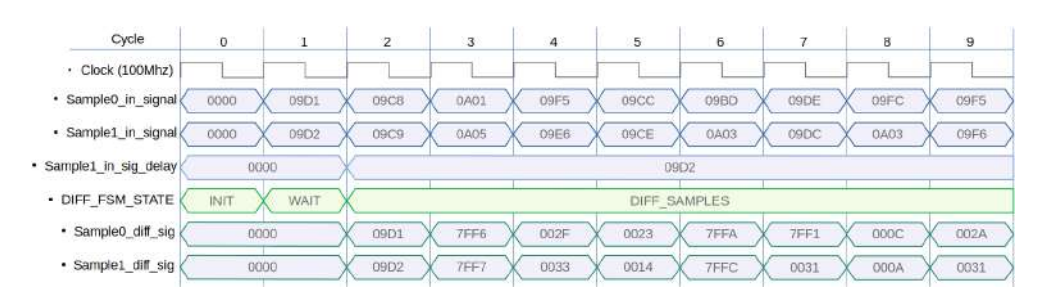


Figure 5.15: Example of initial cycles of Differences FSM.

• Control FSM: This FSM, shown in Fig. 5.16, uses counters to control which sections of the input signal are to be compressed and which remain uncompressed. By Slow Control, it is selected from which sample of the trace the compression is stopped (END\_compress) and from which sample the compression is resumed after the pulse (START\_compress). These two values are used as inputs in this FSM. When the acquisition reaches the sample number corresponding to the value of END\_compress, the samples are no longer compressed. On the other hand, the compression starts again when the sample number is equal to the value selected for (START\_compress). Finally, once the write\_in signal is deactivated, the state machine goes back to the INIT state.

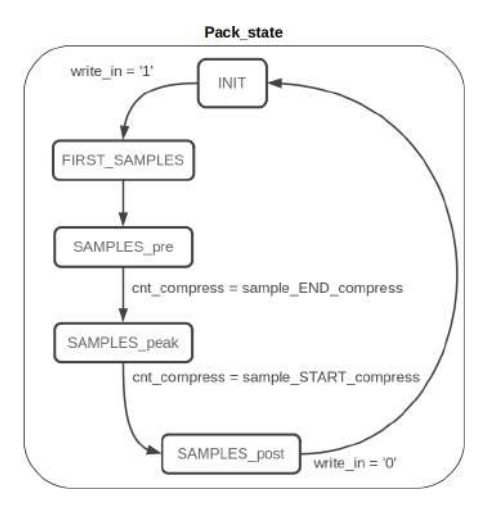


Figure 5.16: Control FSM controls the compression and non-compression sections.

• Joining FSM: This FSM, shown in Fig. 5.17 receives the *sample\_diff0-in\_sig* and *sample\_diff1\_in\_sig* signals and concatenates the lowest 8 bits of each signal. The result of this union is sent to the *SAMPLE0\_out\_sig*, and *SAMPLE1\_out\_sig* signals alternately and stored in two output FIFOs.

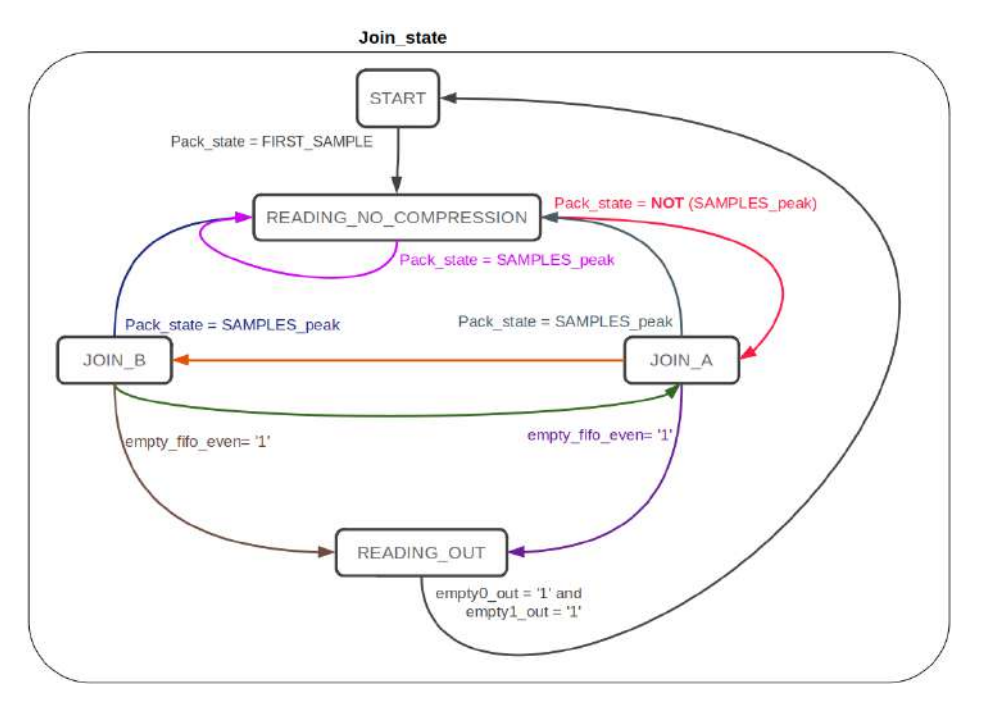


Figure 5.17: Joining FSM performs the merging of two consecutive samples (even and odd).

In this way, the signals are joined together and ready for reading out. Each FSM state is detailed below:

- In the START state, when *current\_state* is equal to FIRST, the FSM transitions to the READING\_NO\_COMPRESSION state.
- During the READING\_NO\_COMPRESSION state, the sample\_diff-0\_in\_sig and sample\_diff1\_in\_sig signals are copied into SAMPLE0\_out\_sig and SAMPLE1\_out\_sig without performing compression as they are samples that are not in differential format. It happens with the first signal sample and as long as the pack\_state is the same SAMPLES\_PEAK. Otherwise, the FSM transitions to the JOIN\_A state and writing to the output FIFO is enabled.
- In the JOIN\_A state, the lowest 8 bits of sample\_diff0\_in\_sig and sample\_diff1\_in\_sig are also concatenated and copied into SAM-PLE0\_out\_sig. Then, the FSM transitions to the JOIN\_B state, and the reading of the output FIFO's is disabled. On the other hand, if the pack\_state is equal to SAMPLES\_peak, the FSM transitions to the READING\_NO\_COM-PRESSION state. Finally, if the pack\_state is equal to INITIAL, the FSM switches to the READING\_OUT state.
- In the JOIN\_B state, the same compression process is performed

as in JOIN\_A, but the data are copied to SAMPLE1\_out\_sig. Also, if the pack\_sta-te is equal to SAMPLES\_peak, the FSM transitions to the READING\_NO\_ COMPRESSION state. Instead, when the FSM transitions to the JOIN\_A state, the reading of the output FIFOs is enabled to save the samples in the next cycle. Furthermore, as in the JOIN\_A state, if pack\_state is equal to INITIAL, the FSM switches to the READING\_OUT state.

- Finally, in the READING\_OUT state, the output reading of the compressed signal is performed. The reading starts from the first cycle and keeps enabled until the FIFOs are empty (empty0\_out = '1' and empty1\_out = '1'). So when both empty0\_out and empty1\_out signals are asserted, the FSM transitions to the START state.

Figure 5.18 shows the first cycles of the state machine. It includes the input signals in differential format and the output signals in compressed format, where the lowest 8 bits of the odd and even signal have been taken. In addition, the write signal in the output FIFO is shown. This signal is enabled when four samples (64 bits) are compressed and sent to the output signals occupying half of the bits (32 bits).

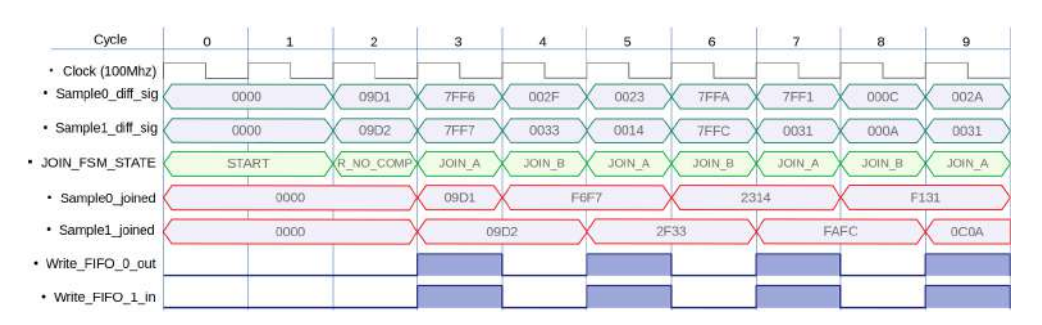


Figure 5.18: Example of initial cycles of Joining FSM.

As shown in the figure Fig. 5.19, the Differences and Joining FSMs are interconnected, creating a pipelining to work simultaneously with consecutive samples in different compression phases. For example, in the third cycle, the differences between samples 4 and 5, and the reference, are calculated by obtaining samples 4 and 5 in differential mode (SAMPLE4') and (SAMPLE5'). Meanwhile, in the same cycle, samples 2' and 3' (already in differential mode) of 16 bits each are being joined into a single 16-bit signal composed of SAMPLE2" and SAMPLE3" of 8 bits.

Although the compression time of two samples is only 2 cycles (10ns), from the time they arrive at the compression module until they are compressed into 16 bits, it is not until the entire trace of the signal is compressed, that it can be read out. For this reason, it is interesting to calculate the difference in processing time between sending an uncompressed or compressed

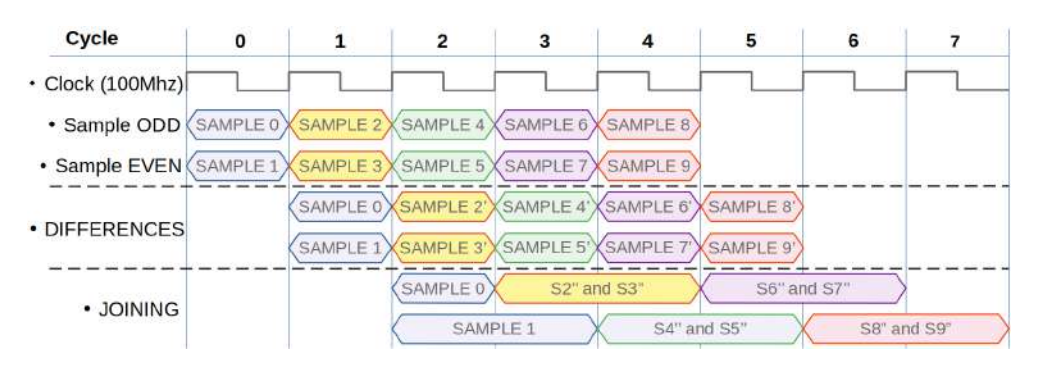


Figure 5.19: First cycles of all state machines.

trace. The uncompressed processing time, up to the moment when the readout is started, is 1.3us. In contrast, the compressed processing, with the parameters END\_compression = 32 and START\_compression = 100 have been taken, thus compressing 178 samples, achieving 35% reduction, and needing a total processing time of 2.66 us. So the difference between compressing and not compressing is 1.36 us. Using other parameters, for example, with END\_compression = 36 and START\_compression = 90, 202 samples are compressed and reduced 35% in size, needing the same processing time, 2.66 us. Thus the processing time to readout is always the same regardless of the reduced size in the compression.

As just discussed, the processing time increases with compression, as mentioned at the beginning of this section, so three compression blocks have been included in each channel. With this architecture, if the first block is busy and a new event arrives, it can be processed in the second block. If both are busy and an event arrives, it will be processed in a third block.

Finally, it should be noted that this compression method is not prepared to compress events that contain pile-up signals. Hence, if during the time window of the pulse, 1.28 us (256 samples), another ZCO is detected in the DCFD block, this event shall be sent uncompressed.

Regarding the implementation, the total resources used in the firmware, including the compression modules, are shown in Fig. 5.21. Compared to the resources used without the compression modules, the resource usage has risen by 7.66%, and none of the individual, shown in Fig. 5.21, resources exceeds 90%. In addition, the complete design is available in detail in the following repository: https://github.com/jmdeltoro/trace\_compression\_NEDA

# 5.5 Test and results

Once the firmware was developed, the setup shown in Fig. 5.21 was used to compress, store, reconstruct, and check that they were correctly reconstructed without distorting the original signals.

Device Utilization Summary (estimated values)			E
Logic Utilization	Used	Available	Utilization
Number of Slice Registers	59937	160000	37%
Number of Slice LUTs	67963	80000	84%
Number of fully used LUT-FF pairs	33659	94241	35%
Number of bonded IOBs	56	600	9%
Number of Block RAM/FIFO	133	264	50%
Number of BUFG/BUFGCTRLs	25	32	78%

**Figure 5.20:** Table of resources needed by adding the 3 compression blocks per channel.

The compression tests were carried out using a Desktop Digital Detector Emulator DT5800D. With this emulator, it is possible to provide gamma and neutron signals with the same characteristics as those from a real NEDA detector. It also gives the possibility to add different levels of noise in the baseline, as well as pile-up signals. The emulator was connected to the PCB to convert the single-ended to differential (SEDIFF) signals. After this signal adaptation via HDMI, the signals are sent to the NUMEXO2, where signal processing and compression are carried out. Finally, the signals are sent via fibre optics to the server, where they are stored and reconstructed to check the correct compression and decompression performance.



Figure 5.21: Chain acquisition.

The first test was carried out by performing a signal acquisition using the parameters END\_compression = 32 and START\_compression = 140 for the compression. These were selected via Slow Control from the configuration PC.

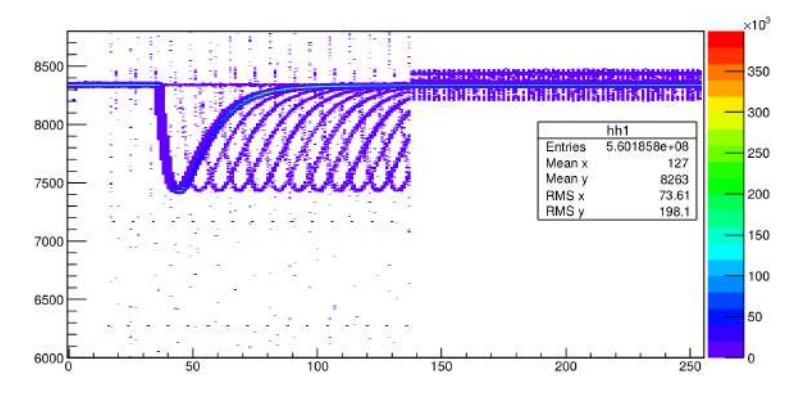


Figure 5.22: Acquisition with shifted events in decompression.

After the acquisition and signal compression, decompression was performed from the server to check that the signals were reconstructed correctly. It was observed that some signals were displaced during decompression, modifying the wave's shape and generating noise in the baseline.

Having analysed the acquisition chain, the origin of the shift in decompression was detected. The effect was produced because the buffer the driver uses for DMA (Direct Memory Access) of the PC server had a fixed size. When it became full, it was emptied and started receiving again. This characteristic generated that the size of each event did not fit with the size of DMA, so cutting and shifting them. In order to avoid this effect, the DMA buffer should be modified to adapt to the size of each event. This modification was not within the scope of this thesis and will have to be done in the future.

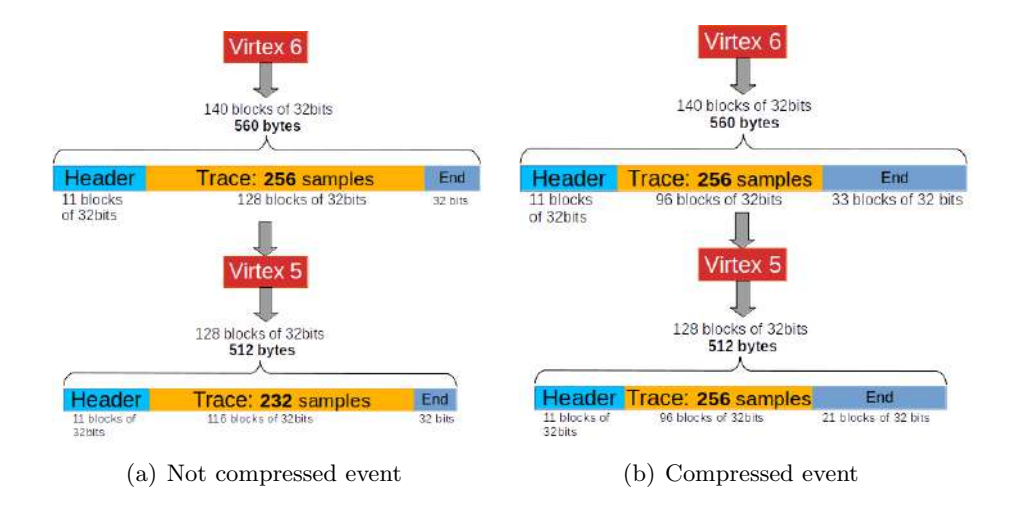


Figure 5.23: Comparison between compressed and uncompressed event.

Since the problem could be solved in the DMA, a firmware adjustment was made to keep the event size the same by adding useless bits at the end of the traces. In this way, the size of the events was maintained, but the traces were compressed. Figure 5.23 figure shows an example of comparing a compressed and an uncompressed event the compressed event is 512 Bytes to be able to use the driver currently in use.

Although were unable to compress the events (Header + Trace + End), at least, thanks to the compression, the samples that were discarded in Virtex-5 can now be kept. In addition to that, with this solution, it was possible to compress the traces and perform different tests with gammas and neutrons by varying the noise in the baseline and the rate.

First, the DT5800D emulator was configured with a constant rate of 10 kHz, with a noise level of 6.5 mV (the same level as that obtained with NEDA acquisitions) and only gamma ray signals. An acquisition was performed by

compressing the traces of each event and reconstructing them on the acquisition server. Figure 5.24 shows the gamma ray signals after reconstruction. Continuity is observed throughout the baseline, from which it can be deduced that the compression had no effect on the baseline after compression and decompression.

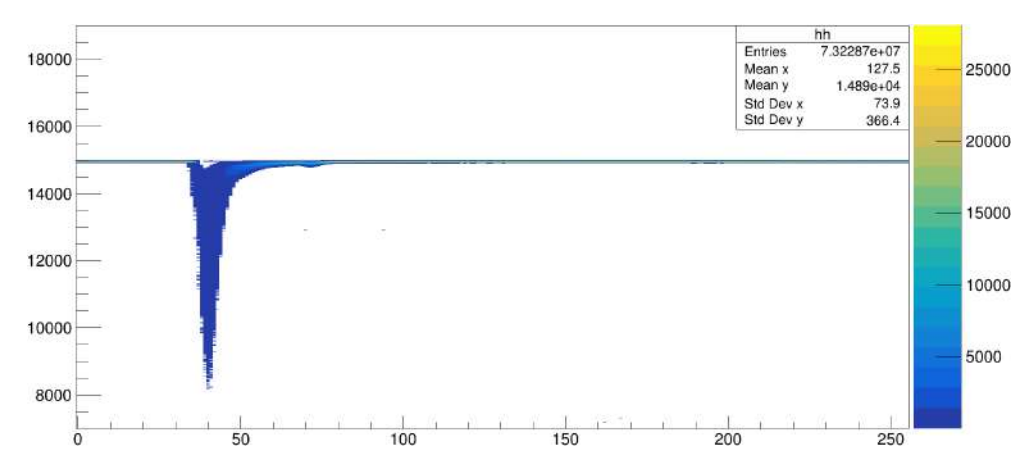


**Figure 5.24:** Decompressed gamma ray signals with a constant rate of 10 kHz and noise of 6.5 mV.

Secondly, the counting rate was maintained and the noise level was raised to 9.7 mV. In addition, neutron type signals were added to the gamma rays. As shown in Fig. 5.25, the baseline was continuous and the compression and decompression had no effect on the acquisition.

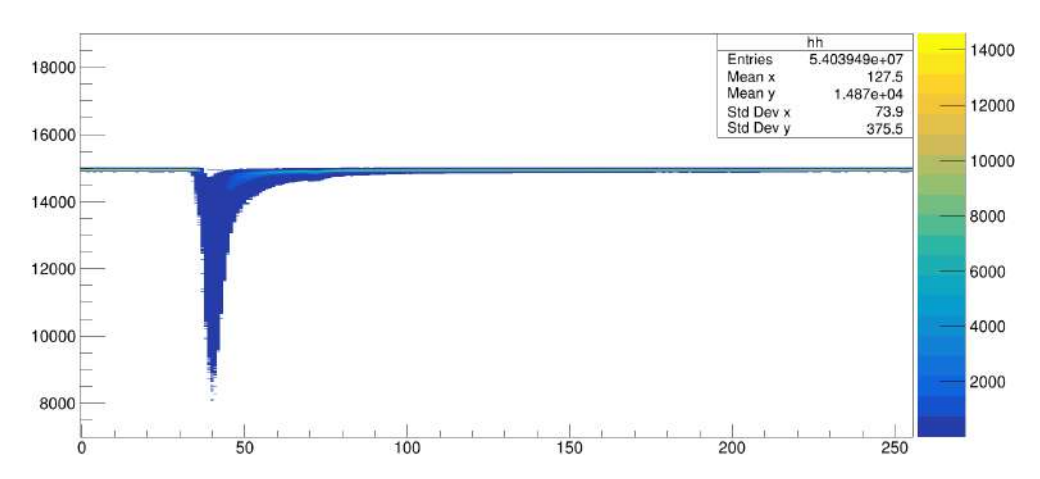


**Figure 5.25:** Decompressed signals neutron and gamma rays a constant rate of 10 kHz and noise of 9.7 mV.

Finally, to check how having a much higher baseline noise would affect the acquisition, the baseline noise was raised to 19.5 mV. In this case, as shown

in Fig. 5.26, a discontinuity was observed in the baseline. The noise in the compressed sections of the baseline is higher than expected. However, thanks to the fact that the samples corresponding to the peak and tail of the pulse are not compressed, these events could be analysed.

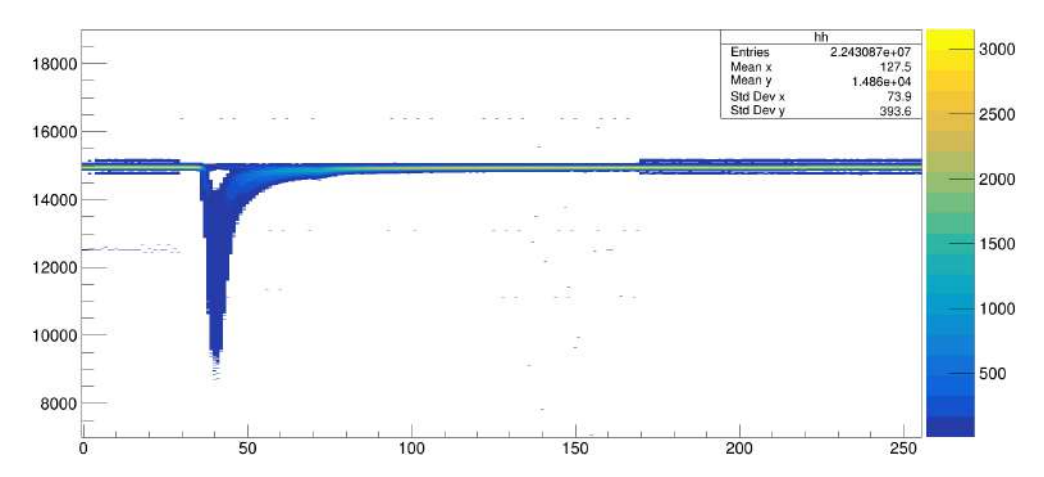


**Figure 5.26:** Decompressed signals neutron and gamma rays a constant rate of 10 kHz and noise of 19.5 mV.

When the improvement in the DMA is finally achieved, the excess bytes at the end of the traces can be removed. With this, the events will be reduced in size at the Virtex-6 output, and the counting rate could be increased. Considering the parameters used in the last tests, the event traces are 396 bytes instead of 512. So applying Eq. (5.1), the NUMEXO2 rate would be 316.8 MB/s. This means that using a NUMEXO2 of 409.6 MB/s, the counting rate could increase the bandwidth up to 65 kHz.

# 5.6 Conclusions

In conclusion, the implementation of data compression in the NUMEXO2 firmware using the Fixed sample size differential coding method has been carried out successfully. The goal of increasing the counting rate without exceeding the maximum transmission rate of 409.6 MB/s has been achieved. By reducing the number of bits required to represent the trace of each event, the counting rate has the potential to be increased significantly.

Various compression methods were studied, including Run-Length Encoding (RLE), Huffman coding, dictionary-based methods (LZ77, LZ78, LZW), and differential coding. The Fixed sample size differential coding method was selected as the most suitable for NEDA data compression. It achieved a compression ratio of 1.6, saving 37.5% of space, which was superior to other compression methods.

The Python implementation of the chosen compression method confirmed its feasibility, and subsequent tests using the Desktop Digital Detector Emulator DT5800D validated its performance. The firmware implementation in NUMEXO2, though not fully optimised due to DMA limitations, it demonstrated the successful compressing and decompressing of traces.

Overall, the Fixed sample size differential coding method has proven to be a viable and effective approach to data compression in NUMEXO2. Given that the data compression method can compress event traces preserving data integrity, the method optimises data transmission, making NUMEXO2 more efficient and capable of higher counting rates in experiments. Future improvements in DMA and event size reduction will likely lead to even more significant gains in counting rates and overall performance.

# Chapter 6

# Double Trigger condition system

This chapter studies the effect of implementing a double trigger condition system on data acquisition in NEDA. The system discussed here aims to improve neutron acquisition while reducing the acquisition of gamma rays. The firmware implemented, the tests performed, and analysis of the results obtained are described in this chapter.

# 6.1 Introduction

The NEDA cells exhibit sensitivity to neutrons, X-rays, and gamma rays. While shielding reduces X-ray interference, it proves impractical for higher energy gamma rays without compromising neutron detection efficiency. Gamma rays detected by NEDA cab be classified in two types, prompt gamma rays and uncorrelated gamma rays. The descriptions of these types are explained below:

- **Prompt gamma rays** are gamma rays emitted immediately following a nuclear reaction. They are typically emitted by atomic nuclei in an excited state that decays to a lower-energy state, releasing the excess energy.
- Uncorrelated gamma rays are gamma rays that have no direct causal relationship with the nuclear reaction of the experiment. They can come from several sources such as cosmic radiation, the de-excitation of radioactive nuclei, or the interaction of charged particles (such as protons, alpha particles, or electrons) with matter. In nuclear physics experiments, uncorrelated gamma rays can represent a background or noise that needs to be considered when analysing data.

Given this characteristic of the NEDA cells, developing techniques for discriminating between gamma ray (prompt and uncorrelated) and neutron events to determine the radiation's type becomes essential. In NEDA, PSA (Pulse-Shape Analysis) based on CC and TOF (Time-of-Flight) information is used for NGD. Based on information from CC and TOF, it is possible to classify the type of event. Figure 6.1 shows the selection of event types from a data collection accepting all events.

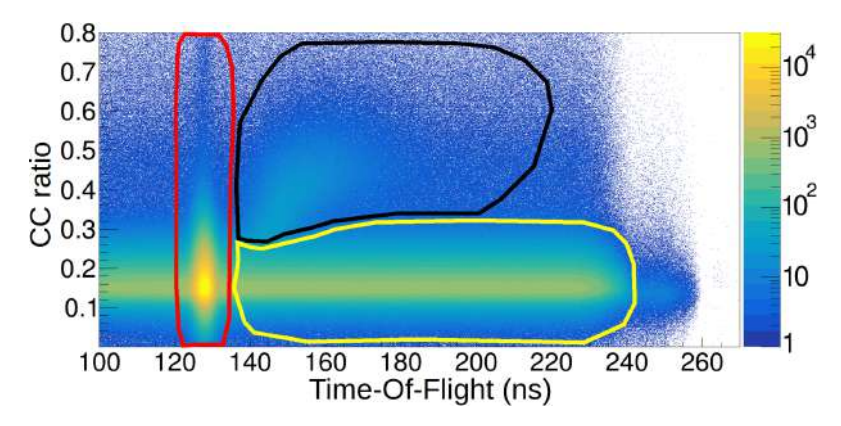


**Figure 6.1:** The black area encloses the neutrons, the red one the prompt gamma rays, and the yellow one the uncorrelated gamma rays.

Although the most accurate analysis and discrimination is performed offline, i.e., once the acquisition is made, from the front-end electronics, trigger requests are restricted online by the trigger conditions to reduce the large number of prompt and uncorrelated gamma rays that can be acquired. These trigger conditions significantly increase the proportion of neutrons among all acquired events.

In the first version of the NEDA electronics, the trigger method implemented in the firmware at the level of the digital pre-processing was based on the CC ratio. As previously mentioned, this method generates a trigger based on the ratio between two values computed integrating two regions of the signal, shown in Fig. 6.2: the fast component, containing the leading edge and the beginning of the falling edge (a few samples after Constant Fraction Discrimination (CFD) trigger), and the slow component, starting directly at the end of the fast component and extending along the pulse. If the ratio is above a certain threshold, the event is considered a neutron, whereas if it is below, the signal is considered a gamma ray.

Using the CC method, it is possible to significantly reduce the number of gamma rays accepted online. Figure 6.3 shows the events accepted online using the CC as a trigger method.

However, this method can lose low-energy neutrons because the reduced number of scintillation photons reduces the sensitivity of the CC method.

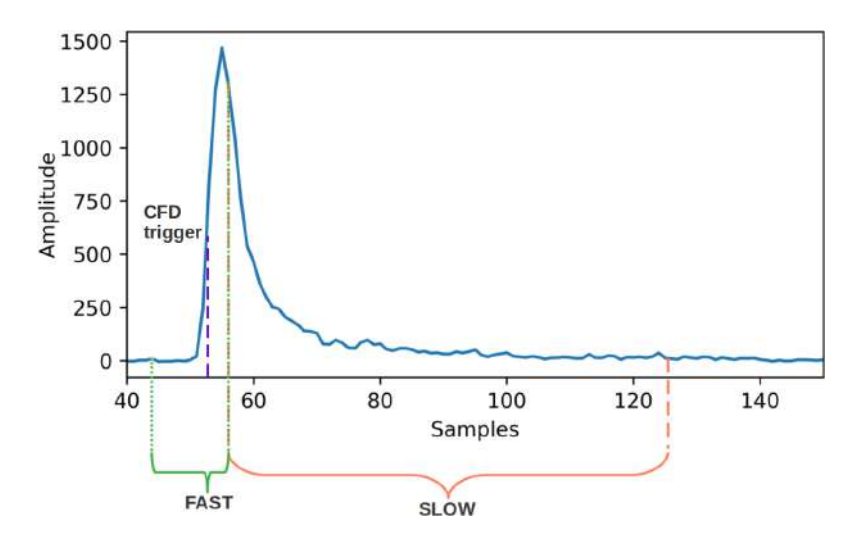
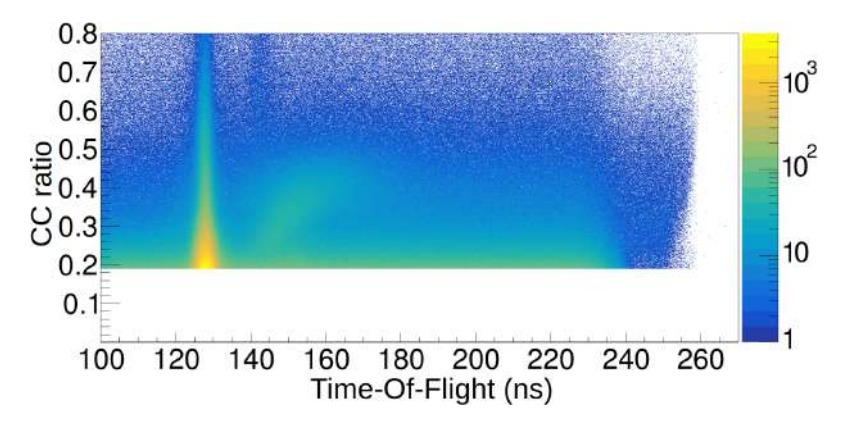


Figure 6.2: Slow and fast components of neutron and gamma-ray signals.



**Figure 6.3:** Acquisition using CC as trigger.

In order to acquire low-energy neutrons and reduce the trigger requests, the double trigger condition system was designed.

# 6.1.1 Double trigger concept and objective

The proposed double trigger condition system combines the CC ratio with additional event information to accept low-energy neutrons while reducing trigger requests. This additional information is the Time-of-Flight (TOF) of each particle. With the TOF information, it is also possible to identify the prompt gamma rays since their TOF is close to zero. In contrast, neutrons have a greater TOF as shown in Fig. 6.1. For NEDA, TOF is measured as the time difference between an external logical signal, such as the beam radiofrequency signal (STOP), and the signal generated within the NEDA cell (START).

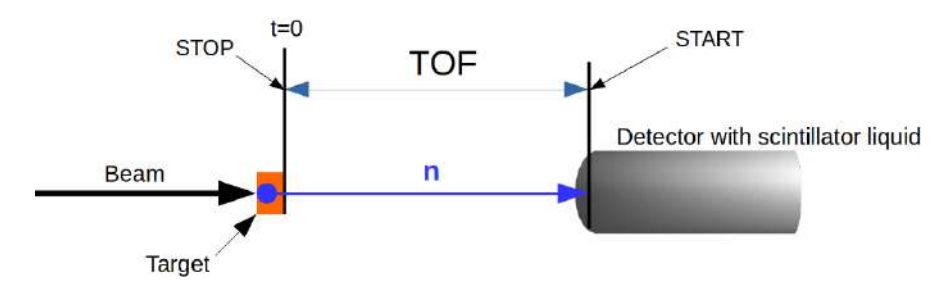


Figure 6.4: Schematic view of the TOF measurement concept for in-beam studies.

The introduction of this trigger method enables the use of two independent trigger signals that can be combined to generate a final trigger. Firstly, low-energy neutrons, undetectable by a system solely based on CC, can be captured using an OR logic to combine both trigger signals. Secondly, these two signals can be integrated with AND logic to decrease the high counting rate caused by prompt gamma ray events.

Consequently, four trigger modes are implemented for NEDA experiments, allowing the customisation of the trigger method for each experiment's specific objectives. The modes implemented are:

- CC mode: Only the trigger generated by CC is used;
- **TOF mode:** Only the trigger based on TOF is considered;
- **AND mode:** A trigger signal is generated when both methods generate a trigger;
- **OR mode:** A trigger signal is generated when either of the two methods generates a trigger.

This chapter aims to describe the implementation of this new functionality in the NEDA front-end and study the impact of using each trigger mode after performing offline analysis.

# 6.2 Firmware implementation

As mentioned in Chapter 4, the core component of NEDA electronics is the NUMEXO2 digitiser [61], featuring a Virtex-6 FPGA (Field Programmable Gate Array) and a Virtex-5 FPGA. The Virtex-5 interfaces with the Global Trigger and Synchronization (GTS) [44] system and manages data readout interfaces. The new double trigger condition system design is implemented in the Virtex-6 FPGA, using the outputs of independently obtained trigger signals as inputs. The NUMEXO2 digitiser has 16 acquisition channels, so this new functionality was independently implemented to each channel. Figure

6.5 shows the Virtex-6 firmware block diagram for a single channel, including blocks for the two trigger methods and the newly added Double Trigger block. During the implementation of this new functionality, particular attention was given to optimising the code and minimising FPGA resource usage, as the FPGA was already operating at 70% capacity.

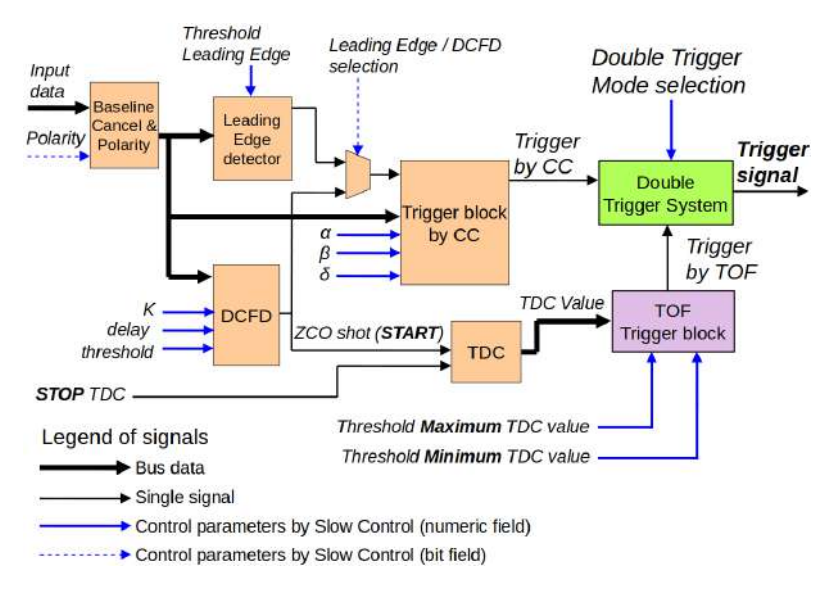


**Figure 6.5:** NUMEXO2 Virtex6 firmware blocks diagram including the newly implemented Double Trigger block (green box) and the TDC Trigger block (purple box). See text for details.

Following the signal path, the first firmware block focuses on baseline cancellation and polarity inversion (illustrated as the leftmost block in Fig. 6.5). In this block, input samples come directly from the ADC mezzanines [59], which digitise the detector signal at 200 Msps. Users can individually set the offset baseline of each channel and signal polarity using dedicated registers.

At the output of this block, the baseline of the signal is subtracted, and the digital pulse of the detector becomes positive, independent of the original signal polarity. This processed pulse is then directed to three blocks: (1) the Leading Edge, (2) the Digital Constant Fraction Discriminator (DCFD), and (3) the trigger block based on Charge Comparison (CC).

The firmware detects the arrival of an event through two methods. The first method is in the Leading Edge block, where a boolean output signal is generated based on whether the input pulse exceeds a set threshold, indicating the presence of a pulse. The second method in the DCFD block performs the standard constant-fraction discriminator operation with configurable attenuation (K), delay, and threshold for each channel. From the DCFD, Zero-CrossOver (ZCO) detection is used as a time reference signal, indicating the pulse's arrival.

The same ZCO detection is used as a START signal for the TOF measurement using a Time-to-Digital Converter (TDC) with the STOP coming from the accelerator radio-frequency signal.

The CC-based trigger block analyses the signal generated in the detector to distinguish between gamma rays and neutrons. The following operation carries out this discrimination:

Trigger if: 
$$\hat{I}_s > \delta \cdot \hat{I}_f$$
 (6.1)

Here,  $\hat{I}_s$  represents the integral of the slow component of the input signal, while  $\hat{I}_f$  represents the integral of the fast component. The threshold parameter,  $\delta$ , which can be adjusted using Slow Control (as shown in Fig. 6.5), determines when a signal is triggered. Additionally, the number of samples used to compute the fast and slow components can be selected via Slow Control, and these are denoted by the  $\alpha$  and  $\beta$  values, respectively, as illustrated in Fig. 6.5.

The TDC block measures the Time of Flight (TOF) between the Zero Crossing Output (ZCO) signal and the external reference signal from the accelerator's radiofrequency to generate a TDC value. This value is processed in the TOF Trigger block (shown in purple), where the trigger signal is activated when the TDC value falls within a user-configurable range, defined by the lower  $(t_{min})$  and upper  $(t_{max})$  thresholds. Therefore the trigger is determined using the following expression:

Trigger if: 
$$t_{MIN} < TDCvalue < t_{MAX}$$
 (6.2)

The Double Trigger System block receives the trigger signals from the CC and TOF trigger blocks. Finally, it generates the final trigger signal at the output based on the trigger mode selected by the user.

Control parameters are integrated into the Slow Control system to manage the trigger modes and their respective thresholds effectively. These new controls necessitate updating the firmware and the Slow Control script. The architecture now supports the independent adjustment of trigger methods, CC thresholds, and TOF thresholds for each channel, enhancing the system's versatility.

# 6.3 Functional test

The purpose of the functional test was to evaluate the performance of the double trigger implementation by examining the firmware's performance of the trigger modes. Specifically, the test checked if, during the online acquisition, the CC, TOF, AND, and OR trigger modes correctly discarded events that fell outside and retained events within the set thresholds.

For this functional test, a  $^{252}$ Cf source was positioned between a BaF<sub>2</sub> detector (with a diameter and length of 2.54 cm) and a NEDA detector at distances of 0.1 cm and 30 cm, respectively, as depicted in Fig. 6.6.  $^{252}$ Cf presents the advantage of being a mixed field-radiation source with a broad neutron energy distribution similar to the one observed in fusion evaporation reactions.

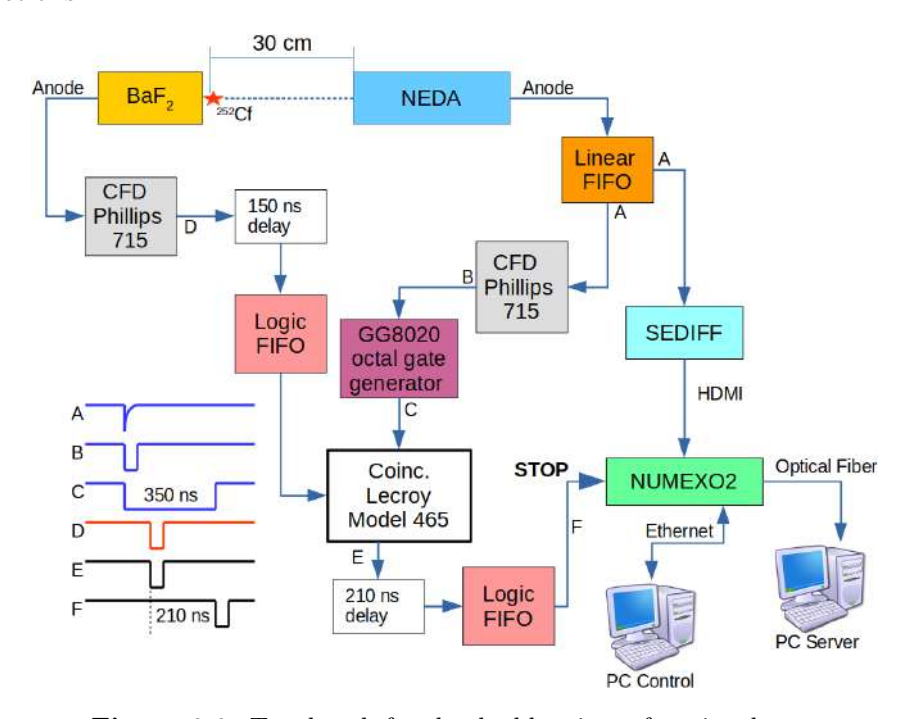
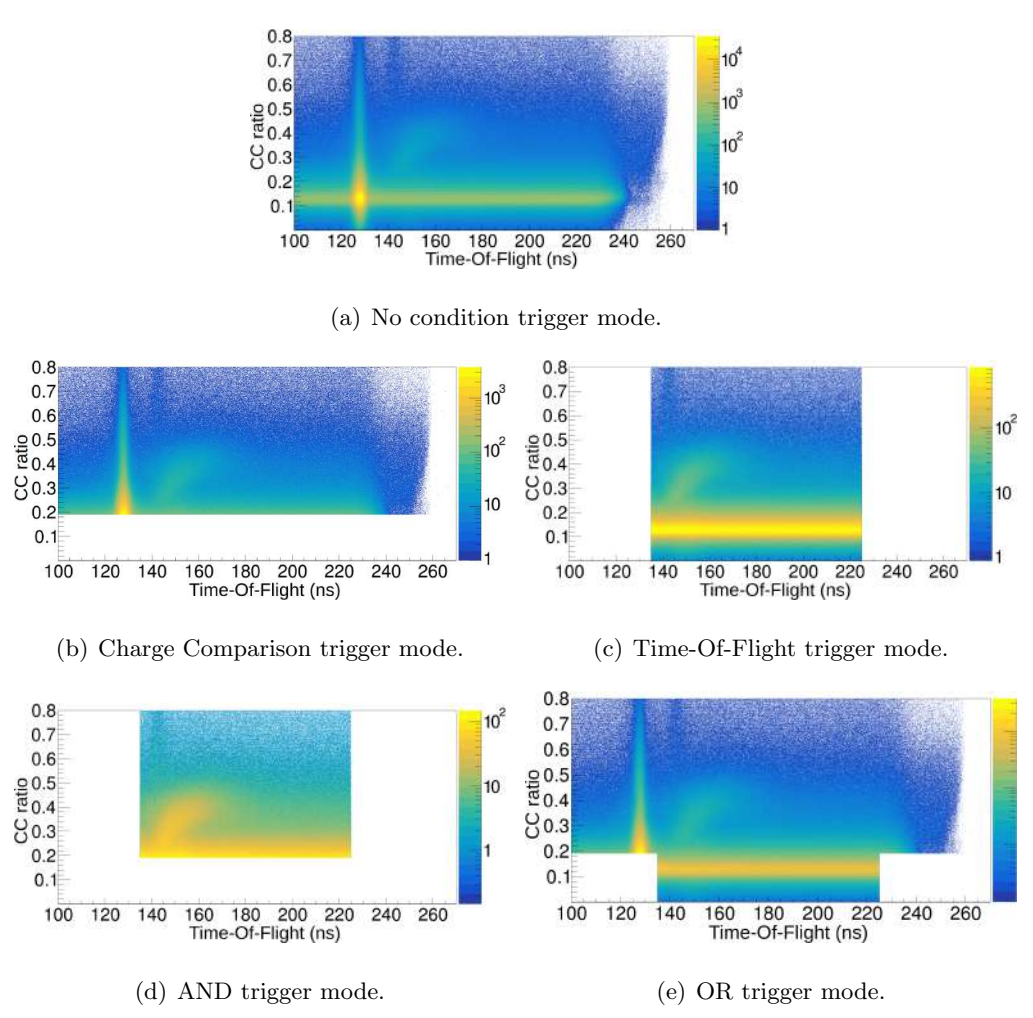


Figure 6.6: Test bench for the double trigger functional test.

In the setup the signal was divided into two parts using a linear fan-in fan-out (referred to as signal A in Fig. 6.6). One of these output signals was directed to the NUMEXO2 digitiser after being processed by a Single-Ended to DIFFerential (SEDIFF) module, which converted the unipolar signal into a differential signal. The other signal was sent to an analogue constant fraction discriminator (CFD Phillips 715), which generated a logical NIM signal (signal B). An octal gate and delay generator (ORTEC GG8020) created a coincidence window of 350 ns (signal C), setting the logic signal with the appropriate coincidence time width. The BaF<sub>2</sub> signal was processed through a CFD analogue module to generate a reference logic NIM signal (signal D). A coincidence unit (Lecroy 465) produced a logical NIM signal (signal E) when the NEDA and BaF<sub>2</sub> detectors were in coincidence. Due to the cable length and processing time within the NUMEXO2, this signal was received before the DCFD block had generated the START signal. Therefore, it was necessary to delay it to produce the STOP signal (signal F), which was input into the NUMEXO2 to obtain the TDC value.

The NUMEXO2 transmitted the accepted event to the data acquisition server via optical fibres. The Slow Control's different parameters were managed from a computer through an Ethernet connection.

Using the configuration shown in Fig. 6.6, the operation modes of the double trigger system were evaluated. The subfigures in Fig. 6.7 display the accepted events based on the results and thresholds of CC (on the Y-axis) and TOF (on the X-axis), which were computed on the Virtex-6 FPGA. The thresholds used were 0.19 for CC and 135 and 225 for TOF.



**Figure 6.7:** Functional test using the four trigger modes, and acquisition without trigger condition.

Figure 6.7(a) depicts the event distribution when all events are accepted, i.e. without trigger conditions. Figure 6.7(b) demonstrates how a CC trigger condition inhibits the capture of signals with a lower  $\delta$  than the one set. Figure 6.7(c) presents the impact of the TOF trigger mode, where events that fall

below the lower or exceed the upper thresholds are not captured. Figure 6.7(d) illustrates the outcome of applying an AND condition to the CC and TOF triggers, where only signals that exceed a CC threshold and fall within a specific TOF range are accepted. Last, Fig. 6.7(e) displays the result of the OR trigger mode, where the system discards signals that fall below the CC threshold and outside the TOF range. All these outcomes confirm the proper operation of the double trigger condition system with the described setup.

# 6.4 In-beam results

Following the functional verification, the double trigger condition system was validated using data from in-beam experiments. The influence of each trigger mode was assessed after conducting an offline analysis and neutron-gamma discrimination. The analysis focused on how the TOF, AND, and OR trigger modes impacted the number of neutrons accepted after the offline PSA analysis, compared to the scenario where only the CC online trigger mode was utilised.

A specific dataset from the E703 experiment, where no trigger condition was applied at the firmware level, was used to evaluate the double trigger condition system. The E703 experiment carried out at GANIL with AGATA and the ancillary NEDA, Neutron Wall, and DIAMANT detectors aimed to study excited states above the  $6^+$  isomer in  $^{102}\mathrm{Sn}$  and  $^{103}\mathrm{Sn}$  using a  $^{58}\mathrm{Ni}$  beam impinging on a  $^{50}\mathrm{Cr}$  target at 200 MeV. Figure 6.8 shows the layout of the experimental setup.

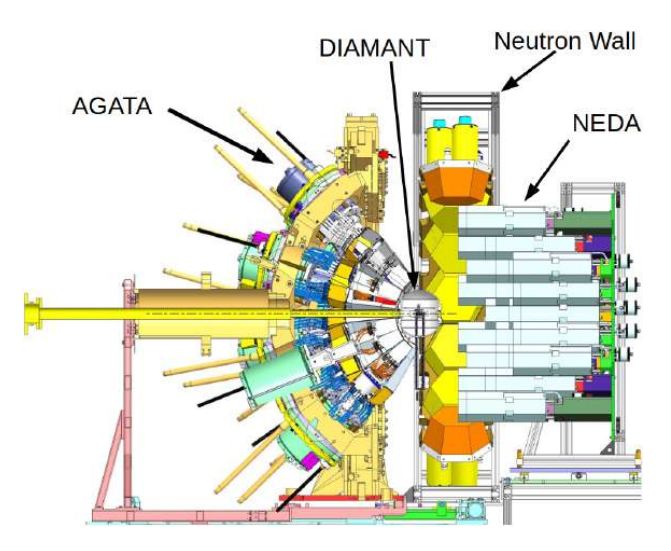
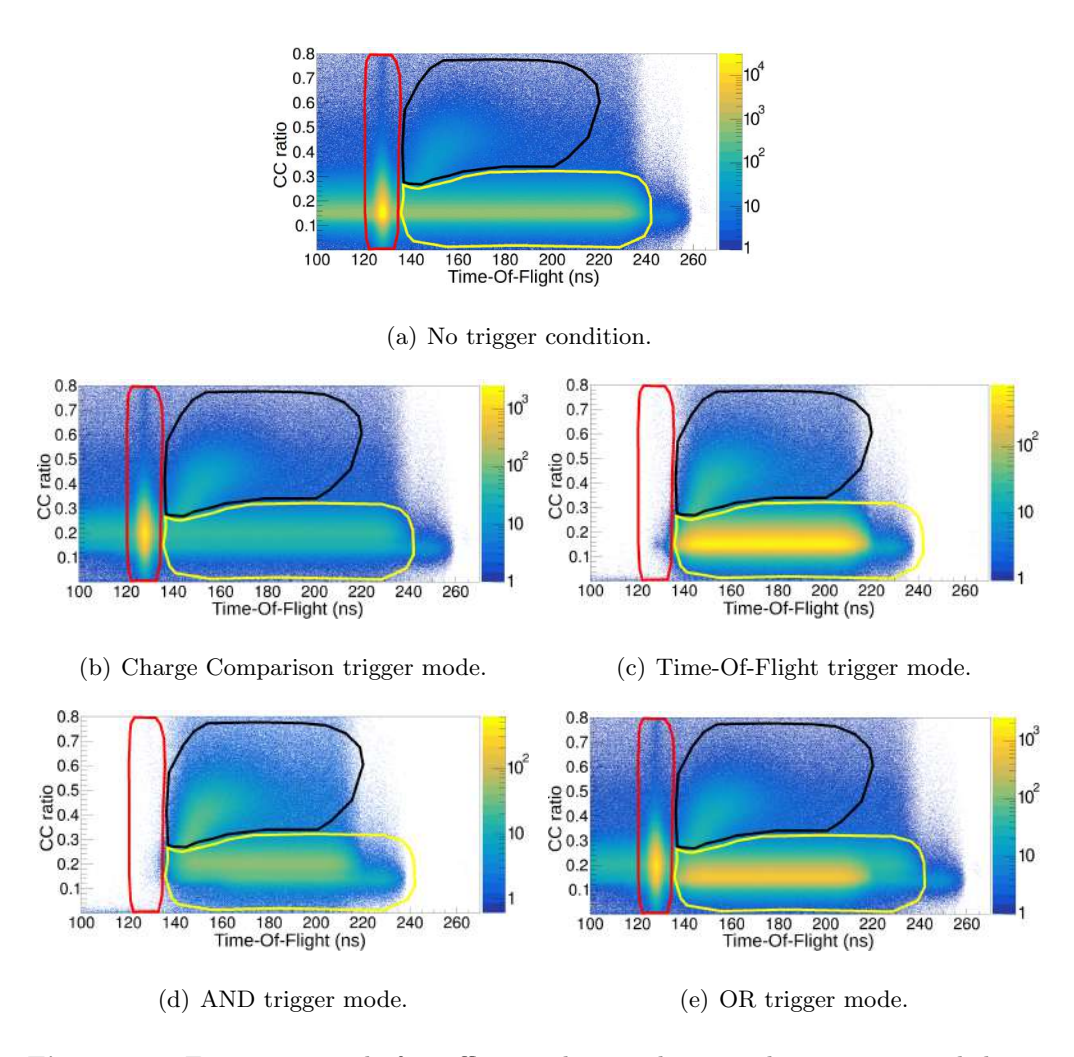


Figure 6.8: NEDA + AGATA + Neutron Wall + DIAMANT structure.

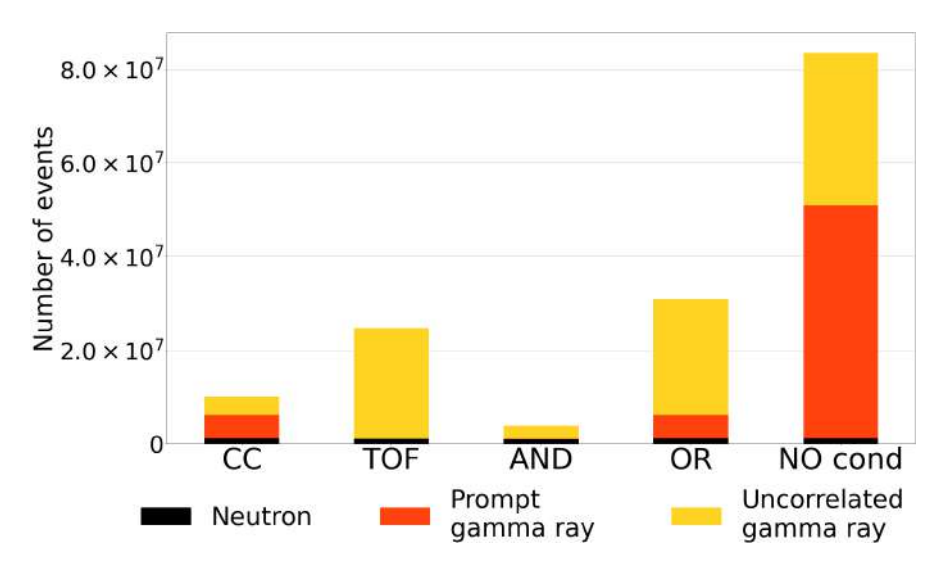
The dataset included events from all NEDA detectors, with aligned offline CC and TOF information. This data was utilised to perform the offline neutron-gamma discrimination. Following this analysis, examining other datasets from the same experiment delivered the appropriate selection zones (CUTs) for each event type (neutron, prompt gamma, or uncorrelated gamma). Figure 6.9(a) shows the three regions: the black CUT encompasses the neutrons, the red one includes the prompt gamma rays, and the yellow one contains the uncorrelated gamma rays. By adding the number of events in each CUT, we obtained the count of events of each type. Figure 6.10 ("NO cond" column) presents the result of each integral without trigger conditions. This result was used as the reference to compare the number of neutrons and gamma rays acquired with each trigger mode.



**Figure 6.9:** Events accepted after offline analysis without condition trigger and the four trigger modes with CC threshold in 0.19. Some events exceed the thresholds established at the firmware level due to the more accurate offline pulse shape analysis.

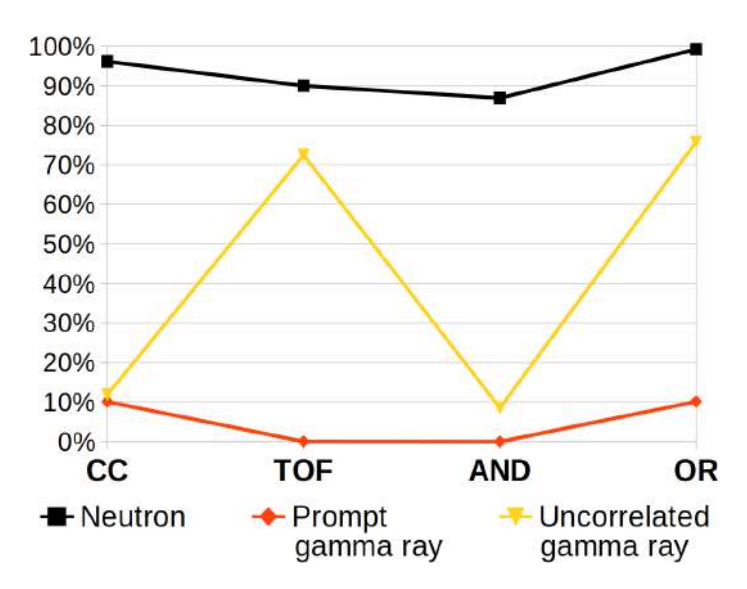
Next, the same process was followed by applying the four trigger modes and emulating the trigger conditions in the trigger blocks at the firmware level. The accepted events after the offline analysis are shown in Figs. 6.9(b) to (e). The same CUTs were also applied, and their integrals were calculated to obtain the number of events of each type. Regarding the trigger conditions (online CC with threshold at 0.19 and online TOF with lower and upper thresholds 135 and 225), the same ones applied during the functional test were maintained. As can be seen in subfigures of Fig. 6.9, events appear that do not meet the online trigger conditions. Events appear with a CC ratio less than 0.19, and with TOF values less than 135 and greater than 225. This effect was produced because, in offline analysis, more advanced analysis techniques were used to improve the pulse quality to perform the CC, such as enhanced baseline elimination and to improve the value of TOF through techniques such as interpolation. This effect caused the CC ratio and TOF of some events to differ from that calculated online in the Virtex-6.

Figure 6.10 shows the total events acquired without trigger condition and with each trigger mode, including the contribution of each type of event to the total, taking into account the integrals of each CUT after offline analysis. Figure 6.11 shows the percentage of accepted events compared to the case where no trigger condition is applied.



**Figure 6.10:** Total events by trigger mode and total events without trigger condition.

The first column of Fig. 6.10 presents the total number of events accepted using the CC trigger mode. A sum of 10,014,312 events were collected, which, as depicted in Fig. 6.11, constitutes the 96.14% of the neutrons and reduces the prompt gamma rays and uncorrelated gamma rays to 10.10% and 11.89%, respectively, in comparison to the acquisition without any trigger condition.



**Figure 6.11:** Percentage of particles acquired compared to acquisition without trigger condition, taking into account the different trigger modes.

The second column in Fig. 6.10 shows the outcomes when a TOF trigger was used. It reveals that while the number of events increases, the count of neutrons decreases compared to the CC trigger mode. However, there is a significant reduction (nearly to zero) of prompt gamma rays and a substantial increase in uncorrelated gamma rays.

For the AND condition, Fig. 6.10 indicates that, compared with the CC trigger mode, the number of events captured is reduced by up to 37.97%. This effect is because, with this trigger method, the trigger requests produced by prompt gamma rays were reduced to 0.01% compared to the case where no trigger condition was used, as shown in Fig. 6.11. Additionally, the number of neutrons captured is reduced by 9.23% (107,242 fewer neutron events) compared to those captured with CC as a trigger mode, as seen in Fig. 6.11.

The OR trigger mode, as illustrated in Fig. 6.11, enhanced neutron acquisition by 3.11% (36,092 more neutron events) compared to the CC trigger mode. Conversely, this trigger mode could not reduce the trigger requests produced by uncorrelated gamma rays, increasing the total acquired events by 308.53% (20,882,451 more events), as shown in Fig. 6.10.

We also examined the effect of the CC threshold on the results of the various trigger modes. The TOF mode was not analysed as the CC threshold had no influence in this case.

As shown in Fig. 6.12, with the CC and AND trigger modes, the proportion of accepted events decreased as the CC threshold increased. For instance, the percentage of neutrons with the AND trigger mode shifted from 86.91% to 71.44% when the threshold changed from 0.19 to 0.3. Additionally, the per-

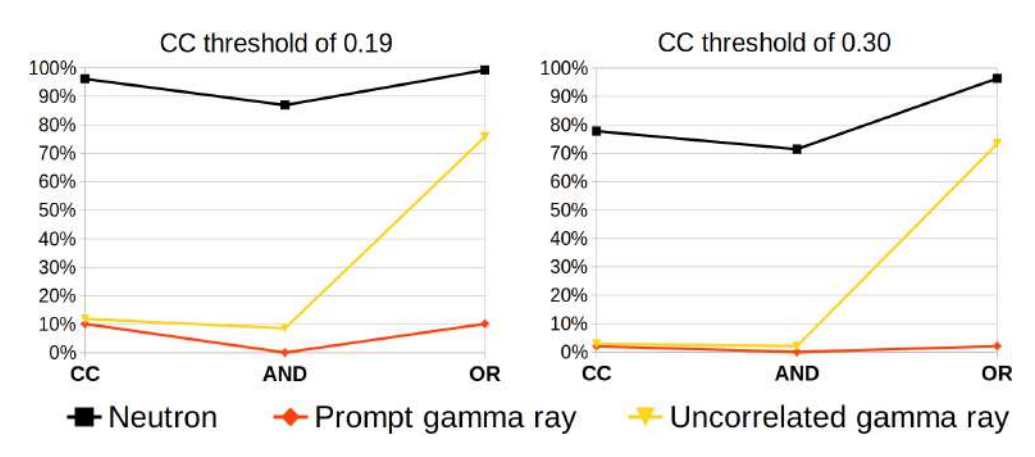


**Figure 6.12:** Percentage of particles acquired compared to acquisition without trigger condition. For the figure on the left a CC threshold of 0.19 was used and for the one on the right 0.3.

centage of prompt gamma rays was reduced to 0%, and uncorrelated gamma rays decreased from 8.56% to 2.08%.

Regarding the OR trigger mode, it was observed that the percentage of acquired neutrons only decreased by 2.87% ( $3 \times 10^4$  fewer neutron events) comparing the result using threshold of 0.19 and that of 0.3. The prompt gammas were reduced by 8.05% ( $4 \times 10^6$  fewer gamma rays) and uncorrelated gamma rays were reduced by only 2.49%.

## 6.5 Conclusions

After applying the four trigger modes on the E703 experiment's data, we conclude that the AND trigger mode can be useful in experiments where the data acquisition system requires a low level of trigger request, and it is not crucial to lose a little amount of neutron events. On the other hand, it is shown that the OR trigger mode can be interesting in experiments where it is crucial to lose the minimum possible number of neutrons as long as the acquisition system can handle a trigger requests at least three times higher than using the CC trigger mode. Finally, the results of this work show that in experiments where it is necessary to increase the CC threshold, it will be necessary to use the OR mode of the trigger to avoid losing neutrons.

In conclusion, developing and implementing the double trigger condition system for the NEDA represents a significant advancement in enhancing the capabilities of spectrometry setups. Combining two independent trigger signals based on CC and TOF measurements, the NEDA array can effectively discriminate between gamma rays and neutrons, thus improving the precision and accuracy of reaction channel selection. The versatile trigger modes (CC, TOF, AND, and OR) offer researchers a range of options to tailor the detec-

tion system to their specific experimental goals. These trigger modes expand the range of detectable neutron energies and provide valuable flexibility in controlling counting rates for various experimental scenarios. The firmware implementation using Virtex-6 FPGA and associated signal processing blocks demonstrates the feasibility of the proposed trigger system.

In nuclear physics research, the NEDA detector array, equipped with the double trigger condition system, offers enhanced capabilities for precise reaction channel identification and data acquisition.

# Chapter 7

# Pile-up reconstruction using a 1D-CAE

In this chapter, we study the NEDA pile-up events and present a new method for reconstructing them. This method uses a One-Dimensional Convolutional AutoEncoder (1D-CAE) to recover pile-up pulses to be analysed like non-pile-up pulses. This method is tested by reconstructing pile-up signals and evaluating the signals obtained.

# 7.1 Introduction

Pulse pile-up is a frequent problem in nuclear reaction and spectroscopy experiments with high counting rates. This effect occurs when pulses arrive so close in time that they completely or partially overlap. As a result of this effect, the pulses become distorted, as shown in Fig. 7.1. This distortion compromises the quality of energy and timing information, making it challenging to identify particle types using the usual pulse shape discrimination techniques [14,62,63]. Consequently, the pile-up pulses are typically discarded.

Various techniques have been developed to detect and eliminate consecutive pulses, employing digital and analogue methods. These methods include leading-edge discrimination, moment-analysis, Constant-Fraction Discrimination (CFD), Digital Constant-Fraction Discrimination (DCFD), triangular pulse shaping with leading-edge linear regression, and pulse-shape fitting, as studied in [64,65]. Additional methods involve analogue circuits [66], trapezoidal shaping [67], Position Shift Identification [65], Pulse Shape Discrimination (PSD) [68], neural networks [69], and Application-Specific Integrated Circuits (ASICs) [70] for pile-up rejection.

However, some rejected events contain valuable information. Consequently, methods have been developed to recover information from two or more pile-up pulses. These methods can be categorised into those refining the distorted

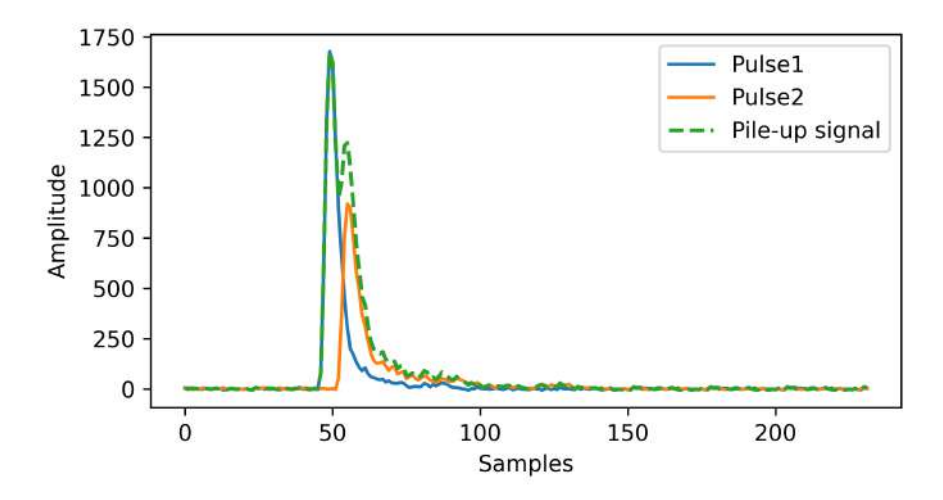


Figure 7.1: Example of a signal with pulse pile-up effect.

pulse height spectrum [71, 72] and those individually analysing the signals. Among the latter, some techniques extract pulse height information [73]. In contrast, others identify the type of particles corresponding to each pile-up pulse using Pulse Shape Discrimination methods and machine learning techniques [74–76].

In certain applications or experiments, complete reconstruction of both pile-up pulses is required. There are no general solutions for these pulse reconstructions that can be used for all applications. Therefore, specific solutions have been developed for particular cases, such as the fitting and extrapolation method [77–79] or the deconvolution method [80].

For instance, two methods have been developed for reconstructing pile-up events acquired with organic scintillators. The first method, based on pile-up model comparison [81], is designed for offline use. It involves multiple iterations to fit one of the pile-up models to the acquired signals. The second method employs machine learning techniques [82] and can reconstruct pulses, although limited to those separated by more than 60 ns.

This chapter studies an online pile-up event reconstruction method capable of recovering pulses with a time difference of 15 ns or more (3 samples @200 MHz). To ensure feasibility, the method must have low analytical and computational complexity and a short reconstruction time per event to integrate seamlessly into the overall analysis system.

As shown in Fig. 7.2, pile-up events are rejected during the offline analysis and, therefore, the CC offline is not carried out. This work aims to implement a pulse reconstruction method that meets all the requirements mentioned above to be included in the acquisition chain before the Offline Analysis, and verify its feasibility and efficiency. The future objective is to implement the reconstruction method in the digitiser.

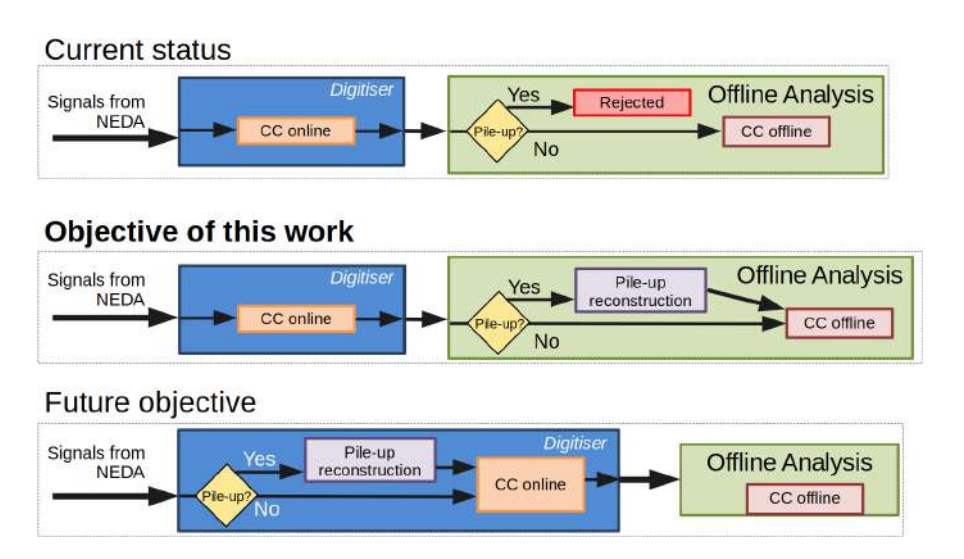


**Figure 7.2:** Current status reject the pile-up signals. The objective of this work is the development of a method for reconstructing pile-up signals before Offline Analysis. In the future it will be included in online signal processing.

Regarding the method to be used for reconstruction, the previously mentioned reconstruction techniques do not meet all the requirements and thus cannot be used for NEDA events. Therefore, this paper proposes an ad-hoc method using a 1D-CAE to disentangle the two pulses composing each pile-up event acquired with NEDA detectors.

# 7.2 Pile-up in NEDA detector

As mentioned in Chapter 1, one of the goals of this thesis is to provide the ability to increase the counting rate in NEDA experiments without modifying the existing hardware. Thanks to the online lossless data compression proposed in this thesis, it will be possible to increase the counting rate, increasing the probability of generating pile-up events. This makes it even more relevant to be able to reconstruct the pile-up events. Being able to separate and analyse these events is a great step forward in order not to lose pile-up events produced in the experiments.

As described in Chapter 3, NEDA cells are sensitive to neutrons and gamma rays and the NGD techniques used are CC ratio and TOF information. However, when two pulses are generated very close in time by the same NEDA cell, the pile-up effect occurs, and the event is typically discarded since reliable CC information cannot be obtained. These two pulses can be produced by two neutrons arriving at the same NEDA cell, generating the neutron-neutron combination. It is also possible that a gamma ray arrives a few nanoseconds after the arrival of a neutron, giving rise to the neutron-gamma combination.

The opposite is also possible, a neutron arrives and shortly after a gamma ray, generating a gamma-neutron signal. Finally, the last possibility is that two gamma rays arrive at the same time at the same NEDA cell. So, four possible combinations of pile-up can occur: neutron-neutron, neutron-gamma, gamma-neutron, and gamma-gamma.

Not all four combinations are equally likely or detectable as pile-up signals. The neutron-neutron combination, where two neutrons arrive at the same detector, has a low probability of occurring, with a time difference typically less than 5 ns, causing the analysis to identify it as a single neutron, thus not detecting pile-up. The gamma-gamma combination is more likely; however, if two gamma rays arrive at the same detector simultaneously after the reaction, they will be identified as a single gamma ray. The neutron-gamma combination is likely when a neutron is detected first, followed by a spurious gamma ray from natural background radiation. This gamma ray can appear at any moment during the acquired signal. Lastly, gamma-neutron pile-up events occur when gamma rays from the reaction are detected first, followed by a neutron. A longer or shorter TOF will be observed depending on the detector's distance from the reaction. With the standard NEDA setup, a distance of 100 cm is typical, resulting in an average neutron flight time of 40 ns. Given these characteristics, pile-up reconstruction will focus exclusively on gamma-neutron or neutron-gamma events.

# 7.3 1D-CAE architecture for NEDA pile-up event reconstruction

Pile-up signals must be reconstructed and treated similarly to non-pile-up signals. In our case, the pile-up problem is approached as a time series problem in which single dimension data are separated and reconstructed., where single-dimensional data. This study focuses on solving the pile-up problem using a One-Dimensional Convolutional Autoencoder (1D-CAE).

A 1D-CAE combines the principles of both a One-Dimensional Convolutional Neural Network (1D-CNN) [83] and an autoencoder [84]. It uses convolutional layers for feature extraction and encoding sequential data, followed by decoding layers to reconstruct the input sequence. The architecture of a 1D-CAE typically consists of an encoder module, which applies one-dimensional convolutional filters to reduce the dimensionality of the input sequence, and a decoder module, which employs transpose convolutional layers to upsample and reconstruct the original sequence. The loss function used in training the 1D-CAE compares the input sequence with the reconstructed output sequence. Below, the two main concepts of the architecture, 1D-CNN and autoencoder, are explained, followed by the specific architecture used to reconstruct pile-up events.

#### 7.3.1 1D-CNN

A 1D-CNN [83] is a unique type of neural network architecture specifically designed to process sequential data like time series, signals, or text sequences. Unlike conventional CNNs [85], which work on two-dimensional grids such as images, 1D-CNNs handle data along a single dimension. This makes them particularly effective for tasks where the sequence of elements is significant.

The core operation in a 1D Convolutional Neural Network (1D-CNN) is the convolutional layer. This layer is responsible for identifying patterns or features in the input sequence, such as time series data, audio signals, or text sequences. It achieves this by applying a set of learnable filters (also known as kernels) to the input sequence. These kernels are fixed-size arrays (vectors in the 1D case) of weights that are learned during the training process. Each kernel is designed to detect a specific type of feature or pattern in the input sequence, such as edges in an image or trends in time series data.

The convolution operation involves the kernel sliding over the input sequence one element (or step) at a time. At each position, the kernel and the corresponding segment of the input sequence are element-wise multiplied and then summed to produce a single value in the output feature map. This operation can be expressed as:

$$output = input * kernel$$

$$output[i] = \sum_{k=0}^{+\infty} input[i-k] \cdot kernel[k]$$
(7.1)

Where k is the size of the filter and i is the current position of the filter on the input sequence. Typically, multiple filters are used in a single convolutional layer, each producing a different feature map, which allows the network to learn a variety of features from the input. The output of a convolutional layer is a set of feature maps, each corresponding to a different kernel, resulting in a transformed representation of the input sequence that highlights the detected patterns or features.

Typically, to manage the complexity of the model and prevent overfitting, a pooling layer reduces the size of the feature maps. Different pooling techniques like max pooling or average pooling can be used here. An activation layer is next, adding non-linearity with functions like ReLU. This layer is crucial for the model to learn complex relationships.

The fully connected layer connects all the neurons from the previous layer, allowing the model to learn even more intricate connections between the features and the desired outcome. Finally, the output layer delivers the final predictions. This layer might use a softmax function to predict probabilities for various categories in a classification task, or a linear function for continuous outputs in regression problems.

1D-CNNs find applications in predicting time series data, such as electrocardiogram (ECG) time series [86] or weather forecasting [87]. They are also employed in automatic speech recognition (ASR) [88], natural language processing, and signal identification.

#### 7.3.2 Autoencoder

An autoencoder [84, 89] is a type of neural network architecture used in machine learning and pattern recognition. It consists of two primary parts: an encoder and a decoder. The encoder compresses the input into a lower-dimensional representation. It reduces the dimensionality of the input data and captures the most important features. Subsequently, the decoder takes this lower-dimensional representation and tries to produce an output as close as possible to the original input. This entails employing a loss function that compares the decoder's output with the corresponding input, enabling the model to learn to reconstruct input data. The expression describing a autoencoder is:

$$L(x, x') = L(x, g(f(x)))$$
 (7.2)

Where:

- L denotes the loss function comparing the original input x with the reconstruction x' or g(f(x))
- f represents the encoder function that maps the input x to a lower-dimensional representation space.
- g represents the decoder function that reconstructs the original input from the lower-dimensional representation obtained by the encoder.

Several types of autoencoders are designed to address specific challenges in machine learning. Traditional autoencoders, also called densely connected autoencoders, are adaptable and frequently employed for tasks like reducing dimensionality and reconstructing data. Convolutional autoencoders [90] are particularly suitable for image reconstruction, as they effectively utilise convolutions to identify spatial patterns. Other types include variational autoencoders [91], which concentrate on generating new data, and denoising autoencoders [92], models designed to handle noisy data.

# 7.3.3 1D-CAE architecture and training

As mentioned earlier, the pile-up signals studied consist of two pulses in close temporal proximity. As depicted in Fig. 7.3, the proposed 1D-CAE architecture follows the usual structure of a 1D-CAE but with the particularity that it has a single input, which is the signal containing the two pile-up pulses

but two outputs, each corresponding to one of the pulses in the input signal. For this purpose, the encoder structure is shared, and the decoder is bifurcated, resulting in a separate decoder for each reconstructed pulse.

### 1D-CAE design

This design allows both pulses to be separately obtained and directly incorporated into the processing chain with a single model. This strategy facilitates integration into future NEDA hardware and firmware upgrades without disrupting the rest of the processing chain.

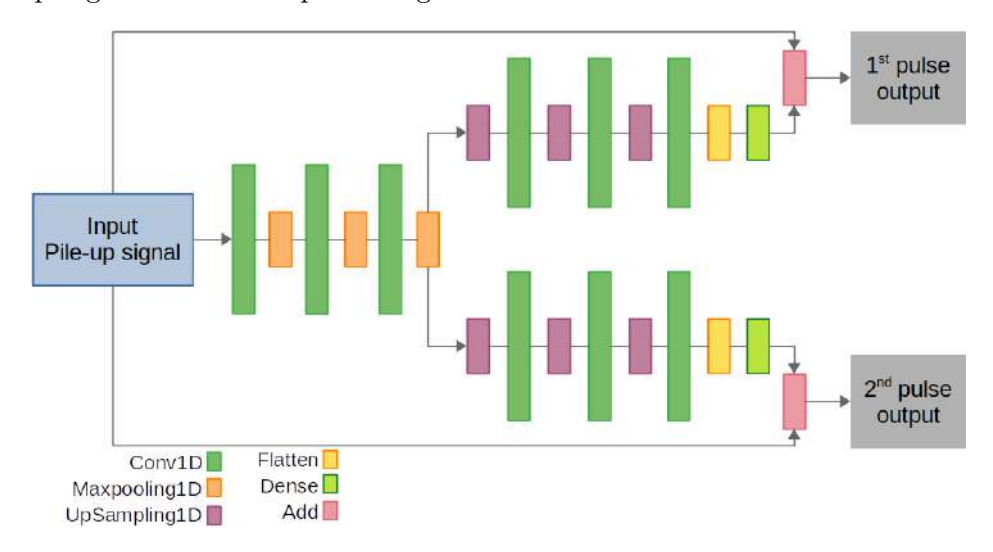


Figure 7.3: 1D-CAE architecture for NEDA pile-up event reconstruction.

The proposed design, shown in Fig. 7.3, is based on the usual autoencoder but with modifications. The architecture begins with a series of One-Dimensional Convolutional (Conv1D) [93] layers with ReLU [94] activation functions, followed by MaxPooling1D [95] layers to progressively reduce the dimensionality and extract features from the input signal. This process encodes the input into a compressed representation stored, called a feature map.

In the decoding phase, the model branches into two separate paths that upsample and process the compressed representation. Each branch undergoes several layers of UpSampling1D [96] and Conv1D to reconstruct the signal towards its original form.

Subsequently, the branches are connected to two Flatten [97] layers and then to Dense [98] layers with a ReLU as an activation function. Later, they combine the processed signal with the original input using an Add [99] layer. This layer is a skip connection to add the values with the input. The skip connection enables the direct flow of information from input to output layers, allowing the network to access the raw, unprocessed information. Finally, the model outputs two separate results.

This structure allows the model to capture and reconstruct complex patterns from the input signal while providing two distinct output signals. The complete design is available in detail in the following repository:

https://github.com/jmdeltoro/pile-up\_reconstruction\_NEDA

### Training

Autoencoders are generally used in an unsupervised learning context. In this case, supervised learning is used since the expected outputs are not signals similar to the input. The goal is to obtain one pulse as one of the outputs and another pulse as the other output. Therefore, the input signals for training are the artificial pile-up signals created from signals acquired with NEDA cells. The expected output signals (ground truth) are the two signals used to generate the artificial input pile-up signal. The process of data acquisition and the creation of the artificial pile-up signals is detailed in the following section.

# 7.4 Dataset preparation

The artificial pile-up signals (neutron-gamma and gamma-neutron combinations) for training and testing have been generated following the following steps:

- 1. Acquiring data from NEDA detectors.
- 2. Selecting and taking signals without pile-up.
- 3. Removing baseline of the signals. This aids in pulse analysis and allows acquired pulses from different channels to be summed.
- 4. Analyse them to determine what type of signal they are (gamma ray or neutron) using the CC method.
- 5. Take two signals of different types.
- 6. One of them is delayed between 3 and 40 samples.
- 7. Finally, they are added together, generating the final pile-up signal.

By performing these steps, a dataset with artificial pile-up signals has been created in which the origin of the signals composing the pile-up signal is known. Thus, pile-up signals with neutron-gamma and gamma-neutron combinations are obtained.

#### 7.4.1 Data acquisition

The data employed in this study was acquired during an on-beam experiment carried out at the Heavy Ion Laboratory (HIL) at the University of Warsaw, Poland. Nine NEDA detectors were placed 450 mm from the target centre at the 78-degree ring (theta angle measured with respect to the beam direction) of the EAGLE array [100]. Neutrons and gamma rays acquired in NEDA detectors were produced by a 171 MeV  $^{32}S$  beam impinging on a 0.75 mg/cm²  $^{148}\mathrm{Sm}$  target.

Signals from the NEDA detectors were independently read out by a Caen V1725SB digitiser (250 MHz, 14-bit) whenever a CFD threshold (implemented in FPGA) was exceeded. Linear FIFO modules limited the digitiser against too large signals (beyond the Vpp range). The CoMPASS software by CAEN, installed on a Centos07 server, was used to read the digitiser via optical fibre.

#### 7.4.2 Analysis and dataset generation

After data acquisition, the events were filtered to select only those signals without pile-up. Then, a classification was performed to differentiate between gamma ray and neutron signals. In typical NEDA experiments, the offline analysis uses information derived from the TOF and CC ratio. However, the TOF information was unavailable in our case, so the NGD depended only on the CC ratio.

The CC method in NEDA is employed to distinguish between neutron and gamma ray signals by analysing the shape of their respective pulses. After applying the CC to all the collected signals, they were categorised by particle type: gamma ray if the CC ratio was less than 0.525 and neutron if the result was greater, as depicted in Fig 7.4.

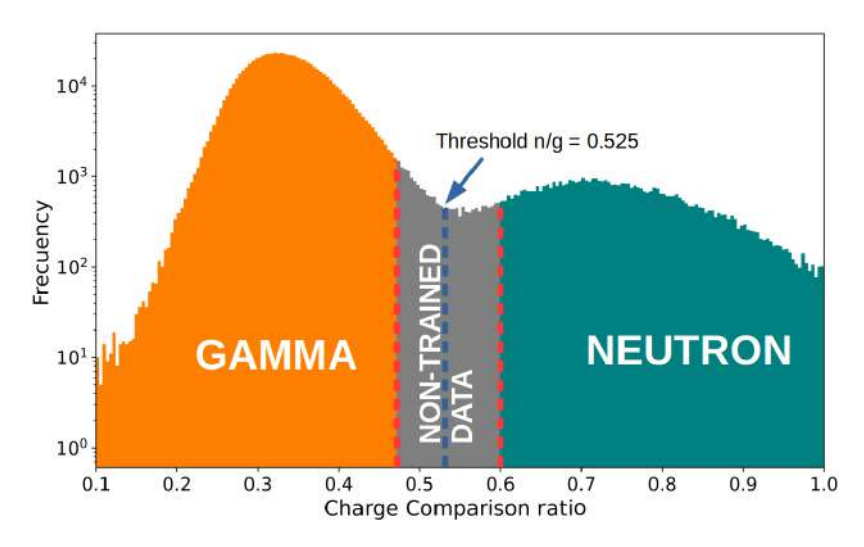


Figure 7.4: Included and excluded events for training.

The CC threshold was determined by identifying the lowest point in the valley between the gamma ray and neutron groups. However, there might be neutrons with CC values below the threshold and gamma rays with values above it. A more comprehensive analysis of the events would also need information from the TOF. Since the TOF information was unavailable, the events closest to the threshold (neutron-gamma discrimination value) were not used to train the 1D-CAE. As shown in Fig 7.4, events with a CC ratio between 0.475 and 0.6 were excluded. Therefore, events where the CC ratio is a value close to 0.525 were discarded for training. However, for the test dataset, events between 0.475 and 0.6 were not excluded for creating artificial pile-up signals. This is because, during the experiments, pulses with unknown CC ratio may form pile-up signals, and the values could be between 0.475 and 0.6.

After the classification, a signal of each type was selected, and one was shifted between 3 and 40 samples. In the Caen V1725SB digitiser context, each sample is equivalent to 4 ns, meaning that one of the two signals was shifted between 12 and 160 ns. Finally, both signals were summed to create an accumulation signal, as shown in Fig. 7.1.

Following this process, training and testing datasets were created, each containing an equal number of events. Each dataset included 10,000 events generated with each delay, resulting in 380,000 neutron-gamma and 380,000 gamma-neutron combinations (760,000 events in each dataset). Additionally, the events varied in amplitude from 150 to 7000 ADC counts, or from 18 to 855 mV, to reconstruct pile-up events across the entire amplitude range of the acquisition. The training dataset was utilised to train the 1D-CAE model, while the test dataset was used to evaluate the model with unknown pile-up signals. The outcomes of these tests are presented next.

### 7.5 Analysis of reconstructed signals

After the 1D-CAE model was trained, it was tested using the test dataset, which consisted of signals unknown to the system. The reconstructed pulses were then evaluated by comparing them with the original pulses. Factors considered for evaluation included the neutron or gamma ray pulse, the distance between pulse peaks, and the two possible combinations (gamma-neutron and neutron-gamma). Pile-up signals from the test data set were input to the 1D-CAE model, resulting in the reconstruction of the two pulses that composed each input pile-up signal. Subsequently, a CC analysis was performed on these reconstructed pulses. An example of the reconstruction of pulses from pile-up signals is shown in Figure 7.5.

As mentioned in Section 3, discriminating between neutrons and gamma rays is crucial, and the CC method was employed for this purpose. This analysis aims to confirm that the expected particle type was achieved after reconstructing a pile-up event.

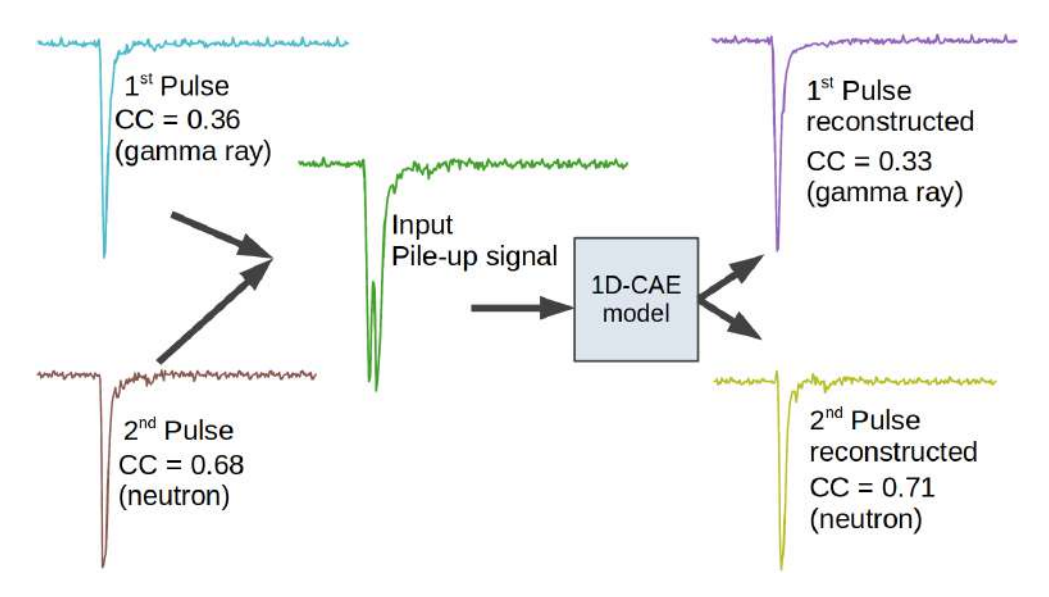
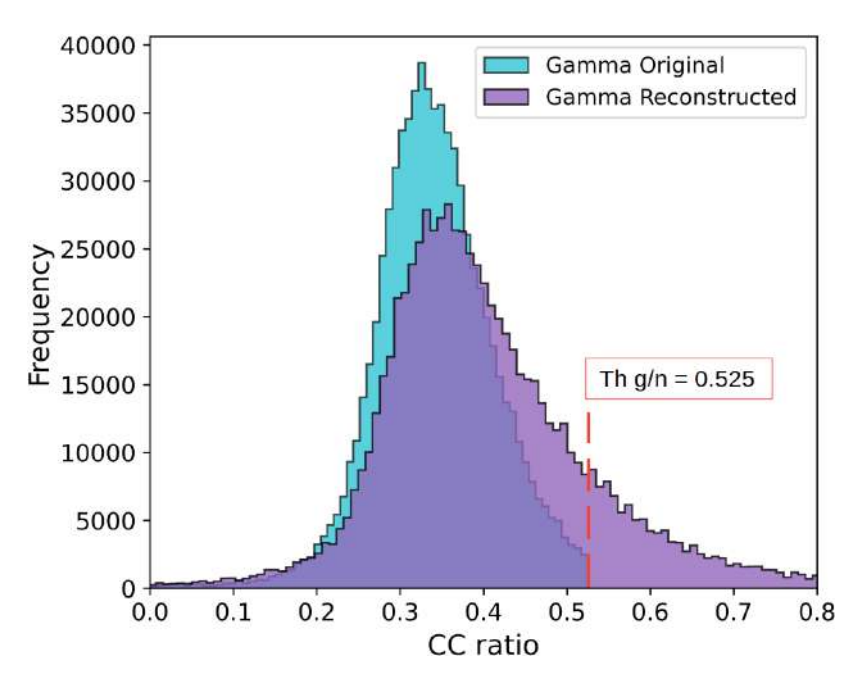


Figure 7.5: Example of pile-up reconstruction.



**Figure 7.6:** Distribution of CC ratio for the original gamma rays (without pile-up) and reconstructed gamma rays from pile-up events.

In the context of gamma rays, a successful reconstruction was considered when the CC ratio of the reconstructed pulse was lower than the neutron-gamma discrimination threshold (0.525). Figure 7.6 displays the distribution of the CC ratio of original gamma rays (blue) and the distribution of the

CC ratio of reconstructed gamma rays (purple). Upon comparing the two distributions, we found a mean value for the CC ratio of the original gamma rays of 0.34, while for the reconstructed gamma rays, it is 0.40. For the standard deviation, we obtain 0.072 for original gamma rays and 0.15 for reconstructed ones. In terms of the number of pulses correctly identified, we found that 84.7% of the pulses that would originally (without pile-up) be classified as gamma rays would also be classified as gamma rays if present in a pile-up event.

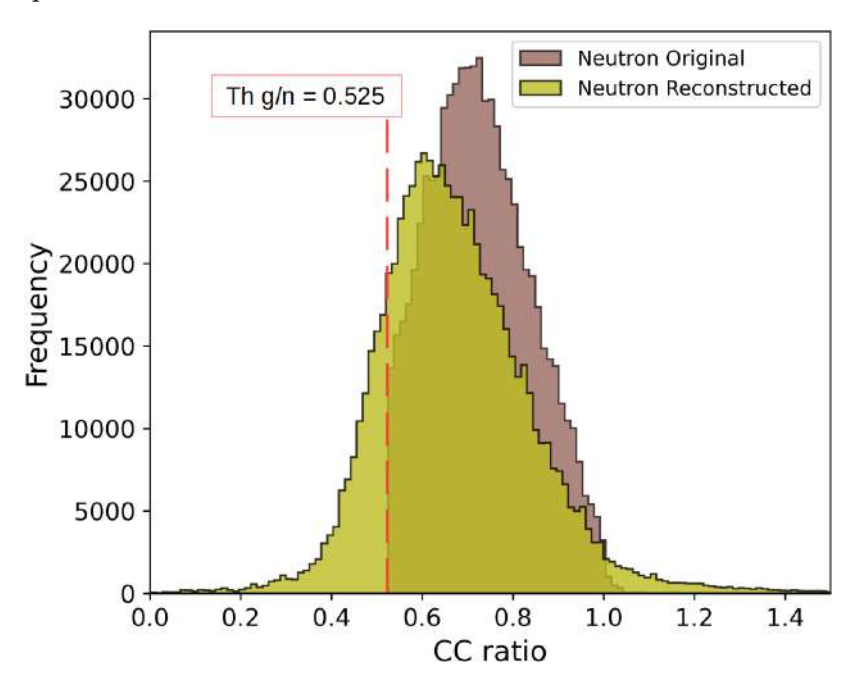


Figure 7.7: Distribution of CC ratio for the original neutrons (without pile-up) and reconstructed neutrons from pile-up events.

For neutron reconstruction, if the CC ratio of the reconstructed signal was lower than the neutron-gamma distribution threshold value (0.525), the event was considered a successful gamma ray. Figure 7.7 illustrates the CC distribution of the original neutrons (brown) and the CC distribution of the reconstructed neutrons (green). In this case, the mean values for the original and reconstructed neutron events are 0.73 and 0.67, respectively. For the standard deviation, we have 0.112 for the original neutrons and 0.181 for the ones after reconstruction. Again, the number of correctly identified neutrons after reconstruction is 83.3%.

As mentioned, neutron-gamma and gamma-neutron are particle combinations that can lead to pile-up events. These combinations can occur with different distances between pulses. Therefore, the results were analysed more deeply considering the type of pile-up combination and the distance between pulses.

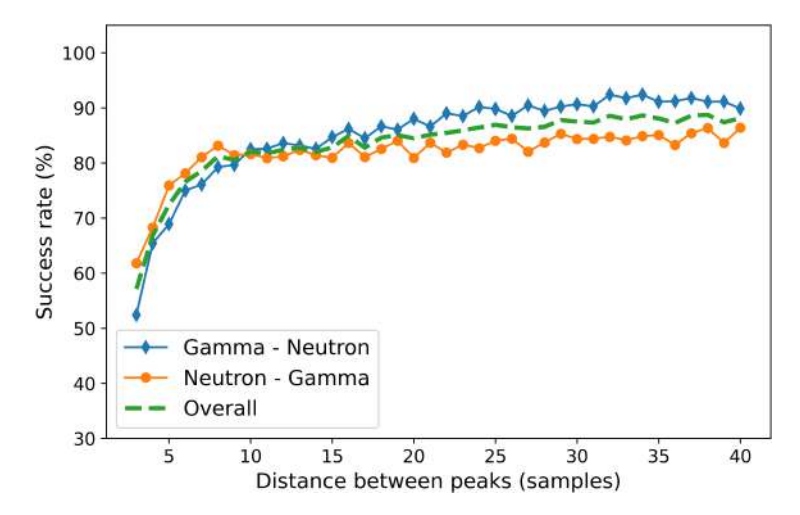


Figure 7.8: Percentage of success by distance between peaks.

On one side, the success rate was studied after obtaining the result of CC of each reconstructed pulse for each distance between pulses and both combinations. An 85.28% success rate was obtained for the gamma-neutron combination and an 82.61% success rate for the neutron-gamma combination. On average, 83.95% of the pulses were reconstructed correctly, obtaining the same type of particle as the original events without pile-up.

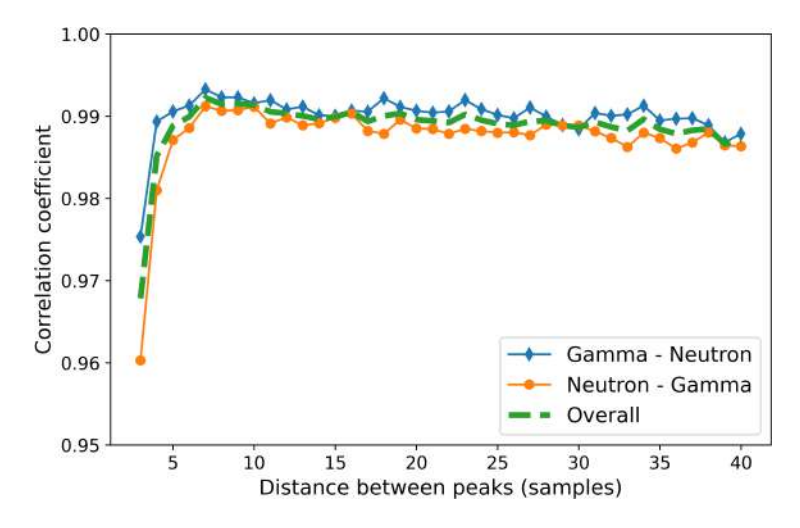


Figure 7.9: Average correlation per delay.

On the other side, we also analysed the correlation factor of the reconstructed signal shapes compared to the original signals. The mean correlation obtained was 0.988. Figure 7.9 shows the average correlation for each combination and each distance between pulses, obtaining a mean p-value of  $6.76 \times 10^{-15}$ .

#### 7.6 Conclusions and future work

To summarise, this study presents a robust solution to the prevalent issue of pulse pile-up in nuclear spectroscopy, with a primary focus on signals acquired in NEDA experiments. The novel method this research introduces employs a 1D-CAE architecture, which consist on an autoencoder with two outputs to reconstruct the two pile-up pulses effectively.

The evaluation of this method reveals a high success rate of 83.95% in accurately reconstructing pile-up events, thereby demonstrating its efficacy in preserving crucial information. This implies that pile-up events previously rejected in NEDA can now be reconstructed and incorporated into the analysis process. Notably, the reconstructed signals exhibit a high average correlation of 0.988 compared to the original signals, and a low p-value of  $6.76 \times 10^{-15}$ .

To tackle the pile-up issue, the inherent limitations in NEDA events have been considered, such as the necessity for a time difference of 15 ns or more between pulses and the demand for low computational complexity. Consequently, this method provides a practical and efficient solution for real-time signal processing in future enhancements of NEDA electronics. This research not only offers a technical solution to the challenging problem of pulse pile-up but also underscores the potential of the proposed 1D-CAE method as a practical tool for enhancing the precision and efficiency of nuclear spectroscopy experiments, particularly those involving NEDA detectors.

### Chapter 8

### Conclusions

In this thesis, several advances in the Neutron Detector Array (NEDA) were successfully implemented to improve its data acquisition and analysis capabilities in the context of gamma ray spectroscopy. Although in each chapter of the thesis the conclusions was obtained separately, the main achievements and conclusions are summarised below.

- Lossless online data compression: The Differential coding with fixed number of bits method was implemented, achieving a compression ratio of 1.6 and saving 37.5% of storage space. This allows a significant increase in the counting rate without exceeding the maximum transmission rate of 409.6 MB/s. Despite not being fully optimised due to DMA limitations, the compression and decompression of event traces were successfully demonstrated.
- Double trigger condition system: A double trigger condition system was developed, combining Charge Comparison (CC) and Time-Of-Flight (TOF) measurements to effectively discriminate between gamma rays and neutrons. Four trigger modes (CC, TOF, AND, and OR) were evaluated using data from the E703 experiment at GANIL. The AND mode is useful for reducing the trigger requests, while the OR mode minimises neutron loss when higher trigger request rates are manageable. These trigger modes offer greater versatility to adapt the detection system to the specific experimental goals.
- Pulse pile-up reconstruction: A novel method using a one dimensional convolutional autoencoder (1D-CAE) was implemented to reconstruct pile-up events, showing an 83.95% success rate in accurately reconstructing these events. This method preserves crucial information previously lost in pile-up events and maintains a high average correlation of 0.988 with the original signals. It offers a practical solution for real-time signal processing in future NEDA upgrades.

Overall, this thesis allows to enhance NEDA's data acquisition and analysis capabilities, enabling more precise and efficient nuclear spectroscopy and reaction studies. The advancements in data compression, the double trigger condition system, and pulse pile-up reconstruction collectively optimise NEDA's performance, positioning it as a powerful tool for future nuclear physics research.

# List of Figures

2.1	Table of nuclides with the stable elements in black and for the other nuclides the colour indicates the type of decay (or radiation) happening in the unstable nuclei, i.e. red: $\beta$ +, blue: $\beta$ -, orange: proton-decay, yellow: $\alpha$ -decay, purple: neutron-emitters	7
2.2	Comparison of the <sup>60</sup> Co gamma spectrum between HP-Ge (blue) and NaI (red) [19]	9
2.3	Attenuation coefficients for gamma ray in relation with atomic number Z of absorbed material [21]	11
3.1	The design of a single NEDA neutron detector cell [8]	13
3.2	The NEutron Detector Array coupled to the Neutron Wall at	
	$90^{o} [30].$	14
3.3	Scintillator coupled to a photomultiplier	15
3.4	Graphic representation of the delocalisation of electrons in ben-	
	zene. [32]	16
3.5	Energy level diagram of an organic molecule with $\pi$ -electron structure, adapted from [33]. The singlet states with spin 0 are labelled $S_{ab}$ and the triplet states of spin 1 are labelled $T_{ab}$ where a indicates the excitation level and $b$ indicates the vibrational state of that level	17
3.6		18
3.7	Average waveform from <sup>252</sup> Cf for neutrons and gammas in a hydrocarbon-based plastic, normalised to the same electron-	19
3.8	Pulse-shape discrimination based on the charge comparison method [38] measured with a NEDA detector using a $^{252}$ Cf source. The ratio of the light in the slow component of the digitised signal divided by the total light is shown on the y axis as a function	
3.9	Measured Time-of-Flight distribution of pulses. The inset shows	
	•	20

	(a) NUMEXO2 digitiser + Neutron Wall. (b) Neutron Wall (blue) + NEDA (green) + AGATA (multi-color). (c) 355 NEDA detectors
	Schematic picture and measures of the NEDA detector cell 22
	Scintillator coupled to a photomultiplier tube (PMT) 23
3.14	General scheme of NEDA electronics with single detector 23
4.1	Frontal and general view of NUMEXO2
4.2	Block diagram of NUMEXO2 digitiser
4.3	Top and bottom view of the hardware of the FADC Mezzanine. 2
4.4	Block diagram of single mezzanine [42]
4.5	Block diagram of Virtex-6 firmware
4.6	ISERDES hardware block diagram
4.7	Digital signal processing for a single channel and interaction with the global readout. Blocks in blue refer to local processing, while orange refers to the readout system clocked by the global
	clock
4.8	General block diagram of the capture event to transmit data
	between Virtex-6 and Virtex-5
4.9	General block diagram of the capture event to transmit data
	between Virtex-6 and Virtex-5
4.10	Virtex-5 block diagram. Courtesy of GANIL
5.1	Resources used in the FPGA without compression method included
T 0	
5.2	Example one event compressed where X is smaller than 128 39
5.3	Example Run-Length Encoding
5.4	Example Huffman tree
5.5	Example Huffman tree for NEDA event
5.6	Schema Differential coding with variable number of bits where
	X, Z, and Y are less than or equal to 16
5.7	Example of Differential coding with variable number of bits in
	the first samples in a real trace
5.8	Example of Differential coding with fixed number of bits 48
5.9	Baseline noise of 6.5 mVpp in a data acquisition at HIL 46
5.10	Number of bits required for the difference between consecutive
	samples
	Number of bits required for the difference with the first sample. 4
	Outline of the basic concept of data compression 48
5.13	Compression blocks location and new design inside the Capture
	Single Channel block
5.14	Differences FSM performs the calculation of the difference be-
	tween current samples and the reference sample (second sample). 50

5.15	Example of initial cycles of Differences FSM 5
5.16	Control FSM controls the compression and non-compression
	sections
5.17	Joining FSM performs the merging of two consecutive samples (even and odd)
5.18	Example of initial cycles of Joining FSM 5
5.19	First cycles of all state machines
5.20	Table of resources needed by adding the 3 compression blocks per channel
5.21	Chain acquisition
5.22	Acquisition with shifted events in decompression 5
5.23	Comparison between compressed and uncompressed event 5
5.24	Decompressed gamma ray signals with a constant rate of 10 kHz and noise of 6.5 mV
5.25	Decompressed signals neutron and gamma rays a constant rate of 10 kHz and noise of 9.7 mV
5.26	Decompressed signals neutron and gamma rays a constant rate of 10 kHz and noise of 19.5 mV
6.1	The black area encloses the neutrons, the red one the prompt gamma rays, and the yellow one the uncorrelated gamma rays.
6.2	Slow and fast components of neutron and gamma-ray signals $$ 6
6.3	Acquisition using CC as trigger 6
6.4	Schematic view of the TOF measurement concept for in-beam studies
6.5	NUMEXO2 Virtex6 firmware blocks diagram including the newly implemented Double Trigger block (green box) and the TDC Trigger block (purple box). See text for details 6
6.6	Test bench for the double trigger functional test 6
6.7	Functional test using the four trigger modes, and acquisition without trigger condition
6.8	NEDA + AGATA + Neutron Wall + DIAMANT structure. 6
6.9	Events accepted after offline analysis without condition trigger and the four trigger modes with CC threshold in 0.19. Some events exceed the thresholds established at the firmware level due to the more accurate offline pulse shape analysis
6.10	Total events by trigger mode and total events without trigger condition
6.11	Percentage of particles acquired compared to acquisition without trigger condition, taking into account the different trigger modes

6.12	Percentage of particles acquired compared to acquisition with-	
	out trigger condition. For the figure on the left a CC threshold	
	of 0.19 was used and for the one on the right 0.3	73
7.1	Example of a signal with pulse pile-up effect	76
7.2	Current status reject the pile-up signals. The objective of this	
	work is the development of a method for reconstructing pile-up	
	signals before Offline Analysis. In the future it will be included	
	in online signal processing	77
7.3	1D-CAE architecture for NEDA pile-up event reconstruction	81
7.4	Included and excluded events for training	83
7.5	Example of pile-up reconstruction	85
7.6	Distribution of CC ratio for the original gamma rays (without	
	pile-up) and reconstructed gamma rays from pile-up events	85
7.7	Distribution of CC ratio for the original neutrons (without pile-	
	up) and reconstructed neutrons from pile-up events	86
7.8	Percentage of success by distance between peaks	87
7.9	Average correlation per delay	87

### Abbreviations

AGATA Advanced GAmma Tracking Array

ASIC Application-Specific Integrated Circuit

**BUFG** Global clock BUFfer

**BW** BandWidth

**CC** Charge Comparison

CERN Conseil Européen pour la Recherche Nucléaire

**CFD** Constant Fraction Discrimination

CNN Convolutional Neural Network

**DCFD** Digital Constant Fraction Discriminator

**DMA** Direct Memory Access

**DPCM** Differential Pulse-Code Modulation

**DSP** Digital Signal Processing

**EMA** Exponential Moving Average

FADC Fast Analog/Digital Converter

**FIFO** First In First Out

**FPGA** Field-Programmable Gate Array

FSM Finite State Machine

GANIL Grand Accélérateur National d'Ions Lourds

**GAP** Group d'Acquisition pour la Physique

**GTS** Global Trigger and Synchronization

**HDMI** High-Definition Multimedia Interface

**HIL** Heavy Ion Laboratory

**HPGe** High-purity Germanium

**IP** Internet Protocol

**ISERDES** Input Serialisation/Descrialisation

**LUT** Look Up Tables

**NEDA** Neutron Detector Array

NGD neutron/gamma discrimination

**NIM** Nuclear Instrumentation Module

NUMEXO2 NUMériseur pour EXOgam2

1D-CAE One-Dimensional Convolutional Autoencoder

1D-CNN One-Dimensional Convolutional Neural Network

**PET** Positron Emission Tomography

PM PhotoMultipliers

**PMT** PhotoMultiplier Tubes

**PPC** Power PC

PSD Pulse Shape Discrimination

**PSA** Pulse Shape Analysis

**RLE** Run-Length Encoding

 ${\bf SPI}\,$  Serial Peripheral Interface

 ${\bf SEDIFF} \ \ {\bf Single-Ended} \ \ {\bf to} \ \ {\bf DIFFerential}$ 

TCP Transmission Control Protocol

**TDC** Time to Digital Converter

**TOF** Time-Of-Flight

**ZCO** Zero Cross Over

## Bibliography

- [1] G. de Angelis, A. Bracco, and D. Curien, "The euroball gamma ray detector array," *Europhysics News*, vol. 34, pp. 181–185, 9 2003. [Online]. Available: https://www.europhysicsnews.org/articles/epn/abs/2003/05/epn03503/epn03503.html
- [2] F. S. Goulding, D. A. Landis, N. Madden, and et al., "Gammasphere overview of detector and signal processing system," *IEEE Nuclear Sci*ence Symposium Medical Imaging Conference, vol. 1, pp. 432–436, 1995.
- [3] J. Eberth, G. Pascovici, H. G. Thomas, and et al., "Miniball: A gamma-ray spectrometer with position-sensitive ge detectors for nuclear structure studies at rex-isolde," *AIP Conference Proceedings*, vol. 656, pp. 349–356, 3 2003. [Online]. Available: /aip/acp/article/656/1/349/1013565/Miniball-A-Gamma-Ray-Spectrometer-With-Position
- [4] J. Simpson, F. Azaiez, G. de France, G. Fouan, J. Gerl, R. Julin, W. Korten, P. Nolan, B. Nyako, G. Sletten, and P. Walker, "The EXOGAM array: A radioactive beam gamma-ray spectrometer," Acta Physica Hungarica New Series-Heavy ion, vol. 11, pp. 159–188, 2000. [Online]. Available: https://hal.in2p3.fr/in2p3-00438782
- [5] S. Akkoyun, A. Algora, B. Alikhani, and et al., "Agata—advanced gamma tracking array," Nuclear Instruments and Methods in Physics Research Section A: Accelerators, Spectrometers, Detectors and Associated Equipment, vol. 668, pp. 26–58, 3 2012.
- [6] C. W. Beausang, "Greta: the gamma-ray energy-tracking array, status of the development and physics opportunities," Nuclear Instruments and Methods in Physics Research Section B: Beam Interactions with Materials and Atoms, vol. 204, pp. 666–670, 5 2003.
- [7] J. Nyberg. (2008, 5) Neutron wall. [Online]. Available: http://egp-workshop.in2p3.fr/docs/Talks-Mardi/nwall-jn.pdf
- [8] J. J. Valiente-Dobón, G. Jaworski, A. Goasduff, and et al., "Neda—neutron detector array," Nuclear Instruments and Methods in

- Physics Research Section A: Accelerators, Spectrometers, Detectors and Associated Equipment, vol. 927, pp. 81–86, 5 2019.
- [9] D. Mengoni, "Status of the trace array," in SPES Workshop, 2010.
   [Online]. Available: https://agenda.infn.it/event/2660/contributions/41933/attachments/29391/34611/5-Mengoni.pdf
- [10] B. M. Nyakó. (2007) The diamant light-charged particle detector: Performance and plans for improvements. [Online]. Available: https://www.osti.gov/etdeweb/servlets/purl/21016782
- [11] O. Glasser, Wilhelm Conrad Röntgen and the early history of the Roentgen rays. Norman Publishing, 1993, no. 1.
- [12] H. F. Walton, "The curie-becquerel story," Journal of chemical education, vol. 69, no. 1, p. 10, 1992.
- [13] K. S. Krane, "Gamma decay," Introductory Nuclear Physics. John Wiley & Sons Inc, New York, 1988.
- [14] G. F. Knoll, Radiation detection and measurement. John Wiley & Sons, 2010.
- [15] D. S. Ahn, N. Fukuda, H. Geissel, and et al., "Location of the neutron dripline at fluorine and neon," *Phys. Rev. Lett.*, vol. 123, p. 212501, Nov 2019. [Online]. Available: https://link.aps.org/doi/10. 1103/PhysRevLett.123.212501
- [16] W. Leo, Techniques for Nuclear and Particle Physics Experiments: A How-to Approach. Springer, 1994. [Online]. Available: https://books.google.es/books?id=W7vHQgAACAAJ
- [17] J. Eberth and J. Simpson, "From ge(li) detectors to gamma-ray tracking arrays—50 years of gamma spectroscopy with germanium detectors," *Progress in Particle and Nuclear Physics*, vol. 60, pp. 283—337, 4 2008.
- [18] L. J. Meng, D. Ramsden, V. M. Chirkin, and et al., "The design and performance of a large-volume spherical csi(tl) scintillation counter for gamma-ray spectroscopy," Nuclear Instruments and Methods in Physics Research Section A: Accelerators, Spectrometers, Detectors and Associated Equipment, vol. 485, pp. 468–476, 6 2002.
- [19] (2023, 9) Universitetet i oslo nukwik. [Online]. Available: https://wiki.uio.no/mn/safe/nukwik/index.php/Gamma\\_Spectroscopy\\_and\\_Detectors

- [20] F. C. Crespi, V. Vandone, S. Brambilla, and et al., "Hpge detectors timing using pulse shape analysis techniques," Nuclear Instruments and Methods in Physics Research Section A: Accelerators, Spectrometers, Detectors and Associated Equipment, vol. 620, pp. 299–304, 8 2010.
- [21] (2023, 11) Attenuation coefficients. [Online]. Available: https://www.nuclear-power.com/nuclear-power/reactor-physics/interaction-radiation-matter/interaction-gamma-radiation-matter/gamma-ray-attenuation/
- [22] T. Crane and M. Baker, "Neutron detectors," *Passive Nondestructive Assay of Nuclear Materials*, vol. 13, pp. 1–28, 1991.
- [23] P. Rinard *et al.*, "Neutron interactions with matter," *Passive nonde-structive assay of nuclear materials*, no. 375-377, 1991.
- [24] G. Jaworski, M. Palacz, J. Nyberg, and et al., "Monte carlo simulation of a single detector unit for the neutron detector array neda," Nuclear Instruments and Methods in Physics Research Section A: Accelerators, Spectrometers, Detectors and Associated Equipment, vol. 673, pp. 64–72, 5 2012.
- [25] J. Valiente-Dobón, D. Mengoni, F. Recchia, and et al., "Status of the gamma-ray spectrometer galileo," *Annual Report*, pp. 95–96, 2014.
- [26] M. J. Borge Jonson, "Isolde and В. past, and present **Journal** future," of*Physics* G: Nuclear andParticlePhysics, vol. 44. p. 044011, 3 2017. [Online]. Available: https://iopscience.iop.org/article/10.1088/1361-6471/aa5f03https: //iopscience.iop.org/article/10.1088/1361-6471/aa5f03/meta
- [27] G. Pretea, A. Andrighetto, M. Manzolaro, and et al., "The spes project at the infn- laboratori nazionali di legnaro," *EPJ Web of Conferences*, vol. 66, p. 11030, 2014. [Online]. Available: https://www.epj-conferences.org/articles/epjconf/abs/2014/03/epjconf\_inpc2013\_11030/epjconf\_inpc2013\_11030.html
- [28] S. Gales, "Spiral2 at ganil: Next generation of isol facility for intense secondary radioactive ion beams," *Nuclear Physics A*, vol. 834, pp. 717c–723c, 3 2010.
- [29] T. and Υ. A. Litvinov, "Status of the fair facildarmstadt," of Physics: ConferenceJournalSeries, 1685, 012020,11 2020.[Online]. Available: https: //iopscience.iop.org/article/10.1088/1742-6596/1685/1/012020https: //iopscience.iop.org/article/10.1088/1742-6596/1685/1/012020/meta

- [30] M. de la Luz Jurado Gómez, "Nuclear structure studies on quadrupole and octupole correlations in the vicinity of heavy n=z nuclei with agata and neda," Ph.D. dissertation, 2022.
- [31] D. G. Sarantites, W. Reviol, C. J. Chiara, and et al., ""neutron shell": a high efficiency array of neutron detectors for -ray spectroscopic studies with gammasphere," Nuclear Instruments and Methods in Physics Research Section A: Accelerators, Spectrometers, Detectors and Associated Equipment, vol. 530, pp. 473–492, 9 2004.
- [32] A. L. Chemistry. (2023, 10) Aromatic compounds. [Online]. Available: https://alevelchemistry.co.uk/notes/aromatic-compounds/
- [33] G. F. Knoll, Radiation detection and measurement, Fourth Edition, Chapter 8, Page 225. John Wiley & Sons, 2010.
- [34] A. G. Wright, *The photomultiplier handbook*. Oxford University Press, 2017.
- [35] R. Pestotnik, S. Korpar, H. Chagani, and et al., "Silicon photomultipliers as photon detectors for pet," *Nuclear Instruments and Methods in Physics Research Section A: Accelerators, Spectrometers, Detectors and Associated Equipment*, vol. 623, pp. 594–596, 11 2010.
- [36] V. Modamio, J. J. Valiente-Dobón, G. Jaworski, and et al., "Digital pulse-timing technique for the neutron detector array neda," Nuclear Instruments and Methods in Physics Research Section A: Accelerators, Spectrometers, Detectors and Associated Equipment, vol. 775, pp. 71–76, 3 2015.
- [37] X. L. Luo, V. Modamio, J. Nyberg, and et al., "Test of digital neutron–gamma discrimination with four different photomultiplier tubes for the neutron detector array (neda)," Nuclear Instruments and Methods in Physics Research Section A: Accelerators, Spectrometers, Detectors and Associated Equipment, vol. 767, pp. 83–91, 12 2014.
- [38] P. A. Söderström, J. Nyberg, and R. Wolters, "Digital pulse-shape discrimination of fast neutrons and rays," *Nuclear Instruments and Methods in Physics Research Section A: Accelerators, Spectrometers, Detectors and Associated Equipment*, vol. 594, pp. 79–89, 8 2008.
- [39] T. Hüyük, "The next generation nuclear instruments: agata and neda, and nuclear structure studies near n=z line," Ph.D. dissertation, 2017.
- [40] F. J. Canet, C. Houarner, A. Boujrad, and et al., "Digital front-end electronics for the neutron detector neda," *IEEE Transactions on Nuclear Science*, vol. 62, pp. 1063–1069, 6 2015.

- [41] J. M. Deltoro, F. J. Egea, P. Cocconi, and et al., A Single-ended to Differential Converter for the Neutron Detector NEDA, 2017. [Online]. Available: URL:http://www.lnl.infn.it/~annrep
- [42] X. Egea, E. Sanchis, V. Gonzalez, and et al., "Design and test of a high-speed flash add mezzanine card for high-resolution and timing performance in nuclear structure experiments," 2012 18th IEEE-NPSS Real Time Conference, RT 2012, 2012.
- [43] A. Triossi, D. Barrientos. Μ. Bellato, al., "A and et optical link based on low-cost transceivers qualexpress radiation hardness," ified for **Journal** ofInstrumentation, vol. 8. p. C02011. 2 2013. [Online]. Available: https: //iopscience.iop.org/article/10.1088/1748-0221/8/02/C02011https: //iopscience.iop.org/article/10.1088/1748-0221/8/02/C02011/meta
- [44] M. J. and et Bellato. D. Bortolato. Chavas. al.. "Subnanosecond clock synchronization and trigger management the nuclear physics experiment agata," Journal of Instrumentation, vol. 8, p. P07003, 7 2013. [Online]. Available: //iopscience.iop.org/article/10.1088/1748-0221/8/07/P07003https: //iopscience.iop.org/article/10.1088/1748-0221/8/07/P07003/meta
- [45] J. E. Canet, "Design, verification and integration of a fast digitizer for nuclear structure experiments. application to exogam and neda detectors," Ph.D. dissertation, Universitat de Valencia, 2015.
- [46] U. Jayasankar, V. Thirumal, and D. Ponnurangam, "A survey on data compression techniques: From the perspective of data quality, coding schemes, data type and applications," *Journal of King Saud University Computer and Information Sciences*, vol. 33, pp. 119–140, 2 2021.
- [47] K. Sayood, Introduction. Morgan Kaufmann, 1 2018, pp. 1–10.
- [48] G. K. Wallace, "The jpeg still picture compression standard," *IEEE Transactions on Consumer Electronics*, vol. 38, pp. xviii–xxxiv, 1992.
- [49] D. Huffman, "A method for the construction of minimum-redundancy codes," *Proceedings of the IRE*, vol. 40, pp. 1098–1101, 9 1952.
- [50] H. D. Kotha, M. Tummanapally, and V. K. Upadhyay, "Review on lossless compression techniques," *Journal of Physics: Conference Series*, vol. 1228, p. 012007, 5 2019. [Online]. Available: https://iopscience.iop.org/article/10.1088/1742-6596/1228/1/012007
- [51] A. H. Robinson and C. Cherry, "Results of a prototype television bandwidth compression scheme," *Proceedings of the IEEE*, vol. 55, pp. 356–364, 1967.

- [52] Y. Kondo, K. Kakuse, S. Saba, and et al., "United states patent (19) tsukiyama et al. (54) method and system for data compression and restoration 75) inventors: Tokuhiro tsukiyama, kanagawa," 4 1986.
- [53] Huffman coding calculator compression tree generator online. (Accessed on 19.06.2024). [Online]. Available: https://www.dcode.fr/huffman-tree-compression
- [54] J. Ziv and A. Lempel, "A universal algorithm for sequential data compression," *IEEE Transactions on Information Theory*, vol. 23, pp. 337–343, 1977.
- [55] —, "Compression of individual sequences via variable-rate coding," *IEEE Transactions on Information Theory*, vol. 24, pp. 530–536, 1978.
- [56] Welch, "A technique for high-performance data compression," *Computer*, vol. 17, no. 6, pp. 8–19, 1984.
- [57] D. Salomon, G. Motta, and G. Motta, *Relative Encoding*. Springer, 2010, vol. 2, pp. 351–378.
- [58] C. C. Cutler, "Differential quantization of communication signals," Patent, 1952, patent 2,605,361.
- [59] F. J. Egea, E. Sanchis, V. González, and et al., "Design and test of a high-speed flash adc mezzanine card for high-resolution and timing performance in nuclear structure experiments," *IEEE Transactions on Nuclear Science*, vol. 60, no. 5, pp. 3526–3531, 2013.
- [60] Dt5800 desktop digital detector emulator caen tools for discovery. [Online]. Available: https://www.caen.it/products/dt5800/
- [61] F. J. Egea Canet, C. Houarner, A. Boujrad, and et al., "Digital Front-End Electronics for the Neutron Detector NEDA," *IEEE Transactions* on Nuclear Science, vol. 62, no. 3, pp. 1063–1069, 2015.
- [62] M. Nakhostin, Signal processing for radiation detectors. John Wiley & Sons, 2017.
- [63] X. Fabian, G. Baulieu, L. Ducroux, and et al., "Artificial neural networks for neutron/ discrimination in the neutron detectors of neda," Nuclear Instruments and Methods in Physics Research Section A: Accelerators, Spectrometers, Detectors and Associated Equipment, vol. 986, p. 164750, 1 2021.
- [64] M. A. Nelson, B. D. Rooney, D. R. Dinwiddie, and et al., "Analysis of digital timing methods with baf2 scintillators," *Nuclear*

- Instruments and Methods in Physics Research Section A: Accelerators, Spectrometers, Detectors and Associated Equipment, vol. 505, no. 1, pp. 324–327, 2003, proceedings of the tenth Symposium on Radiation Measurements and Applications. [Online]. Available: https://www.sciencedirect.com/science/article/pii/S0168900203010787
- [65] Z. Gu, D. L. Prout, R. Taschereau, and et al., "A new pulse pileup rejection method based on position shift identification," *IEEE Transactions on Nuclear Science*, vol. 63, no. 1, pp. 22–29, 2016.
- [66] M. Capogni, A. Ceccatelli, P. D. Felice, and et al., "Random-summing correction and pile-up rejection in the sum-peak method," *Applied Ra*diation and Isotopes, vol. 64, pp. 1229–1233, 10 2006.
- [67] J. Yu, J. Zhou, Y. Liu, and et al., "Pile-up pulse continuous zone reject method," Applied Radiation and Isotopes, vol. 165, p. 109319, 2020. [Online]. Available: https://www.sciencedirect.com/science/article/pii/ S0969804320304693
- [68] V. T. Jordanov, "Pile-up rejection using pulse-shape discrimination." IEEE, 11 2018, pp. 1–4.
- [69] E. Ronchi, P.-A. Söderström, J. Nyberg, and et al., "An artificial neural network based neutron–gamma discrimination and pile-up rejection framework for the bc-501 liquid scintillation detector," Nuclear Instruments and Methods in Physics Research Section A: Accelerators, Spectrometers, Detectors and Associated Equipment, vol. 610, no. 2, pp. 534–539, 2009. [Online]. Available: https://www.sciencedirect.com/science/article/pii/S0168900209017045
- [70] P. Bastia, G. Bertuccio, F. Borghetti, and et al., "An integrated reset/pulse pile-up rejection circuit for pixel readout asics," *IEEE Transactions on Nuclear Science*, vol. 53, no. 1, pp. 414–417, 2006.
- [71] W. Guo, S. H. Lee, and R. P. Gardner, "The monte carlo approach mcput for correcting pile-up distorted pulse-height spectra," Nuclear Instruments and Methods in Physics Research Section A: Accelerators, Spectrometers, Detectors and Associated Equipment, vol. 531, pp. 520– 529, 10 2004.
- [72] L. Sabbatucci, V. Scot, and J. E. Fernandez, "Multi-shape pulse pile-up correction: The mcppu code," *Radiation Physics and Chemistry*, vol. 104, pp. 372–375, 11 2014.
- [73] M. R. Mohammadian-Behbahani and S. Saramad, "A comparison study of the pile-up correction algorithms," *Nuclear Instruments and Methods*

- in Physics Research Section A: Accelerators, Spectrometers, Detectors and Associated Equipment, vol. 951, p. 163013, 1 2020.
- [74] C. Yi, J. Han, R. Song, and et al., "Discrimination of piled-up neutron-gamma pulses using charge comparison method and neural network for clyc detectors," Nuclear Instruments and Methods in Physics Research Section A: Accelerators, Spectrometers, Detectors and Associated Equipment, vol. 1055, p. 168561, 10 2023.
- [75] I. Morad, M. Ghelman, D. Ginzburg, and et al., "Model-based deep learning algorithm for pulse shape discrimination in high event rates," *EPJ Web of Conferences*, vol. 288, p. 10001, 11 2023. [Online]. Available: https://www.epj-conferences.org/articles/epjconf/abs/2023/14/epjconf\_animma2023\_10001/epjconf\_animma2023\_10001.html
- [76] S. Peng, Z. Hua, Q. Wu, and et al., "Piled-up neutron-gamma discrimination system for cllb using convolutional neural network," *Journal of Instrumentation*, vol. 17, p. T08001, 8 2022.
- [77] S. Marrone, D. Cano-Ott, N. Colonna, and et al., "Pulse shape analysis of liquid scintillators for neutron studies," *Nuclear Instruments and Methods in Physics Research Section A: Accelerators, Spectrometers, Detectors and Associated Equipment*, vol. 490, pp. 299–307, 9 2002.
- [78] F. Belli, B. Esposito, D. Marocco, and et al., "A method for digital processing of pile-up events in organic scintillators," *Nuclear Instruments and Methods in Physics Research Section A: Accelerators, Spectrometers, Detectors and Associated Equipment*, vol. 595, pp. 512–519, 10 2008.
- [79] M. E. Hammad, H. Kasban, R. M. Fikry, and et al., "Pile-up correction algorithm for high count rate gamma ray spectroscopy," Applied Radiation and Isotopes, vol. 151, pp. 196–206, 9 2019.
- [80] W. Guo, R. P. Gardner, and C. W. Mayo, "A study of the real-time deconvolution of digitized waveforms with pulse pile up for digital radiation spectroscopy," Nuclear Instruments and Methods in Physics Research Section A: Accelerators, Spectrometers, Detectors and Associated Equipment, vol. 544, pp. 668–678, 6 2005.
- [81] X. L. Luo, V. Modamio, J. Nyberg, and et al., "Pulse pile-up identification and reconstruction for liquid scintillator based neutron detectors," Nuclear Instruments and Methods in Physics Research Section A: Accelerators, Spectrometers, Detectors and Associated Equipment, vol. 897, pp. 59–65, 7 2018.
- [82] C. Fu, A. D. Fulvio, S. D. Clarke, and et al., "Artificial neural network algorithms for pulse shape discrimination and recovery of piled-up pulses

- in organic scintillators," Annals of Nuclear Energy, vol. 120, pp. 410–421, 10 2018.
- [83] S. Kiranyaz, O. Avci, O. Abdeljaber, and et al., "1d convolutional neural networks and applications: A survey," *Mechanical Systems and Signal Processing*, vol. 151, p. 107398, 4 2021.
- [84] D. Bank, N. Koenigstein, and R. Giryes, Autoencoders. Springer, Cham, 2023, pp. 353–374. [Online]. Available: https://link.springer. com/chapter/10.1007/978-3-031-24628-9\_16
- [85] Z. Li, F. Liu, W. Yang, and et al., "A survey of convolutional neural networks: Analysis, applications, and prospects," *IEEE Transactions* on Neural Networks and Learning Systems, vol. 33, pp. 6999–7019, 12 2022.
- [86] U. Erdenebayar, H. Kim, J. U. Park, and et al., "Automatic prediction of atrial fibrillation based on convolutional neural network using a short-term normal electrocardiogram signal," *Journal of Korean medical science*, vol. 34, 2 2019. [Online]. Available: https://pubmed.ncbi.nlm.nih.gov/30804732/
- [87] S. Mehrkanoon, "Deep shared representation learning for weather elements forecasting," Knowledge-Based Systems, vol. 179, pp. 120–128, 9 2019.
- [88] L. Deng and X. Li, "Machine learning paradigms for speech recognition: An overview," *IEEE Transactions on Audio, Speech and Language Processing*, vol. 21, pp. 1060–1089, 2013.
- [89] P. Li, Y. Pei, and J. Li, "A comprehensive survey on design and application of autoencoder in deep learning," Applied Soft Computing, vol. 138, p. 110176, 5 2023.
- [90] R. Ranjan, V. M. Patel, and R. Chellappa, "Hyperface: A deep multitask learning framework for face detection, landmark localization, pose estimation, and gender recognition," *IEEE Transactions on Pattern* Analysis and Machine Intelligence, vol. 41, pp. 121–135, 1 2019.
- [91] D. P. Kingma and M. Welling, "Auto-encoding variational bayes," 2nd International Conference on Learning Representations, ICLR 2014 - Conference Track Proceedings, 12 2013. [Online]. Available: https://arxiv.org/abs/1312.6114v11
- [92] P. Vincent, H. Larochelle, Y. Bengio, and et al., "Extracting and composing robust features with denoising autoencoders."

- [93] Conv1d layer. (Accessed on 24.06.2024). [Online]. Available: https://keras.io/api/layers/convolution\_layers/convolution1d/
- [94] Rectifier (neural networks) wikipedia. (Accessed on 24.06.2024). [Online]. Available: https://en.wikipedia.org/wiki/Rectifier\_(neural\_networks)
- [95] Maxpooling1d layer. (Accessed on 24.06.2024). [Online]. Available: https://keras.io/api/layers/pooling\_layers/max\_pooling1d/
- [96] Upsampling1d layer. (Accessed on 24.06.2024). [Online]. Available: https://keras.io/api/layers/reshaping\_layers/up\_sampling1d/
- [97] Flatten layer. (Accessed on 24.06.2024). [Online]. Available: https://keras.io/api/layers/reshaping\_layers/flatten/
- [98] Dense layer. (Accessed on 24.06.2024). [Online]. Available: https://keras.io/api/layers/core\_layers/dense/
- [99] Add layer. (Accessed on 24.06.2024). [Online]. Available: https://keras.io/api/layers/merging\_layers/add/
- [100] J. Mierzejewski, J. Srebrny, H. Mierzejewski, and et al., "Eagle—the central european array for gamma levels evaluation at the heavy ion laboratory of the university of warsaw," Nuclear Instruments and Methods in Physics Research Section A: Accelerators, Spectrometers, Detectors and Associated Equipment, vol. 659, no. 1, pp. 84–90, 2011. [Online]. Available: https://www.sciencedirect.com/science/article/pii/S0168900211016585